WARWICK
THE UNIVERSITY OF WARWICK

A Thesis Submitted for the Degree of PhD at the University of Warwick

Permanent WRAP URL:
http://wrap.warwick.ac.uk/128299

Copyright and reuse:
This thesis is made available online and is protected by original copyright.
Please scroll down to view the document itself.
Please refer to the repository record for this item for information to help you to cite it.
Our policy information is available from the repository home page.

For more information, please contact the WRAP Team at: wrap@warwick.ac.uk

warwick.ac.uk/lib-publications

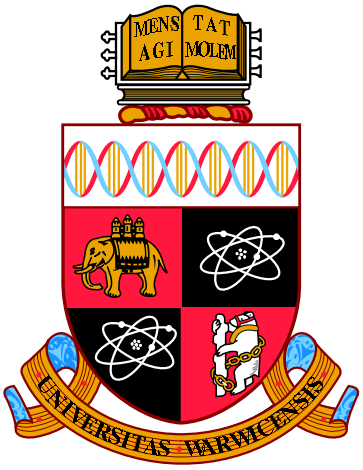

Ground states in low-dimensional quantum magnets

by

William James Anthony Blackmore

Thesis

Submitted to the University of Warwick

for the degree of

Doctor of Philosophy

Department of Physics

September 2018

THE UNIVERSITY OF
WARWICK

Contents

List of Tables

List of Figures

Acknowledgments

I would firstly like to thank my supervisor Paul Goddard for his support, guidance and patience throughout my four years as a postgraduate student. Special thanks to Jamie Brambleby for getting me started. I would also like to thank Martin Lees for his invaluable, extensive help with the measurement systems, and Oleg Petrenko, Tom Orton, Ali Julian and Patrick Ruddy for further technical assistance. Thanks also to the rest of the Superconductivity and Magnetism group for stimulating discussions, both related and unrelated to my work! My undercutting of the tea and coffee club will unfortunately have to end.

I am very appreciative of the work by Jamie Manson, Jacqueline Villa, Danielle Villa and Fan Xiao, who made the materials studied in this thesis, and for their advice. A big thanks to John Singleton in Los Alamos and Andrew Ozarowski in Tallahassee for enabling me collect data, and their advice. Also to my collaborators Tom Lancaster and Roger Johnson for helping me with understanding the finer points of μ-SR and neutron scattering respectively.

I am much appreciative of all my friends, both based at Warwick and elsewhere, for helping me retain what little sanity I had. Especially those, who are too many to name, who have joined me at Pub Wednesday, on socials, and shared the Flunkyball arena with me! Shout outs to Hary, Wilf and Connor as well for showing continuous interest in me and whisking me away to various place and events!

A final, massive thanks to my parents Alison and Tony, and sister Rachel, without whose love and support this thesis would not be.

Declarations

This thesis is submitted to the University of Warwick in support of my application for the degree of Doctor of Philosophy. It has been composed by myself and has not been submitted in any previous application for any degree. Experimental work presented in this thesis was carried out between October 2014 and September 2018 at the University of Warwick, the Pulsed Field Facility at the National High Magnet Field Laboratory (NHMFL) at Los Alamos National Laboratory (LANL) USA, the Electron Magnetic Resonance Facility at the NHMFL in Tallahassee USA, the ISIS Neutron and Muon Source at the Rutherford Appleton Laboratory and the Laboratory for Muon Spin Spectroscopy (LMU) at the Paul Scherrer Institute (PSI) Switzerland. This work, including data generated and data analysis, was carried out by myself except in the cases outlined below.

Powdered samples of $[Ni(3,5\text{-lut})_4(H_2O)_2](BF_4)_2$, $Ni(SiF_6)(H_2O)(4\text{-mepz})_2$, $Ni(H_2O)_2(acetate)_2(4\text{-picoline})_2$, $[Ni(pyz)_2(H_2O)_2](BF_4)_2$, $[Ni(D_2O)_2(pyz\text{-}d_4)_2](^{11}BF_4)_2$, $NiX_2(3,5\text{-lut})_4$ (X = HF_2, Cl, Br, I) and $NiF_2(3,5\text{-lut})_4{\cdot}H_2O$ were prepared by Dr. Jamie Manson, Jacqueline A. Villa and Danielle Y. Villa at the Department of Chemistry and Biochemistry, Eastern Washington University, USA. The structures of $[Ni(3,5\text{-lut})_4(H_2O)_2](BF_4)_2$ and $NiX_2(3,5\text{-lut})_4$ were obtained by Dr. John Schlueter and Dr. Yu-shen Cheng at the Advanced Photon Source, Argonne National Laboratory, USA. The structure of $[Ni(pyz)_2(H_2O)_2](BF_4)_2$ was obtained by Dr. Saul Lapidus at the Advanced Photon Source, Argonne National Laboratory, USA. The structures of $Ni(SiF_6)(H_2O)(4\text{-mepz})_2$ and $Ni(H_2O)_2(acetate)_2(4\text{-picoline})_2$ were obtained by Dr. Atta Arif at the University of Utah, USA. The structure of $NiF_2(3,5\text{-lut})_4{\cdot}H_2O$ was obtained by Dr. Robert

Williams and Sam Curley at the University of Warwick. Single crystals of $(QuinH)_2Cu(Cl_xBr_{1-x})_4{\cdot}2H_2O$ were grown and the relative abundance of the halide ions determined by Dr. Fan Xiao (now at the University of Bern) with the help of Prof. Mark Turnbull at Clark University, USA. Pulsed-field measurements of $[Ni(pyz)_2(H_2O)_2](BF_4)_2$, $NiX_2(3,5\text{-lut})_4$ (X = Cl, Br, I) and $NiF_2(3,5\text{-lut})_4{\cdot}H_2O$ were performed by Dr. Jamie Manson, Dr. John Singleton and Serena Birnbaum but the resultant data was analysed by myself. Secondary up pulsed-field measurements of $(QuinH)_2Cu(Cl_xBr_{1-x})_4{\cdot}2H_2O$ with (x = 0.17, 0.57, 0.74) were performed by Matthew Pearce but the resultant data was analysed by myself. Electron spin resonance measurements of $NiX_2(3,5\text{-lut})_4$ (X = HF_2, Br, I) were performed by Dr. Jamie Manson and Dr. Andrew Ozarowski but the resultant data was analysed by myself. SQUID magnetometry measurements of $[Ni(pyz)_2(H_2O)_2](BF_4)_2$ and heat capacity measurements of $Ni(H_2O)_2(acetate)_2(4\text{-picoline})_2$ were performed by Jamie Brambleby at The University of Warwick but the resultant data was analysed by myself. Muon spin resonance measurements of $(QuinH)_2Cu(Cl_xBr_{1-x})_4{\cdot}2H_2O$ (x = 0, 0.01, 0.09, 0.23, 0.25, and 0.41) were performed and analysed by Dr. Fan Xiao and Dr. Robert Williams at PSI. Muon spin resonance measurements of $[Ni(pyz)_2(H_2O)_2](BF_4)_2$ were performed and the data analysed by Dr. Fan Xiao, Dr. Tom Lancaster, Dr. Robert Williams and Dr. Stephen Blundell at PSI. Elastic neutron scattering data of $[Ni(pyz)_2(H_2O)_2](BF_4)_2$ was analysed by Dr. Roger Johnson at Oxford University.

The work presented in this thesis was also presented at the following conferences as a poster presentation:

- The 12th International Symposium on Crystalline Organic Metals, Superconductors and Magnets (ISCOM) "*Halide Substitution in a Low-Dimensional Molecular Magnet*" Zao, Miyagi, Japan (2017);
- Magnetism "*Magnetic exchange disorder in low-dimensional quantum magnets*" Manchester, UK (2018);

and in the form of oral presentations at:

- Magnetism "*Characterisation of powdered low-dimensional spin-1 antiferromagnets with single-ion anisotropy*" York, UK (2017);

- New Frontier of Molecular Materials (NFMM) "*Halide Substitution in a Low-Dimensional Molecular Magnet*" Sendai, Japan (2017).

Related work that will not be discussed further in this thesis has been published as:

- Leonardo H. R. Dos Santos, Arianna Lanza, Alyssa M. Barton, Jamie Brambleby, William J. A. Blackmore, Paul A. Goddard, Fan Xiao, Robert C. Williams, Tom Lancaster, Francis L. Pratt, Stephen J. Blundell, John Singleton, Jamie L. Manson and Piero Macchi, Journal of the American Chemistry Society **138**, 7, 2280 (2016).

Abstract

The ability to control the magnetic properties of low-dimensional magnetic systems is a major aim of research in condensed matter physics. Bespoke magnetic systems have potential uses in many practical applications and experimental investigations of theoretical predictions. To achieve this goal necessitates being able to determine the magnetic properties of these systems, which can require much expense in time, money and effort. In this thesis I present a methodology that can be used for characterising the properties of powdered, low-dimensional spin-1 antiferromagnets using commercially available measurement systems. The techniques involved are able to determine the magnetic properties of powdered systems containing isolated and exchange-coupled Ni^{2+} ions accurately enough such that a decision on growing single-crystals or measurements requiring more complicated measurements at specialist facilities can be made. Using this method, I then characterise the magnetic properties of a family of similar Ni^{2+}-halide-halide-Ni^{2+} chains which show differing magnetic behaviour linked to the different bridging ligands. It is found that single-ion anisotropy in Ni^{2+} octahedral environments is not just dependent on the placement but also the electronic properties of the coordinated non-magnetic ligands. Also, magnetic interactions along the Ni^{2+} chains are strongly influenced by the size of the bridging halide ions. The distance between adjacent ions is less important. This property was exploited to explore bond disorder in the spin-1/2 quasi two-dimensional antiferromagnet $(QuinH)_2Cu(Cl_xBr_{1-x})_4{\cdot}2H_2O$, which occurs due to the presence of two competing superexchange pathways with different interaction strengths. As the concentration increases from $x = 0$, disorder enhances quantum fluctuations which destroy long-range order before the percolation threshold is reached. This leads to multicritical points and the possible rise of a quantum Griffiths phase.

Chapter 1

Introduction

Magnetism was first discovered by the ancient Greeks in the 8th century BC [14], where it was noticed that lodestone, a naturally occurring magnetised material, could attract iron. The Chinese appear to be the first to discover the significance of the magnetic needle and it's application to navigation with the invention of the concept of true north in the 11th century AD. By the 12th century AD, lodestone was commonly used for navigation, albeit crudely. This was rectified by Pierre Pelerin de Maricourt, who described how to identify the poles of the compass and also the laws of magnetic attraction and repulsion [15]. de Maricourt also appeared to be the first to observe the magnetic field lines emanating from a spherical piece of lodestone. At this time compasses were "wet" and consisted of a magnetic material placed on an insulator that floated on water. The Yemeni astronomer Prince al-Ashraf, amongst others in the Middle East, made strides in the development of the dry compass, which did not require water and allowed the use of the device at sea [16]. This allowed the development of a much more accurate compass leading to the wider ranged explorations of the 14th and 15th centuries. Whilst it was known that magnetic needles pointed in a north-south direction, the reasons for such behaviour was not fully understood. In 1600, William Gilbert and partner Aaron Dowling described that the whole Earth itself was a magnet [17], whereas previously it was thought that a large magnetic island at the north pole caused the alignment of compasses.

1.1 Basics of magnetism

Up until this point, only the macroscopic properties of magnets had been investigated with anything close to being called scientific methods. In the 18th century

however, studies began to touch on the microscopic properties. Initially, the theory of magnetism was based on variations of fluids and also involved electricity. It was Charles Augustin Coulomb who first established that magnetic "fluids" are not free to flow like electric "fluids", but are bound to individual molecules. This led to the idea of the magnetic moment $\boldsymbol{\mu}$. Classically, this can be modelled as a current I moving in a circle (of area $\mathbf{A}$) via $\mathrm{d}\boldsymbol{\mu} = I\mathrm{d}\mathbf{A}$. At the microscopic level, magnetic moments occur due to unpaired electrons orbiting around a nucleus within orbitals. Therefore, the magnetic moment of an orbiting electron is proportional to the orbital angular momentum ($\mathbf{L}$) of the electron

$$\boldsymbol{\mu} = \gamma \mathbf{L}, \tag{1.1}$$

where γ is the gyromagnetic ratio. In a magnetic field $\mathbf{B}$, the moment has energy

$$E = -\boldsymbol{\mu} \cdot \mathbf{B}, \tag{1.2}$$

and torque

$$\mathbf{G} = \boldsymbol{\mu} \times \mathbf{B}. \tag{1.3}$$

In isolation, Eq. 1.3 would suggest that μ would like to align with the magnetic field. However, because torque is equal to rate of change of angular momentum, where $\mathbf{L}$ is given by Eq. 1.1, then Eq. 1.3 can be rewritten as [12]:

$$\frac{\mathrm{d}\mu}{\mathrm{d}t} = \gamma \boldsymbol{\mu} \times \mathbf{B}. \tag{1.4}$$

This shows that any change in $\boldsymbol{\mu}$ is perpendicular to both $\boldsymbol{\mu}$ and $\mathbf{B}$. Therefore, the direction of magnetic moments will precess around the applied magnetic field [18].

Whilst it was believed that there was connection between magnetism and electricity, it wasn't until the early 19th century before this was observed experimentally by Hans Christian Ørsted (commonly referred to as Oersted), who observed the flickering of a compass close to a current carrying wire, verifying this belief [19]. However, it took until the early 20th century with the advent of quantum mechanics before magnetism could be explained properly. This is because the electron itself has an intrinsic angular momentum called spin ($\mathbf{S}$), which is characterised using the spin quantum number S and component of spin angular momentum m_s. The component of the spin angular momentum can take one of $2S + 1$ values (S, $S - 1$, $S - 2$, . . ., $-S$) [20]. One electron has $S = 1/2$ and $m_s = \pm 1/2$. These components are called up and down respectively. The orbital angular momentum also has the

quantum numbers L and m_l which are analogous to the spin quantum numbers. The magnetic moment on an atom comes from the total angular momentum $\mathbf{J}$, which is defined by [21]

$$\mathbf{J} = \mathbf{L} + \mathbf{S}. \tag{1.5}$$

which has quantum numbers J and m_j. For atoms with unfilled electron shells, an unpaired electron or electrons can impart non-zero spin ($\mathbf{S}$) and orbital angular momentum ($\mathbf{L}$). Spin and orbital angular momentum are independent for free electrons, but they do couple when confined into orbitals. This effect is called spin-orbit coupling which has energy λ [12]. Hence, $\mathbf{L}$ and $\mathbf{S}$ are not individually conserved for electrons within atoms but the total angular momentum $\mathbf{J} = \mathbf{L} + \mathbf{S}$ is. This gives a large range of values for which $\mathbf{J}$ can take. However, a value of $\mathbf{J}$ for any atom can be given by Hund's rules. They are empirical rules that only apply to the ground state and assumes only one subshell is incomplete. In order of decreasing importance, they are

1. Maximise spin angular momentum. This minimises the Coulomb energy between electrons which arises from the Pauli exclusion principle (two electrons cannot occupy the same quantum state).

2. Maximise orbital angular momentum. This also minimises energy as electrons moving in the same direction are less likely to come into contact with each other.

3. The value of J is found by using $|L - S|$ if the shell is less than half full and $|L + S|$ if the shell is more than half full. This is an attempt to minimise the spin-orbit energy.

Hund's rules do not fully apply in certain cases. One example is the $3d$ transition metal ions with unfilled outer shells. In these materials, the crystal field interaction is much stronger than the spin-orbit interaction. This quenches the orbital angular momentum $\mathbf{L}$ and the third law doesn't apply. Therefore, the spin of 3d transition metal ions is due to the spin angular momentum of the unpaired electron, or electrons, in the outer shell ($\mathbf{J} = \mathbf{S}$). As it is 3d transition metal ions with unfilled outer shells that I am investigating in this thesis, I will use S to represent the spin of the ions from now on. Atoms with more than one unpaired electron will have $S > 1/2$ and therefore different m_s values. This will be discussed further in section 1.2.3. The size of μ is commonly measured in units of the Böhr magneton,

which is defined as the magnetic moment of a hydrogen atom with an electron in the ground state;

$$\mu_{\mathrm{B}} = \frac{e\hbar}{2m_e}, \tag{1.6}$$

and has the value $\mu_{\mathrm{B}} = 9.274 \times 10^{-24}$ Am^{-2}.

1.2 Non-interacting moments in a magnetic field

For an electron in a magnetic field B, the energy is given by

$$E = g\mu_{\mathrm{B}} m_s B \tag{1.7}$$

and therefore the energy levels of electrons split in a magnetic field. This is known as Zeeman splitting. In Eq. 1.7, g is the g-factor, which is a proportionality constant that relates the observed magnetic moment to the total spin and the Bohr magneton μ_{B}. For free electrons $g_e = 2.0023$ [22], but this changes for electrons bound in orbitals inside magnetic materials. This is due to different relative contributions of spin and orbital angular momentum. The Zeeman effect introduces the following term into the Hamiltonian of a material containing atoms with unpaired electron

$$\hat{\mathcal{H}}_{\mathrm{Zeeman}} = \mu_{\mathrm{B}} \sum_j \mathbf{g} \cdot \mathbf{S}_j \cdot \mathbf{B}. \tag{1.8}$$

where the sum is over all atoms in the compound. In magnetic systems, the overall moment per unit volume is known as the magnetisation ($\mathbf{M}$) and is the vector sum of all the magnetic moments. This is related to the magnetic flux density ($\mathbf{B}$) and magnetic field strength ($\mathbf{H}$) via

$$\mathbf{B} = \mu_0 \left(\mathbf{H} + \mathbf{M}\right), \tag{1.9}$$

where $\mu_0 = 4\pi \times 10^{-7}$ Hm^{-1} is the magnetic permeability of free space in which $\mathbf{B} = \mu_0\mathbf{H}$. $\mathbf{H}$ is the field applied to the sample and is produced by a current carrying wire which is applied to a magnetic material whereas $\mathbf{B}$ is the total magnetic field in the sample. At small applied fields, the magnetisation is directly proportional to the magnetic field $\mathbf{H}$ via the dimensionless magnetic susceptibility χ. For magnetic materials, molar susceptibility (χ_m) is commonly used and is defined as

$$\chi_m = \chi V_m = \frac{\mathbf{M} V_m}{\mathbf{H}}, \tag{1.10}$$

where V_m is the volume of one mole of the sample and therefore χ_m has units of $\mathrm{m^3 mol^{-1}}$.

1.2.1 Diamagnetism

All materials exhibit a magnetic susceptibility due to diamagnetism [23]. It occurs when a magnetic field is applied to the material and moments act to oppose the field. The diamagnetic susceptibility is given by

$$\chi = -\frac{Ne^2\mu_0}{6m_e V}\sum_{i=1}^{Z}\langle r_i^2\rangle \tag{1.11}$$

for a sample of volume V containing N atoms each with Z electrons of mass m_e at a distance r from the centre of the nucleus (assuming spherical symmetry). As the temperature increases, excited states become more important, though not significantly. Hence diamagnetism is considered to be largely temperature independent. Diamagnetism dominates in atoms with no unpaired electrons. The compounds in this thesis contain unpaired electrons and as such the diamagnetic susceptibility is small compared to other affects.

1.2.2 Paramagnetism

In compounds containing atoms with a non-zero magnetic moment due to unpaired electrons, the much stronger paramagnetic susceptibility dominates. This corresponds to a positive susceptibility due to an applied magnetic field inducing a magnetisation which aligns parallel with the magnetic field. In the absence of a magnetic field, isolated moments point in random directions. The application of the magnetic field acts to line up the moments with the field. An increase in temperature will increase the randomisation of the atoms and so the magnetisation of a material made up of isolated moments will depend on the ratio B/T [24].

The probability that a system is in a state α with energy E_α is proportional to the Boltzmann factor $\mathrm{e}^{-\beta E_\alpha}$ ($\beta = 1/k_\mathrm{B}T$) [25]. The partition function

$$Z = \sum_\alpha \mathrm{e}^{-\beta E_\alpha}, \tag{1.12}$$

is defined as the sum over all the states of the Boltzmann factors [26]. The magnitudes of E_α are somewhat arbitrary, what is important is the differences between the energy levels. Hence the ground state energy is given the value of $E_0 = 0$. From the partition function, the magnetisation as a function of field $M(H)$ and heat capacity

as a function of temperature $C_p(T)$ of isolated magnetic moments can be calculated. Magnetisation is given by

$$M(H) = -\left(\partial F/\partial H\right), \tag{1.13}$$

where $F = -k_{\mathrm{B}}T\ln Z$ is the Helmholtz function and heat capacity is

$$C_p(T) = \left(\partial U/\partial T\right), \tag{1.14}$$

where $U = \frac{-\mathrm{d}(\ln Z)}{\mathrm{d}B}$ is the internal energy. Eq. 1.13 gives rise to two relationships describing the magnetisation of isolated paramagnets. For a system of moments with arbitrary spin S, the Brillouin function is used to model the magnetisation [27]:

$$M = M_s\left[\frac{2S+1}{2S}\coth\left(\frac{2S+1}{2S}y\right) - \frac{1}{2S}\coth\left(\frac{y}{2S}\right)\right], \tag{1.15}$$

where

$$M_s = g_s\mu_{\mathrm{B}}S, \tag{1.16}$$

is the saturation magnetisation, and

$$y = g_s\mu_{\mathrm{B}}SB/k_{\mathrm{B}}T. \tag{1.17}$$

At low fields, Eq. 1.15 can be simplified to give the Curie Law for susceptibility, which is

$$\chi = \frac{g_s^2\mu_{\mathrm{B}}^2\mu_0 S(S+1)}{3k_{\mathrm{B}}T}. \tag{1.18}$$

1.2.3 Single-ion effects

In crystals containing $3d$ transition metals, the electronic energy levels of each metal ion is different to that of a free ion due to the interaction with surrounding atoms. This occurs due to a weak spin-orbit coupling interaction from unpaired electrons in the outer shells giving rise to electrostatic fields within the crystal which is called the crystalline electric field, or crystal field. As d orbitals within magnetic ions are not spherically symmetric, this induces an angular dependence within the atom. Local environments are also commonly not spherically symmetric, so the orbitals will behave in different ways to different structures. $3d$ transition metal ions, such as Ni^{2+}, contain five distinct d orbitals. These d orbitals fall into two classes, t_{2g} orbitals (d_{xy}, d_{xz} and d_{yz}) which point in between the $a(x)$, $b(y)$ and $c(z)$ crystal axes and the e_g orbitals (d_{z^2} and $d_{x^2-y^2}$) which point along these axes [28]. Depending

on the surrounding environment, the t_{2g} and e_g will split in energy. In octahedral environments, ligands are coordinated along the x, y and z-axes. Hence, the e_g orbitals will overlap with the ligand orbitals and are raised in energy. The t_{2g} orbitals have no overlap with the ligand orbitals and therefore are lowered in energy.

For ions with unfilled $3d$ orbitals, the order in which the orbitals are filled is different depending on the strength of the crystal field. If the crystal-field effects are weak, then the Coulomb energy of putting two electrons close together dominates and the electrons singly occupy all orbitals before it doubly occupies any orbital. However, if the crystal field energy is larger than the Coulomb pairing energy then electrons will doubly occupy the lower energy orbitals before they try and occupy the higher energy orbitals. This is an important effect as it dictates the spin of the ion which in turn will affect the magnetic properties. For example, a Co^{2+} ion contains seven electrons in its outer $3d$ shell. In an octahedral environment the three t_{2g} orbitals are in the ground state. For strong crystal fields, these are fully populated first, leaving one, unpaired, electron in one of the e_g levels. This gives the Co^{2+} ion an overall spin of $S = 1/2$. For weak crystal fields, all five orbitals are occupied singularly before the remaining two electrons double up. This leaves three unpaired electrons, and therefore a spin of $S = 3/2$. The magnetic properties of the magnetic ion can also influence the surrounding environment via the Jahn-Teller effect. This occurs because the elastic cost of distorting, for example, an octahedral environment around the magnetic ion is balanced by the electronic energy saving of the distortion [29].

For $S > 1/2$, the crystal field can split the m_s energy levels in zero-field and is therefore called zero-field splitting [30] and is described using the Hamiltonian term [31]:

$$\hat{\mathcal{H}}_{\text{spin}} = \mathbf{S} \cdot \mathbf{D} \cdot \mathbf{S} \tag{1.19}$$

where $\mathbf{D}$, the zero-field splitting tensor, is symmetric and traceless. Assuming that the $\mathbf{D}$ tensor in Eq. 1.19 and the $\mathbf{g}$ tensor in Eq. 1.8 have the same principal axes, then for a system of $S \geq 1$ ions Eq. 1.19 can be rewritten to [32]

$$\hat{\mathcal{H}}_{\text{spin}} = D \sum_i \hat{S}_i^{z\,2} + E \sum_i \left(\hat{S}_i^{x\,2} - \hat{S}_i^{y\,2} \right) \tag{1.20}$$

where D and E are the zero-field splitting parameters. For $S = 1$ ions and a field applied parallel to the unique z-axis, D is defined as the energy difference between the $m_s = \pm 1$ and $m_s = 0$ energy levels. The parameter E represents the energy difference between the $m_s = +1$ and $m_s = -1$ levels [33]. From Eq. 1.20, a positive

value of D corresponds to the $m_s = 0$ level being the ground state and the system is described as being easy-plane as moments prefer to align within the xy plane. A negative D causes the $m_s = \pm 1$ state to have the lowest energy (for $E = 0$). This corresponds to moments that prefer to align parallel to the z-axis and the system is known as easy-axis. A non-zero E occurs if the x and y directions are dissimilar, and is kept positive as the assignment of the x and y axes is arbitrary for low-symmetry environments. The constraints on D, E and the anisotropic g-factor are determined by the spin-Hamiltonian formalism given by Eq. 1.20 and are [34, 35]:

$$\begin{aligned} &|D| \geq 3E, \\ &D = \left(\tfrac{\lambda}{2}\right)\left[g_z - \tfrac{g_x+g_y}{2}\right], \\ &E = \left(\tfrac{\lambda}{4}\right)(g_x - g_y). \end{aligned} \tag{1.21}$$

If the first constraint is not met, redefining which crystal axes correspond to the x, y and z axes will solve the issue. The spin-orbit coupling parameter λ has a value of $\lambda = -454$ K for free Ni^{2+} ions. For Ni^{2+} ions bound into three-dimensional lattices, it is expected that this value will change. λ has been measured to be of the same order of magnitude as the free value for various Ni^{2+} octahedra [34].

As zero-field splitting causes a preferred direction for the moments to point in, it is also called single-ion anisotropy. The magnitudes of D and E and the sign of D is dependent on the ligands surrounding the magnetic ion and therefore will differ between different compounds. How the structure and composition affects the single-ion anisotropy in the coordination complexes described in this thesis is not fully understood. A previous extended study has attempted to describe how the single-ion anisotropy changes in different systems containing isolated $S = 1$ Ni^{2+} ions [35–39]. One of the authors of these studies also reviewed the magnetic properties of a vast amount of different $S \geq 1$ isolated systems [34]. Data from a range of experimental techniques were used to empirically determine the structural dependency of single-ion anisotropy. For $S = 1$ Ni^{2+} ions in octahedral environments, it was found that an increased elongation of the octahedron in the z-axis corresponds to an increasingly positive D parameter. This is due to a weaker crystal field in the z direction and leads to easy-plane anisotropy. Accordingly, an axially compressed octahedron corresponds to a stronger crystal field in the z-direction and easy-axis anisotropy. This will be investigated further in Chapters 3 and 4.

1.3 Interacting moments in a magnetic field

Magnetic moments that are close enough together such that their respective wavefunctions interact undergo an exchange interaction. This is basically an electrostatic interaction, which for two ions is given by

$$\hat{\mathcal{H}}_{\text{spin}} = J\mathbf{S}_1 \cdot \mathbf{S}_2, \tag{1.22}$$

where J is the the magnitude of the exchange interaction. For a system of such interacting spins which can point in any direction, the Hamiltonian is given by

$$\hat{\mathcal{H}}_{\text{spin}} = \sum_{\langle i,j \rangle} J_{ij}\mathbf{S}_i \cdot \mathbf{S}_j, \tag{1.23}$$

where $\langle i, j \rangle$ denotes a sum over unique pairs of spins with a magnitude of interaction J_{ij} between them. This is known as the Heisenberg model. The related models where spins are confined to one and two dimensions are known as the Ising and XY models respectively. This modifies the components of the spins in Eq. 1.23 by $\mathbf{S}_i, \mathbf{S}_j \rightarrow S_i^z, S_j^z$ for the Ising model and $\mathbf{S}_i, \mathbf{S}_j \rightarrow S_i^{xy}, S_j^{xy}$ for the XY model. Whilst this effect can be due to exchange anisotropy, these models can contain contributions from single-ion anisotropy effects described in section 1.2.3.

Direct exchange occurs between electrons on neighbouring atoms that interact via an exchange described by Eq. 1.23. Whilst it is possible for direct exchange to occur in real magnetic materials, due to the high localisation of the electron orbitals around the magnetic ions it is rarely a significant mechanism. Generally, indirect exchange is the main method for magnetic ions to interact with each other [40]. In the materials studied in this thesis (described later in section. 1.4.3), this process is called superexchange. Magnetic ions are separated by non-magnetic ligands. There is no direct overlap between electrons on the magnetic ions. However, the bonding with these ligands allows the electrons to delocalise over the whole system [41]. This accounts for a much larger kinetic energy saving compared to direct exchange between magnetic atoms due to a bigger area for electrons to travel over. Whilst there is also a potential energy due to electron repulsion, this is small. The superexchange interaction is usually antiferromagnetic.

1.3.1 Ferromagnetism

A ferromagnet has a spontaneous magnetisation at low temperatures, without the need of an applied magnetic field. This occurs when the lowest energy configuration

is for adjacent moments to point parallel to each other. This necessitates $J < 0$ in Eq. 1.23. Ferromagnetism is described phenomenologically using the Weiss model, which uses an effective molecular field at the i'th site [42]:

$$\mathbf{B}_{mf} = -\frac{2}{g\mu_{\mathrm{B}}} \sum_j J_{ij}\mathbf{S}_j = \alpha\mathbf{M}, \tag{1.24}$$

to model the exchange interaction to an adjacent site j. In Eq. 1.24, α is a constant which parametrises the strength of the molecular field and is positive for ferromagnets. If Eq. 1.24 is added as an extra term to the Zeeman Hamiltonaian in Eq. 1.8, then the effective Hamiltonian can be written as

$$\hat{\mathcal{H}} = g\mu_{\mathrm{B}} \sum_i \mathbf{S}_i \cdot (\mathbf{B} + \mathbf{B}_{mf}) \,. \tag{1.25}$$

This allows the problem to be treated as if the system was a paramagnet. At temperatures much lower than J, the parallel alignment of the spins is self-sustaining, even in the absence of an applied magnetic field. This is known as the ferromagnetic ordered state. As the temperature is raised, thermal fluctuations increase until a certain temperature (T_{C}, C stands for Curie) above which the order is destroyed. This critical temperature is known as the ordering temperature. The phase transition between the ferromagnetic and paramagnetic regimes is a second-order phase transition, and as such has discontinuities in heat capacity (called a lambda peak) and the gradient of the magnetisation. The corresponding ordering peak in the gradient of $\chi T(T)$ has been shown to be at the ordering temperature via the Fisher relation [43]. The Weiss model modifies Eq. 1.18 so that susceptibility is proportional to $1/\left(T - T_{\mathrm{C}}\right)$ and

$$\chi = \frac{g^2\mu_{\mathrm{B}}^2\mu_0 S(S+1)}{3k_{\mathrm{B}}\left(T - T_{\mathrm{C}}\right)}, \tag{1.26}$$

which is called the Curie-Weiss Law.

1.3.2 Antiferromagnetism

An antiferromagnet occurs when the exchange interaction between adjacent spins is more than zero, with $J > 0$. It is therefore energetically favourable for neighbouring moments to align antiparallel with each other. A lattice of such interacting spins can be decomposed into two interpenetrating sublattices [Fig. 1.1(a)]. The moments in one sublattice all point in one direction whereas the moments in the other point in the opposite direction [40]. These sublattices can be individually described using the Weiss model analogous to the ferromagnetic case above with molecular fields B_+

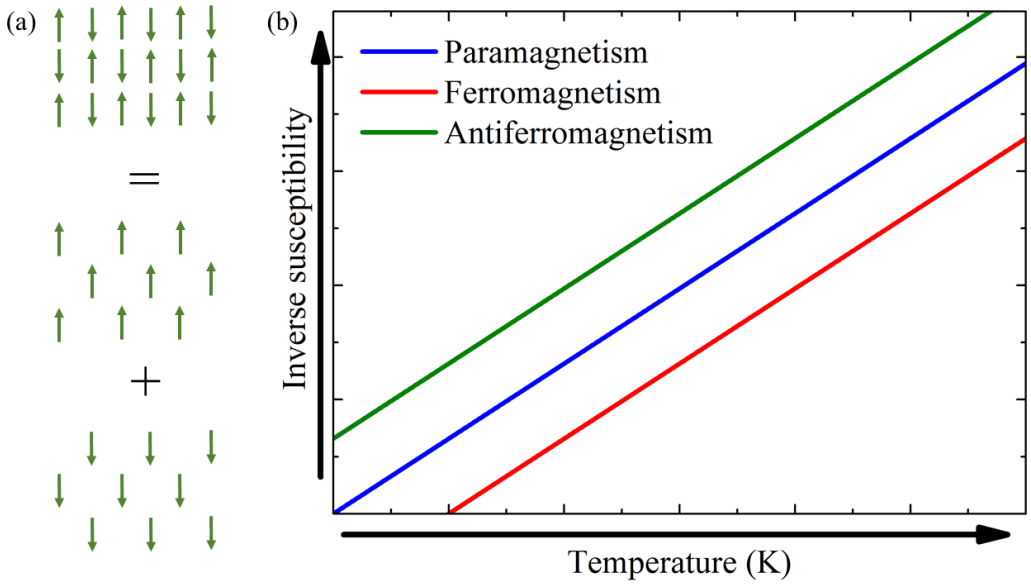

Figure 1.1: **(a)** The ground state of an antiferromagnet is made up of two sublattices with equal and opposite magnetisation. **(b)** The type of interactions within a sample can be determined using high-temperature inverse susceptibility and Eq. 1.29. For paramagnets the inverse susceptibility extrapolates to the origin. Ferromagnets have a positive x-axis intercept whereas antiferromagnets have a negative one.

and B_-. The magnetisation of each sublattice will have the same magnitude but opposite sign such that the overall magnetisation will be zero in the ordered state:

$$\begin{aligned} B_+ &= -|\alpha| M_-, \\ B_- &= -|\alpha| M_+. \end{aligned} \tag{1.27}$$

Similar to the ferromagnetic case, there is a critical temperature T_N (N stands for Néel) above which there is no order. The Weiss model for antiferromagnetism modifies Eq. 1.26 to:

$$\chi = \frac{g^2 \mu_\mathrm{B}^2 \mu_0 S(S+1)}{3k_\mathrm{B}\left(T + T_\mathrm{N}\right)}. \tag{1.28}$$

This enables the analysis of high temperature susceptibility data to determine the interactions within magnetic materials using the Curie-Weiss law:

$$\chi = \frac{g^2 \mu_\mathrm{B}^2 \mu_0 S(S+1)}{3k_\mathrm{B}\left(T - \theta_\mathrm{W}\right)}, \tag{1.29}$$

where θ_W is the Weiss temperature [Fig. 1.1(b)]. If $\theta_\mathrm{W} = 0$ then Eq. 1.29 simplifies to the Curie Law (Eq. 1.18) and the material is a paramagnet. If $\theta_\mathrm{W} > 0$ then

the x-axis intercept in the inverse susceptibility is also positive and the sample is a ferromagnet. Likewise if $\theta_{\mathrm{W}} < 0$ then the compound is antiferromagnetic and the x-axis intercept is negative [44]. However, there are some caveats which need to be taken into account. The Curie-Weiss Law is only applicable in the limit of low fields and high temperatures. The Weiss temperature is also sometimes called the magnetic ordering temperature, the temperature at which paramagnetic moments fully align with the applied magnetic field. Whilst $|\theta_{\mathrm{W}}| \approx T_{\mathrm{N}}$,$T_{\mathrm{C}}$ for three dimensional magnetic lattices, it is certainly not the case for lower dimensional magnetic systems [45]. The presence of a non-zero Weiss temperature does not imply the existence of long-range magnetic order at low temperatures. The sign of θ_{W} should still indicate the type of interaction within the sample however, but only in the absence of terms other than exchange and Zeeman in the Hamiltonian

Due to the two sublattices, when a magnetic field is applied to a three-dimensional Heisenberg antiferromagnet at low temperatures, the direction of the field is important. It is not energetically favourable for moments to align with a small (relative to J) field applied to two sublattices of equal but opposite magnetisation at $T = 0$. The energy saved by aligning one sublattice is cancelled by the cost to align the other sublattice due to J. If a small magnetic field is applied parallel to the direction of the spins, a small term is added or subtracted to the local field of each sublattice, depending on the orientation of the spins. This has no effect on the sublattice already aligned with the field as it is already saturated. It is also not enough to overcome J and therefore the sublattice aligned antiparallel is also unaffected and the parallel susceptibility $\chi_{||} = 0$. If the field is applied perpendicular to the spins this causes the spins to tilt and have a net magnetisation parallel to the field, with a corresponding perpendicular susceptibility $\chi_{\perp} \neq 0$. As the temperature is increased, the perpendicular case doesn't change as the molecular field of both sublattices are reduced equally by thermal fluctuations. In the parallel case, the applied field enhances the magnetisation of one sublattice but decreases the other. This induces an increase in the susceptibility until it reaches $\chi_{\perp}$ at T_{N} [Fig. 1.2(a)]. Above the ordering temperature, the susceptibility will show paramagnetic behaviour where the direction of the applied field is not important.

For a powdered low-dimensional system, the susceptibility data will average to a broad peak [Fig. 1.2(b)]. This position of peak does not signify long-range order, but is dependent on the strength of magnetic interactions between adjacent ions. This can then be used to determine the magnitude of J. Susceptibility data of isotropic antiferromagnetic compounds are modelled using high-temperature series

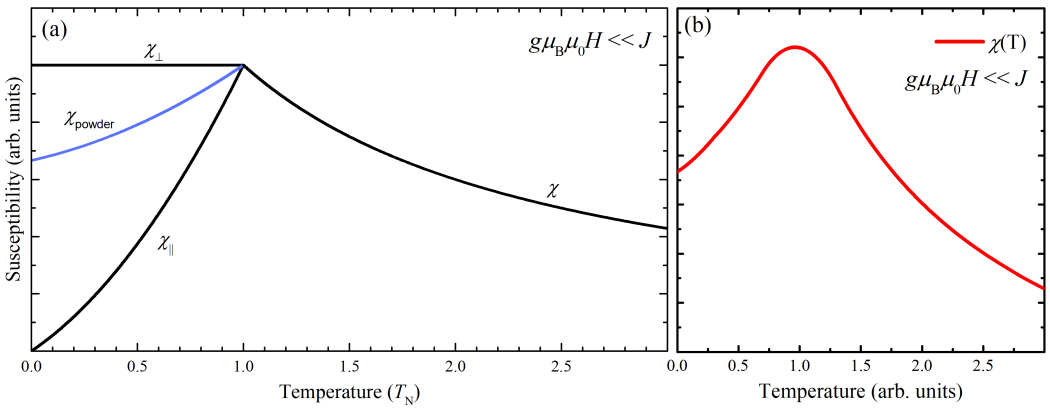

Figure 1.2: Susceptibility of **(a)** a three-dimensional Heisenberg antiferromagnet for a magnetic field applied parallel and perpendicular to the magnetisation axis and **(b)** a powdered low-dimensional Heisenberg antifferomagnet

expansions of the form

$$\chi_{mol} = C\frac{\sum_n a_n A^n}{\sum_m b_m A^m}, \tag{1.30}$$

where

$$C = \frac{g_s^2 \mu_B^2 \mu_0 S(S+1)}{3k_B T}, \tag{1.31}$$

is the Curie constant, $A = (J/T)$, and a_n, b_m are coefficients which depends on the magnetic dimensionality. This is an effective method for determining J in isotropic antiferromagnets [46–51]. Models for more anisotropic compounds do exist [52], but problems occur when modelling data of powdered samples [13]. This will be discussed further in chapter 3

If a strong magnetic field is applied, such that $\mu_0 H \gg J$, then the moments will be fully aligned with the field. For Heisenberg and XY antiferromagnets, as the applied magnetic field is increased, the moments will smoothly align parallel to the field. For Heisenberg antiferromagnets, there is one sharp feature in the magnetisation data indicating the saturation point, whereas for XY antiferromagnets there are two, corresponding to the saturation of moments when the field is applied parallel to the xy plane and z-axis (see section 2.3 for more details). For Ising-like antiferromagnets, the way in which the moments align depends on the orientation of the field. At $T = 0$, for an increasing field applied perpendicular to the preferential axis of the sublattices, the moments smoothly rotate and align with the field. However, for a field applied parallel to the direction of the sublattices, initially nothing happens. In the weak Ising-like anisotropy case, at a critical field (discussed further in section 2.3) the moments will "snap" into a different configuration where the

direction of the sublattices point at an angle $\pm\theta$ to the direction of the field. This process is called a spin-flop. As the field is raised further, the moments smoothly rotate towards the direction of the field. If there is strong Ising-like anisotropy, then a spin-flip may occur for a field applied parallel to the easy-axis. This is where the magnetisation of one of the sublattices suddenly reverses and the system moves to a fully aligned state in one step.

1.4 Low-dimensional magnetism

Low-dimensional magnetism garnered interest in the early to middle 20th century following the theoretical work of Bethe on one dimensional materials in 1931 [53], and follow up studies on anisotropic chains by Bonner and Fisher [46]. The significant advance in two-dimensional magnetism during this time was an exact solution to the two-dimensional Ising problem solved by Lars Onsager in 1944 [54]. However, strong interest in low-dimensional magnetism exploded in the 1970s and 1980s, much due to the pioneering work by David J. Thouless, J. Michael Kosterlitz (see section 1.4.1) and F. Duncan Haldane (see section 1.4.2) for which they won the Nobel prize for physics in 2016. Along with developments in coordination chemistry (see section 1.4.3) in the 1980's, this created a fertile breeding ground for experimental and further theoretical investigations of low-dimensional magnets [55]. Unlike in three dimensions, low-dimensional magnetic materials support strong quantum fluctuations which leads to novel quantum excitations and novel ground states [56]. These are described below.

1.4.1 Quasi-two dimensional magnetism

Much of the focus in low-dimensional magnetism in the mid-20th century was aimed at sheets of magnetically interacting spins. Whilst the Mermin-Wagner theorem predicts the absence of long-range order for ideal isotropic two-dimensional magnets at $T \neq 0$, it says little about the ground state at $T = 0$ [57]. For long-range order to develop at finite temperatures requires only a small amount of anisotropy, via either magnetic exchange or interlayer interactions [58]. Much current work is directed at $S = 1/2$ square lattice Heisenberg antiferromagnets (SLHAF) due to possible connections to understanding high-T_{C} cuprate superconductors [59]. These contain planes of $S = 1/2$ copper ions bridged by oxygen atoms. The Cu-O planes are necessary for the superconducting properties. When the temperature is reduced in SLHAF's, the size of short-range spin correlations (also known as the spin-spin correlation length ξ) increases exponentially and diverges at $T = 0$, suggesting the

presence of long range order.

For spins confined to point in one or two directions, the situation is different. The two-dimensional XY model also doesn't order at finite temperatures, but there are two different phases within this range. The first is at high-temperatures, where spin-spin correlations decay away exponentially. This changes to an algebraic decay at lower temperatures and the transition between the two phases is known as the Kosterlitz-Thouless (KT) transition, or sometimes the BKT transition (where B = Vadim Berezinski), and is a topological phase transition. Topology describes the properties of materials that are invariant under continuous transformations, such as stretching or twisting. Due to quantum and thermal fluctuations destroying long range order in two-dimensions, it was believed that there could be no phase transitions in such systems. However, a phase transition does occur due to the thermal stability of vortices that occur in two-dimensional materials. At low temperatures the vortices form pairs, but as the temperature is increased they disengage and move apart, becoming single. Unusually, this is a phase transition that doesn't break any symmetry; there is no local order parameter (such as magnetisation) that goes to zero at a critical temperature. This is a universal theory that can be used in all kinds of materials in two-dimensions, and even in other areas of physics, such as statistical mechanics or atomic physics. In two-dimensional $S = 1/2$ XY antiferromagnets there is a predicted KT transition at $T_{\mathrm{KT}} = 0.3427(2)J$ [60].

For Ising spins on a two-dimensional lattice, there is a non-zero temperature below which long-range order occurs throughout the lattice. This is because the energy cost of thermally exciting a spin to flip is balanced out by the gain in entropy. Both of these equally scale with the size of the region in which all spins are flipped. As energy and entropy are balanced, neither have an advantage and a stable, long-range ordered state can occur if the temperature is lowered enough.

1.4.2 Quasi-one dimensional magnetism

Similar to the two-dimensional case, long range order doesn't occur for ideal isotropic one-dimensional antiferromagnets at finite temperatures. However, unlike in two-dimensions, this lack of long-range order also applies to Ising chains. Fluctuations, both quantum and thermal, have a much stronger affect on spin chains than they do in two-dimensions. The entropy gain of flipping one spin far outweighs the energy cost as long-range order is destroyed by the flipping of one spin. In reality however, there is no such thing as an ideal spin chain. Long-range order is induced via an interchain interaction $J_{\perp}$ which stabilises the ordered ground state. One interest in pursuing theoretical and experimental studies of spin chains is to understand the

excitations. For example, in Ising spin chains, excitations are associated with domain walls. Once created these excitations move freely along the chain. Heisenberg spin chains also have excitations known as spinons, which are $S = 1/2$ and gapless. Therefore, they order at zero temperature. This was found to be true for all half-integer Heisenberg spins chains.

However, large fluctuations contribute differently depending on the value of the spin. Haldane predicted that the ground state of the one-dimensional Heisenberg antiferromagnet with integer spin would contain nonlinear quantum fluctuations. This creates a singlet, nonmagnetic ground state separated from excited states by an energy gap Δ. This is known as the Haldane gap, and is a nontrivial symmetry-protected topological phase. Spin-spin correlations have an exponential decay as the temperature is lowered, such that there is an absence of long range order even for $T = 0$. The Haldane model also holds for slightly anisotropic chains, though there are constraints on the magnetic parameters. For isolated chains to be in the Haldane state, calculations predict that $|D|/J < 0.29(1)$ for Ising and $D/J < 0.99(2)$ for XY compounds [4]. For positive $D > J$, the system is driven to a quantum paramagnet (QPM) phase where single-ion anisotropy is dominant. The QPM phase also doesn't order at finite temperatures due to the dominant single-ion anisotropy term forcing the spins into the non-magnetic $m_s = 0$ state [61]. It differs to the Haldane phase in that the application of a magnetic field leads to a field induced quantum phase transition into a canted XY antiferromagnetic phase [4].

In non-Heisenberg Haldane chains, the size of the gap is dependent on the direction of the applied field and the magnitude of the single-ion anisotropy D. In zero field this relationship is [62]

$$\begin{aligned} \Delta_z &= \Delta_0 + 1.41D, \\ \Delta_{xy} &= \Delta_0 - 0.57D, \end{aligned} \tag{1.32}$$

for systems with uniaxial symmetry, where $\Delta_0 = 0.41191J$ is the size of the gap for isotropic systems [51]. In an applied field, a Zeeman term is introduced to account for the energy level splitting of the excited triplet state, which will close the gap. In real Haldane systems, there is also an interchain interaction ($J_\perp$). If $J_\perp$ is large enough, the system becomes too three-dimensional, which quenches the Haldane gap. The phase diagram for $S = 1$ antiferromagnetic chains is shown in Fig. 1.3(a).

Experimentally, the Haldane phase can be observed in the exponential decay of susceptibility [51, 63, 64] and zero-field magnetic heat capacity data [65] as $T \to 0$. In an applied field, the excited triplet state splits via the Zeeman mechanism. This

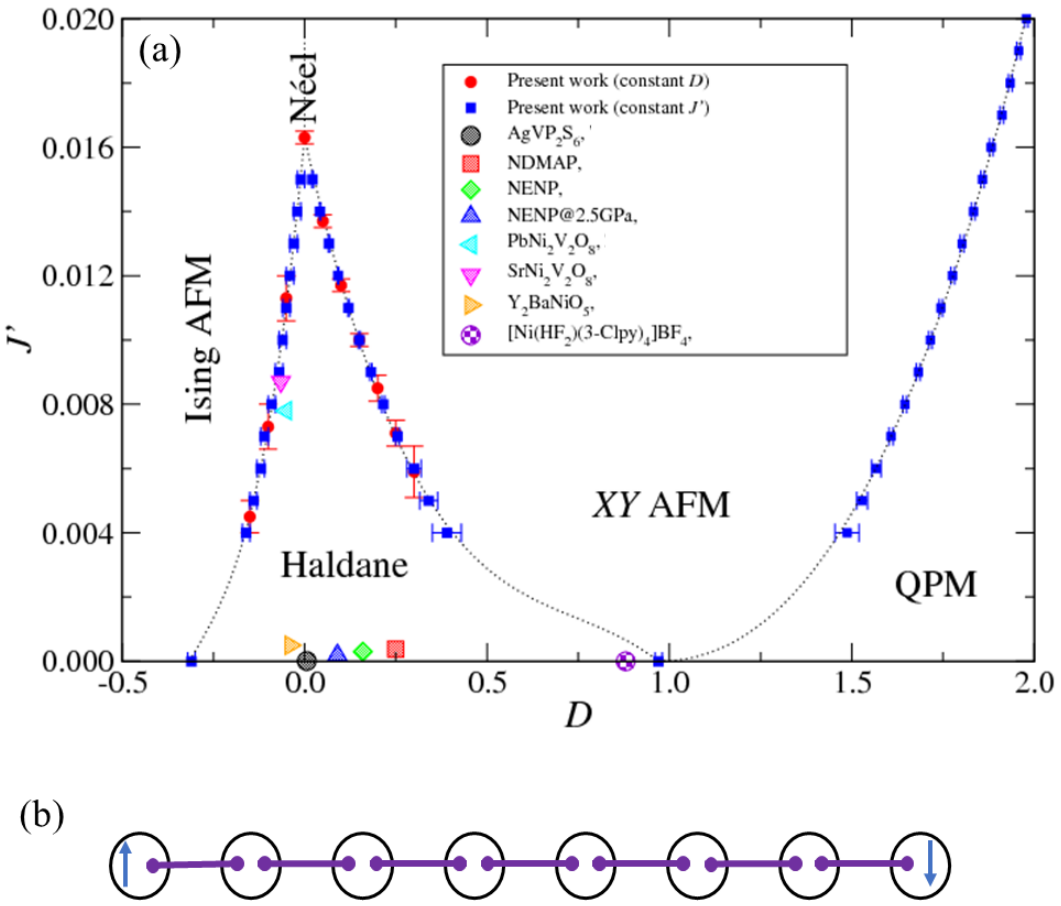

Figure 1.3: **(a)** Theoretical phase-diagram of the $S = 1$ antiferromagnetic chain taken from Ref. [4]. The red circles and blue squares represent the quantum Monte-Carlo calculated phase boundaries. The dotted lines are guides to the eye. The cross hatched symbols represent the estimated positions of some Haldane compounds from the reported D and $J' \equiv J_\perp$ values [5–10]. **(b)** Representation of the valence bond solid model in spin-1 chains. The unshaded circles represent spin-1 sites which are split into two symmetric $S = 1/2$ moments (purple circles), with each $S = 1/2$ moment interacting with an $1/2$ moment on an adjacent site (purple line). The moments at the end of finite chains (blue arrows) are unpaired and act as paramagnets for long chains

closes the Haldane gap at field $g\mu_B\mu_0 H_{C1} = \Delta$. For a Haldane chain at very low temperatures in the region $H < H_C$, the magnetisation is very small due to the spins occupying the nonmagnetic ground state [66–70]. Above H_{C1}, the ground state becomes magnetic and the magnetisation rises approximately linearly until saturation

at $g\mu_B\mu_0 H_{SAT} = SnJ = 4J$ (n = number of magnetic exchange interactions with neighbouring ions, $S = 1$ in this thesis). Field induced long range order develops for $H > H_C$, which has been observed in heat capacity measurements of the Haldane chains $SrNi_2V_2O_8$ [70] and NDMAP [6, 71, 72].

The valance bond solid (VBS) state is a special case of the AKLT (Affleck-Kennedy-Lieb-Tasaki) state, and occurs for periodic chains. In the VBS state each $S = 1$ moment is made up of a combination of two symmetric $S = 1/2$ spins. An $S = 1/2$ spin on one site forms a singlet bond with an $S = 1/2$ spin on an adjacent site [Fig. 1.3(b)]. The VBS state occurs in Haldane spin-chains [4]. Hence the end of $S = 1$ Heisenberg antiferromagnetic chains in the Haldane phase are $S = 1/2$ moments, offering exciting ways to probe the Haldane phase by introducing impurities to sever the chains. This is predicted to have dramatic effects on the low-energy excitations [73], which has been studied by doping the $S = 1$ moments in Haldane chains with nonmagnetic Zn^{2+} [74] or Mg^{2+} [75] ions and $S = 1/2$ Cu^{2+} ions [76]. When Haldane chains are doped in this way, two free $S = 1/2$ moments are produced either side of the impurity [77]. For short chains, it was found that $S = 1/2$ moments couple along the chains to form $S = 1$ triplets [74, 78, 79]. In longer chains, they act as free paramagnets. This effect can be also observed in powders as the paramagnetism dominates magnetisation and electron spin resonance data at low temperatures [80, 81]. These end chain effects are further experimental evidence that an integer spin chain is in the Haldane phase.

1.4.3 Coordination polymers

Recently, coordination polymers have been used to great effect in the experimental studies of low-dimensional magnetism. Coordination polymers are neutral compounds made up of arrays of metal ions linked by a variety of coordinated organic and inorganic ligands [82]. These coordinated linkages are not constrained to three dimensions. Other types of bonding, such as hydrogen bonding or Van der Waals forces, may also be present to keep atoms and molecules linked in two or one directions. These are technically called one or two dimensional coordination polymers [83]. In this thesis the umbrella term "coordination polymer" will include all low dimensional polymers. Fully uncoordinated molecules may be required to counter the charge of the metal ion to achieve charge neutrality throughout the compound. Coordination polymers were accidentally discovered at the start of 18th century by the German colourmaker Diesbach. Diesbach was trying to make the pigment cochineal red lake but due to impurities in the starting ingredients ended up with a deep blue, called Prussian Blue [84]. The formula ($Fe_4[Fe(CN)_6]_3 \cdot xH_2O$) and

structure of Prussian Blue wasn't discovered until the late 1970's [85, 86].

The advantages of this type of material is that the constituent parts can be interchanged almost at will. This can create a near limitless amount of compounds with different structures and combinations of metal ions and ligands. The effect that structure and composition has on the magnetic properties can be investigated by studying closely related polymers via a variety of experimental techniques. This can be done in different ways. An example is the NiX_2(pyz)$_2$ family (Cl, Br and I, pyz = pyrazine $C_4H_4N_2$) [1]. NiX_2(pyz)$_2$ is a quasi-two dimensional antiferromagnet with magnetic interactions through Ni-pyz planes. The halide ions bridge between nickel ions in adjacent planes. Whilst the intraplane magnetic interaction J remain relatively unchanged, the magnitude of the interplane exchange $J_\perp$ increases as X moves down group 7 of the periodic table such that $J_\perp \ll J$ for X=Cl and $J_\perp > J$ for X=I. This indicates that the strength of magnetic interactions can be directly controlled by composition of the compound. Similarly, by exchanging ligands the dimensionality of the magnetic system can be altered [87]. This has been achieved using [Cu(pyz)(pyO)$_2$(H$_2$O)$_2$](PF$_6$)$_2$ and [Cu(pyz)$_2$(pyO)$_2$](PF$_6$)$_2$ (pyO = pyradine-N-oxide, C_5H_5NO). [Cu(pyz)$_2$(pyO)$_2$](PF$_6$)$_2$ is made up of planes of Cu^{2+} ions bridged by pyz molecules which mediate magnetic interactions. The pyO molecules are non-bridging and inhibit the exchange so that [Cu(pyz)$_2$(pyO)$_2$](PF$_6$)$_2$ is a quasi-two dimensional antiferromagnet. By changing the relative amounts of the starting ingredients, a powdered sample of [Cu(pyz)(pyO)$_2$(H$_2$O)$_2$](PF$_6$)$_2$ was grown. Two non-bridging water molecules replaced a bridging pyz molecule in the unit cell creating a quasi-one dimensional antiferromagnet [88]. The effect structure and composition has on the single-ion anisotropy of $S \geq 1$ coordination polymers can be investigated by changing any ligand or magnetic ion before the production stage and then characterising the magnetic properties of the resultant compound. Coordination polymers have already been shown to be highly suited to large-scale investigations into this area [34].

1.5 Thesis motivation

The theoretical work on low-dimensional magnetism and advances in coordination chemistry has led to a vast amount of experimental investigations into low-dimensional quantum magnetism in the last few decades. This is partly driven by possible applications in data storage, catalysis and quantum computing amongst others [88–92]. Coordination polymers are also highly suited to experimentally exploring exotic low-dimensional phases due to the ability to tune the magnetic

properties towards quantum critical points [1, 13, 61, 87, 93–101]. The ability to be able to understand the structural and compositional dependency of the magnetic properties of coordination polymers is therefore of major interest to both chemists and physicists alike. To be able to produce bespoke magnetic systems for physical applications or experimental tests of theoretical predictions is the ultimate goal of research in this area. There have been a large number of experimental studies into the magnetism of spin half coordination polymers in recent years, in which the role of structure and composition has on the magnetic properties has been reasonably well understood [92, 96, 102–104]. This allows the use of $S = 1/2$ systems to more efficiently explore exotic states experimentally, such as Bose-Einstein condensates [105–107] or quantum spin liquids [108].

However, this is not the case for $S \geq 1$ magnetic compounds due to the more complex ground state that these systems exhibit. There has been progress in explaining the single-ion properties of these high-spin systems, but some compounds containing coordinated halide ions do not agree with theoretical predictions [34]. Explicit investigations into understanding the single-ion anisotropy parameters of $S \geq 1$ compounds containing exchange-coupled spins are also quite rare. This is because the competition between single-ion and exchange effects causes immense difficulties when characterising the magnetic properties of these materials. This is exacerbated by the lack of single crystals to make measurements on. The powdered nature of the sample scrambles the crystal axis with respect to the applied magnetic field, increasing the features present in magnetic measurements. Features may also have contributions from both single-ion properties and magnetic exchange, which can be difficult to untangle [13]. Currently, it requires a lot of time, expense and effort to characterise these systems. In this thesis, I will attempt to produce a method with which the characterisation of powdered exchange coupled $S = 1$ compounds can be performed using commercially available lab based equipment. I will then use this method to characterise the properties of a family of $S = 1$ chains to determine the effect composition and the structural parameters have on single-ion anisotropy properties and strength of magnetic exchange interactions. One of the compounds in this family is a near-ideal Haldane chain whose properties make it ripe for further study. Lastly, I will characterise a bond-disordered $S = 1/2$ copper based quasi two-dimensional antiferromagnet, to experimentally test the validity of two theoretical predictions [109, 110].

Chapter 2

Experimental Techniques

2.1 Magnetometry

2.1.1 Quasi-static measurements

Magnetometry measurements were performed using a Superconducting Quantum Interference Device (SQUID), which is an insert into a Quantum Design Magnetic Property Measurement System (MPMS) [11]. The MPMS can precisely control the temperature of the sample in the range $1.8 \leq T \leq 400$ K. The lower range can be extended down to ≈ 0.5 K with the use of a iQuantum Helium-3 (^{3}He) insert. A superconducting magnet is used to generate fields up to 7 T. Due to the sensitivity of the SQUID to fluctuations in magnetic fields, a magnetic shield is required to keep the magnetic field in the SQUID stable. Linear magnetic susceptibility as a function of temperature $\chi(T) = M/H$ and magnetisation as a function of field $M(H)$ can be measured in this set-up. The sample is loaded into a gelatin capsule, which is attached to a nonmagnetic sample holder at the end of a rigid rod. This then moves through a superconducting detection coil, made up of a single piece of superconducting wire wound into a set of 3 coils as shown in Fig. 2.1. In this configuration the upper and lower coil are wound in a clockwise direction and the middle coil is wound in an anti-clockwise direction. This is to reduce noise in the detection circuit caused by fluctuations in the magnetic field and also minimises background drifts in the SQUID caused by relaxation in the magnetic field of the superconducting magnet. As the sample moves through the coils, the local changes in magnetic flux density produced by the dipole field of the sample is measured. This change induces a current in the superconducting wire which then inductively couples to the SQUID sensor producing an output voltage which is directly proportional to the current flowing through the detection coil. This acts as a highly sensitive current to voltage

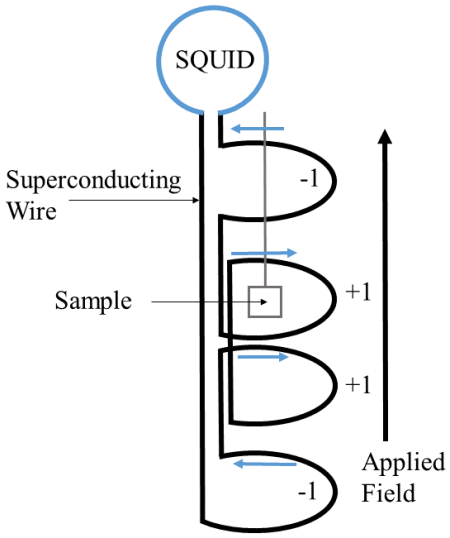

Figure 2.1: Figure showing the superconducting detection coil in the MPMS. The labels -1 and $+1$ correspond to windings in the clockwise and anti-clockwise directions respectively [11]. The square represents the sample.

converter. The voltage as a function of position of a sample with a known magnetic moment is used to calibrate the system. The output voltage then provides a direct measurement of the sample's magnetic moment. The SQUID magnetometer is sensitive to very small magnetic moments, enabling characterisation of small samples or materials with a weak longitudinal magnetism.

2.1.2 Pulsed-field measurements

Pulsed-field magnetisation measurements were performed at the National High Magnetic Field Laboratory in Los Alamos, USA. Fields of up to 65 T with typical rise times $\approx$ 10 ms were used. Powdered samples or single crystals were mounted in 1.3 mm diameter polychlorotrifluoroethylene [PCTFE = $(C_2ClF_3)_n$] ampules (inner diameter 1.0 mm) which are attached to a probe containing a 1500-turn, 1.5 mm bore, 1.5 mm long compensated-coil susceptometer, constructed from 50 gauge high-purity copper wire [96]. The ampules can be moved into and out of the susceptometer. When the sample is within the coil and the field pulsed the voltage induced in the coil is proportional to the rate of change of magnetisation with time ($\mathrm{d}M/\mathrm{d}t$). The total magnetisation is obtained by numerical integration of the signal with respect to time. A subtraction of the integrated signal recorded using an empty coil (sample moved out) under the same conditions is required to calculate the magnetisation of the sample [96]. The magnetic field is measured via the signal induced

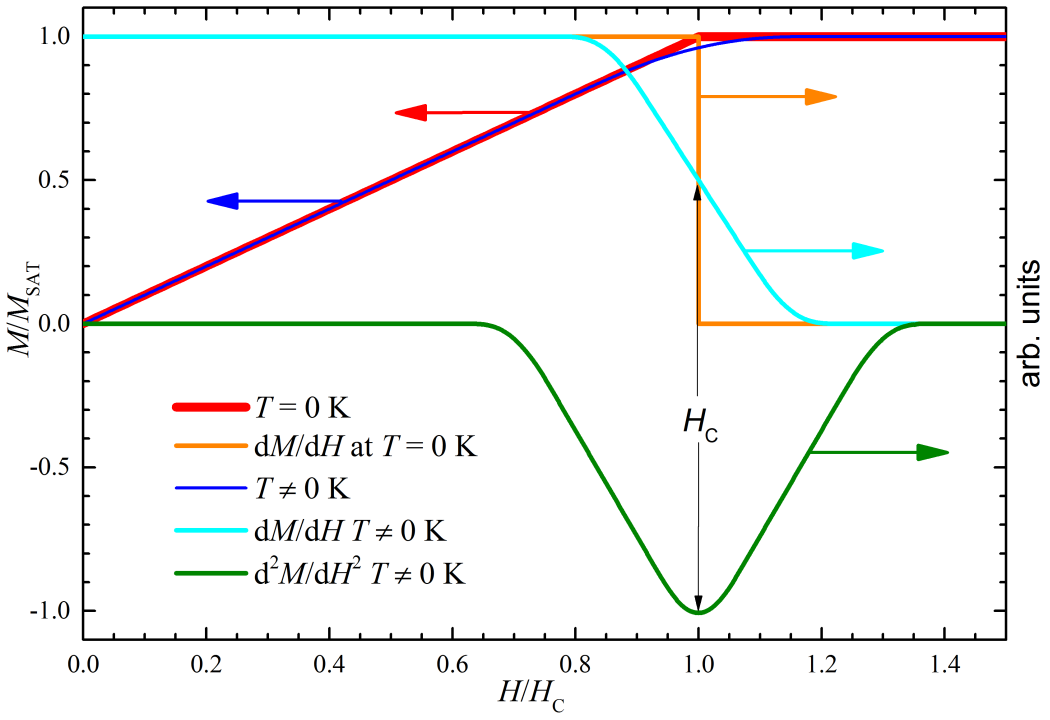

Figure 2.2: Antiferromagnetically coupled spin$-1/2$ moments fully saturate at H_C in zero-temperature (red) causing a step function in the differential susceptibility (orange). Finite temperatures (blue) smooths the saturation point such that it can be difficult to obtain H_C in the differential susceptibility (cyan). However, by differentiating again, a more accurate H_C can be obtained as the position of the trough in $\mathrm{d}^2M/\mathrm{d}H^2$ (green).

within a coaxial 10-turn coil and calibrated via observation of de Haas-van Alphen oscillations arising from the copper coils of the susceptometer [96]. The susceptometer is placed inside a ^{3}He cryostat, which can attain temperatures as low as 500 mK. Sometimes, due to constant offsets in the signal amplification circuit, the zero-field $\mathrm{d}M/\mathrm{d}t$ is not measured to be zero. This induces a linear term into the magnetisation when the signal is integrated and has the form $M_{\mathrm{linear}} = \alpha B$. The constant α is obtained by fitting the magnetisation at fields above the saturation field to a linear fit. This term is then subtracted to give the magnetisation of the sample.

Many Heisenberg antiferromagnets show a well defined saturation transition at $T = 0$ (Fig. 2.2). Non-zero temperatures act to smooth the saturation field H_C. Anisotropy in a powdered sample would also affect the saturation point in this way. This makes it more difficult to determine the point at which the moments would

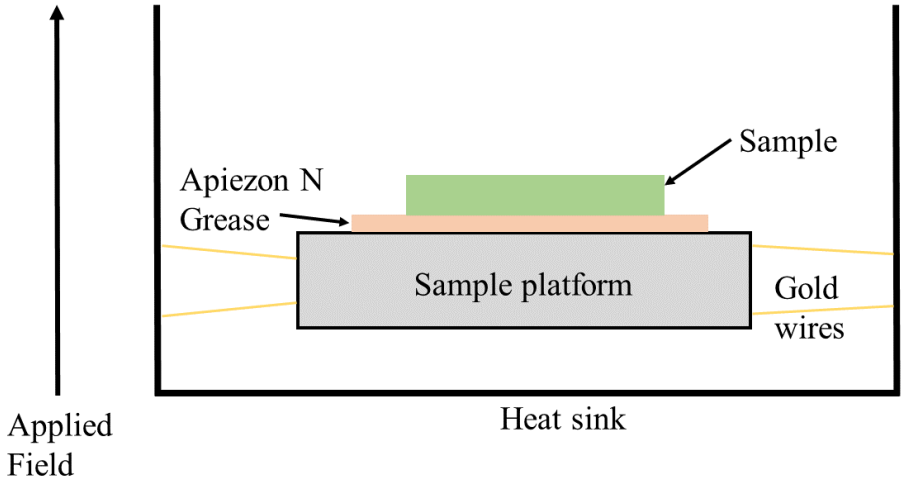

Figure 2.3: Diagram for a thermal-relaxation calorimeter. The powdered sample is pressed into a pellet and stuck to the platform using Apiezon N grease to ensure good thermal conductivity. Gold wires thermally link the platform to a heat sink of temperature T_0 and make an electrical connection to power the temperature sensor and heater.

saturate at zero temperature. A previous study has used the midpoint of the drop in $\mathrm{d}M/\mathrm{d}H$ [1]. The exact midpoint can be difficult to determine, especially if the signal is small or the data is noisy. However, an accurate value of H_C can be found from the position of the minimum in $\mathrm{d}^2M/\mathrm{d}H^2$. This corresponds to the point of highest gradient in $\mathrm{d}M/\mathrm{d}H$ and is typically close to the midpoint of the drop.

2.2 Heat capacity

Heat capacity measurements were made using a Quantum Design Physical Property Measurement System (PPMS) [111]. It contains a superconducting magnet that can reach fields of 9 T and a cryostat which can lower the temperature to 1.8 K. Temperatures down to ≈ 0.5 K can be obtained by using a ^{3}He insert. The PPMS determines the specific heat capacity of a sample by measuring the thermal response of the sample to a change in temperature. Powdered samples are pressed into pellets and attached to the sample platform using Apiezon N grease (Fig. 2.3). The grease not only provides a good thermal connection between sample and platform but also as a glue to keep the sample in place. The platform contains a small heater and the temperature is determined via a bare Cernox sensor. Wires thermally link

the platform to a heat sink, and also make an electrical connection to power the temperature sensor and the heater. A heat pulse is used to increase the temperature of the platform and therefore the sample. A temperature increase of $\approx 1\%$ of that of the thermal bath is used. The PPMS measures the platform temperature as the sample and platform cools back to the level of the thermal bath. A two-tau fitting method is used to determine the heat capacity of the sample [111, 112]. The first time constant, τ_1, is used to model the temperature difference between the sample holder and the heat sink. The second time constant, τ_2, is used to describe the temperature difference between the sample and the platform. During heat capacity measurements, τ_2 is only necessary if there is poor thermal connection between the sample and the sample holder.

Heat capacity measurements of the coordination polymers in this thesis contain two contributions. Low temperature data is dominated by the magnetic heat capacity (C_{mag}). At high temperatures phonons are dominant (C_{latt}). Phonons are quantised lattice waves that describe vibrations of the lattice via normal modes. There are two models that are commonly used to describe vibrations in solids; the Einstein model and the Debye model. The former assumes that all vibrational modes have the same frequency w and is prominent at high-temperature. The Debye model assumes a distribution of frequencies and dominates over the Einstein model at low temperatures [24]. These models are field independent. To obtain the magnetic heat capacity, it is necessary to subtract off the phonon contribution. This is performed by modelling the high temperature zero-field data with

$$C_{\text{latt}} = \frac{3A_{\text{D}}}{x_{\text{D}}^3}\int_0^{x_{\text{D}}} \frac{x^4 e^x}{\left(e^x-1\right)^2} + \sum_{i=1}^{n} A_{\text{E}i}\frac{\theta_{\text{E}i}^2}{T^2}\frac{e^{(\theta_{\text{E}i}/T)}}{\left[e^{(\theta_{\text{E}i}/T)}-1\right]^2}, \tag{2.1}$$

where $x = \hbar\omega/k_{\text{B}}T$ and there are n Einstein modes. The amplitude A and temperature θ are fitted, where D and E denote the Debye and Einstein modes respectively.

2.3 Analysing magnetisation and heat capacity data of powdered samples

Whilst measurements on single crystals are ideal for determining the magnetic properties of anisotropic quantum magnets, single crystals sufficiently large enough are not always readily available. Commonly, new quantum magnets are only available as powders. The mixing of different crystal directions with respect to the applied field causes a loss of information from the magnetic or physical response. However, some details can be obtained from measurements on powders. Comparing the re-

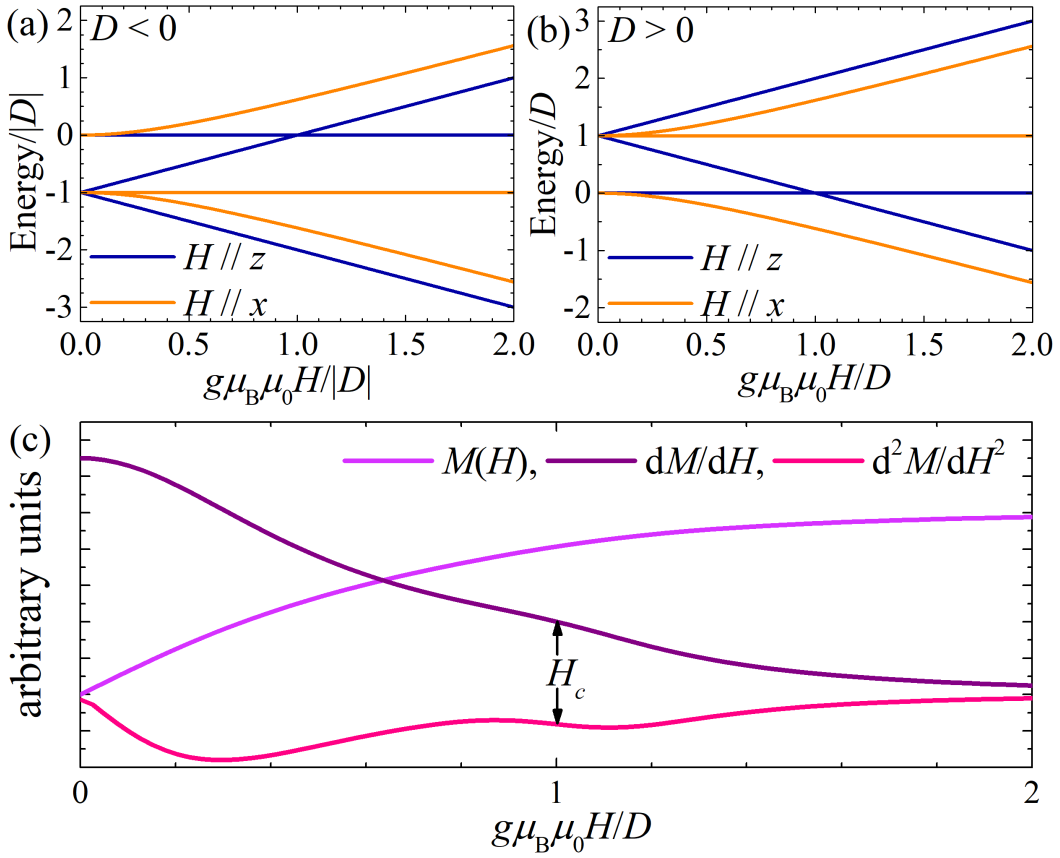

Figure 2.4: Ground state energy level diagrams for **(a)** easy-axis anisotropy and **(b)** easy-plane anisotropy with $E = 0$. **(c)** Simulated magnetisation of a powdered compound containing isolated $S = 1$ ions with easy-plane single-ion anisotropy and $E = 0$. A bump in $\mathrm{d}M/\mathrm{d}H$ and a derivative shape in $\mathrm{d}^2M/\mathrm{d}H^2$ are expected once the applied field causes a ground state energy-level crossing.

sults of experiments to simulations enables an accurate analysis of the measured compound. In this section, the effect powder averaging has on bulk magnetometry and heat capacity measurements is presented. A portion of this work has already been reported [13, 101, 113], but is described again due to its importance as a tool in the analysis of the compounds in this thesis.

For isolated $S = 1$ moments with easy-plane anisotropy, when the applied field is parallel to the hard axis there is a level crossing between the $m_z = 0$ zero-field ground-state and the $m_z = 1$ level [Fig. 2.4(b)] at the critical field H_C, where:

$$g\mu_\mathrm{B}\mu_0 H_\mathrm{C} = \sqrt{D^2 - E^2}. \tag{2.2}$$

This corresponds to a sharp increase in the single crystal magnetization, and a peak in the differential susceptibility dM_z/dH. For a powder, this feature is reduced to a small bump [101]. The simulated differential susceptibility for isolated $S = 1$ ions with easy-plane anisotropy ($D >0$), and $E = 0$, is plotted in dimensionless units in Fig. 2.4(c). The peak in dM/dH can be seen to correspond to the midpoint of the peak-derivative shape in the d^2M/dH^2 data. By simulating the differential susceptibility at different temperatures, it is found that the peak indicating the level crossing at $H = H_c$ is only observed once the temperature is lowered below approximately $0.12D$ [13]. This is because the thermal occupation of excited states obscures the crossing of the ground-state at high-temperatures.

Simulations of the magnetisation of ideal low-dimensional $S = 1$ AFMs were made in MATLAB, using a mean-field semi-classical approach [13]. For the easy-plane case, two critical fields are expected for $nJ < D$. The first is when moments saturate due to an applied field parallel to the xy-plane, and assuming $J_\perp \ll J$ occurs at:

$$g\mu_{\mathrm{B}}\mu_0 H_{\mathrm{C1}} = 2SnJ, \tag{2.3}$$

where $n =$ number of nearest interacting neighbours. The second is is when moments saturate for fields parallel to the x-axis and occurs at

$$g\mu_{\mathrm{B}}\mu_0 H_{\mathrm{SAT}} = 2(nJ + D)S. \tag{2.4}$$

In the easy-axis description, the interpretation of the upper-critical field is analogous to the easy-plane case and occurs for fields perpendicular to z-axis and occurs when:

$$g\mu_{\mathrm{B}}\mu_0 H_{\mathrm{SAT}} = 2(nJ + |D|)S. \tag{2.5}$$

For fields parallel to the z-axis, two transitions can occur. The first is a spin-flop transition at which point the collinear antiferromagnetically ordered moments, which are aligned to the easy axis in zero-field, discontinuously jump to a canted phase in which the z components are aligned to the field whilst the remaining xy component is antiferromagnetically ordered. This occurs at $H = H_{\mathrm{sf}}$ [114]

$$g\mu_{\mathrm{B}}\mu_0 H_{\mathrm{sf}} = 2S\sqrt{|D|(nJ - |D|)}, \tag{2.6}$$

and necessitates $nJ > D$ to be observed. As the field continues to rise further, the moments smoothly approach saturation at $H_{\mathrm{C1}} < H_{\mathrm{SAT}}$, where

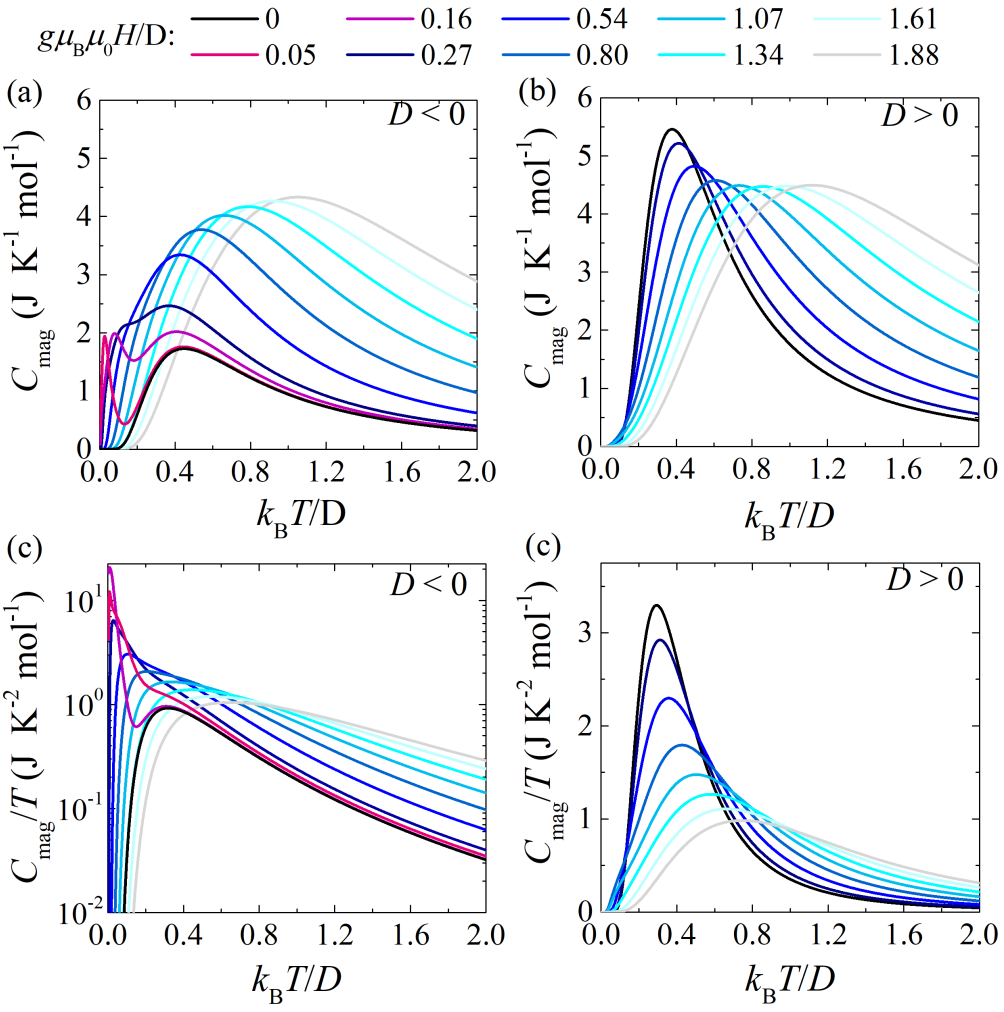

Figure 2.5: Simulations of C_{mag} vs. T and C_{mag}/T vs. T of powdered $S = 1$ **(c)**,**(e)** easy-axis and **(d)**,**(f)** easy-plane compounds with $E = 0$.

$$g\mu_B\mu_0 H_{C1} = 2(nJ - |D|)S. \tag{2.7}$$

Here, H_{C1} contains a contribution from D as it can only be reached through the spin-flop phase which contains a non-zero xy-component of the spins. For powdered samples a feature is expected at H_{C1} and H_{SAT} for both easy-plane and easy-axis cases. This analysis gives two methods to determine the sign of D. The first is that a spin-flop will only be observed in the case of a uni-axial system. The second is that the separation of H_{C1} and H_{SAT} has a different dependence on D for the easy-axis and easy-plane cases.

The heat capacity of a system of isolated $S = 1$ ions with a D only Hamilto-

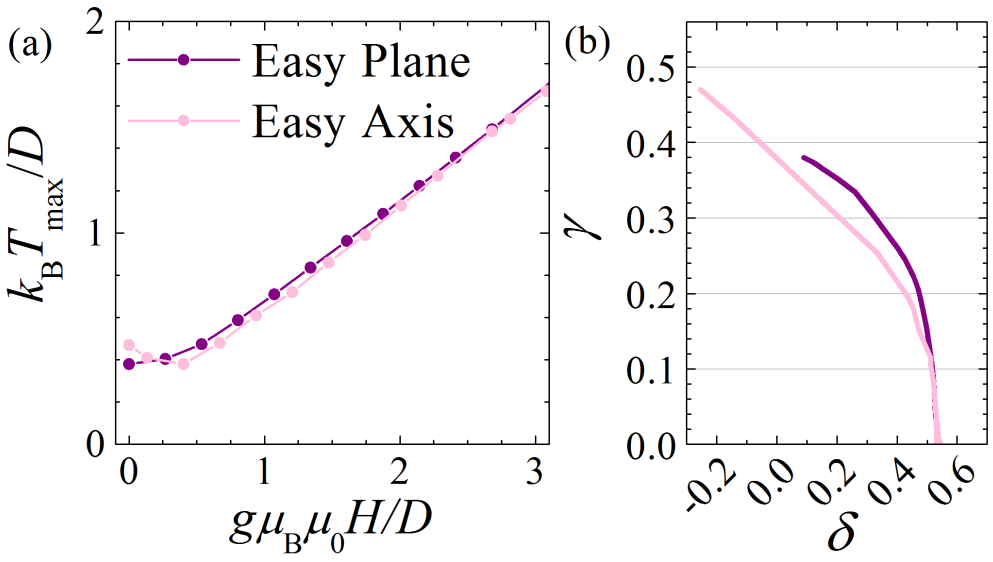

Figure 2.6: **(a)** Simulated position temperature of the Schottky anomaly vs. applied field for powdered $S = 1$ compounds with easy-plane and easy-axis anisotropy with $E = 0$. **(b)** The local gradient versus the zero field intercept of the data in panel (a).

nian in powdered form was simulated using MATLAB [113]. The powder averaging is modelled by considering 20 different applied fields with respect to the z-axis as defined by D. It was assumed that $E = 0$ in the simulations. For the case of easy-axis anisotropy ($D < 0$), the Ni^{2+} ions have a bistable ground-state in zero-field [Fig. 2.5(a)]. The simulated heat capacity [Fig. 2.5(a)] shows a single broad maximum at a temperature set by D in zero-field. In an applied field, the degeneracy of the ground-state is lifted, resulting in a small second peak in the specific heat emerging at low temperatures due to the depopulation of the upper level of the low-energy doublet [Fig. 2.4(a)]. The two peaks merge and move to higher temperatures as the applied field is increased further. For easy-plane anisotropy ($D > 0$) the system always has a unique ground state, and in an applied-field the single broad maximum in C_{mag} moves continuously to higher temperatures [Fig. 2.5(b)].

To extract the magnetic parameters from heat capacity measurements the field-dependence of the Schottky anomaly T_{max} is plotted in dimensionless units [Fig. 2.6(a)]. In the easy-axis case, only the broad feature present in zero-field is tracked. The field dependence of T_{max} [Fig. 2.6(a)] is parametrised by taking the gradient of the data in Fig. 2.6(a) as a function of field. This can be written as:

$$\frac{k_{\mathrm{B}}T_{\mathrm{max}}}{|D|} = \gamma + \delta\left(\frac{g\mu_0\mu_{\mathrm{B}}H}{|D|}\right), \tag{2.8}$$

where there are two field-dependent parameters: (i) δ, the local gradient; and (ii) γ, the zero-field intercept. Multiplying Eq. 2.8 by D suggests the intercept of a linear fit to $T_{\max}$ vs. $g\mu_0\mu_B H$ is equal to γD. The pre-factor γ can be uniquely determined for a particular sign of D by using the measurement of δ and Fig. 2.6(b). The sign of D is apparent from the field dependence of the Schottky peaks.

2.4 Electron spin resonance

High-field, high-frequency Electron spin resonance (ESR) spectra of powdered samples were recorded on a home-built spectrometer at the EMR facility, National High Magnetic Field Laboratory, Tallahassee, Florida, USA. Microwave frequencies in the range $52 \leq \nu \leq 626$ GHz at temperatures ranging from ≈ 3 K to 80 K were used in the measurement. The instrument is a transmission-type device and uses no resonance cavity. Powdered samples are loaded into thin teflon vessels and lowered into the cryostat. The microwaves were generated by a phase-locked Virginia Diodes source, generating frequency of 13 ± 1 GHz, and equipped with a cascade of frequency multipliers to generate higher harmonic frequencies. The resultant signal was detected using a cold bolometer. A superconducting magnet capable of reaching fields up to 15 T was employed.

ESR is an experimental technique that is highly suited to determining the difference between ground-state and excited energy levels in condensed matter [27]. Using a combination of frequency dependent and temperature dependent studies, the sign and magnitude of single-ion anisotropy (see section 1.2.3) parameters can be obtained [21]. In ESR measurements, microwave radiation ($10^9 - 10^{11}$ GHz) is supplied to a sample in a magnetic field. The magnetic field splits the energy levels via the Zeeman mechanism [115]. If the injected photon has the same energy (ν) as the difference between the energy levels (ΔE), then the photon will be absorbed by the spin. This induces a transition of the spin to a higher energy state:

$$\Delta E = h\nu = g\mu_B\mu_0 H\Delta m_s, \tag{2.9}$$

where $\Delta m_s = \pm 1$ is the allowed change in the spin state. This causes a peak in the ESR spectrum. At low fields, energy-level mixing occurs. This allows transitions between spin states with $\Delta m_s = \pm 2$. This transition is called the half-field transition as it occurs at approximately half the mean-field of the $\Delta m_s = \pm 1$ transitions. As both ν and ΔE can be changed (the latter tuned using different $\mu_0 H$), there are two different methods to obtaining spectra; by scanning the frequency or the field. Because of difficulty in scanning microwave frequencies and the common use of

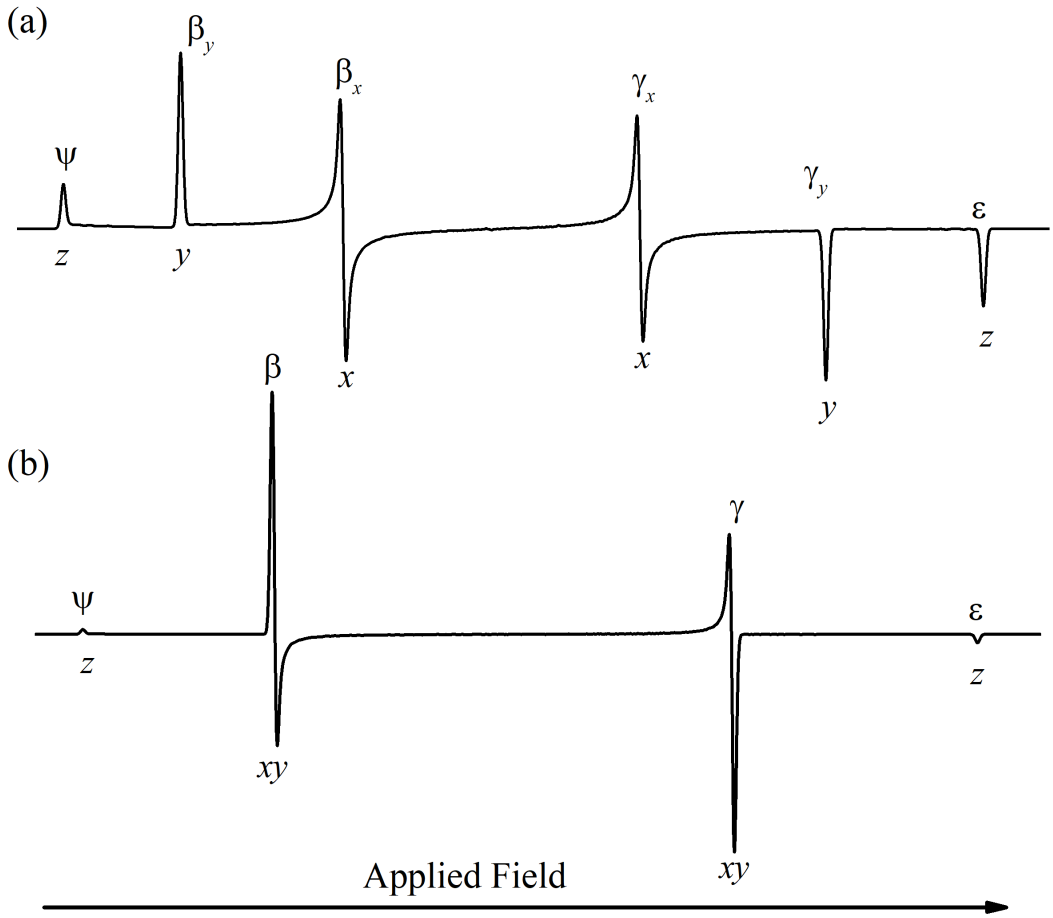

Figure 2.7: Resonances observed in ESR spectra of powdered samples with **(a)** the Hamiltonian in Eq. 2.10 ($D \neq 0$ and $E \neq 0$) and **(b)** uniaxial symmetry ($D \neq 0$ and $E = 0$). Adapted from Ref. [12].

resonant cavities for signal detection, most ESR spectrometers keep the frequency constant and change the field.

In this thesis, ESR measurements have been used to determine the single-ion parameters of $S = 1$ powdered compounds. Spectra of these samples can exhibit up to nine resonances, three for each crystal axis that field can be applied along. The position of each of these resonances can be calculated by exact diagonalisation of the $S = 1$ Hamiltonian:

$$\hat{\mathcal{H}} = D\sum_i \hat{S}_i^{z\,2} + E\sum_i \left(\hat{S}_i^{x\,2} - \hat{S}_i^{y\,2}\right) + \mu_{\mathrm{B}}\mu_0 \sum_i \boldsymbol{g}\cdot\boldsymbol{H}\cdot\hat{\boldsymbol{S}}_i. \tag{2.10}$$

This yields, for fields parallel ($||$) to the x,y and z axes, the expected resonance field for a particular frequency ν and unknown single-ion anisotropy parameters D and

E [12]:

$$
\begin{aligned}
&\Delta m_s = \pm 1 \text{ transitions} \\
&\mu_0 H \parallel x-\text{axis}: \quad \mu_0 H = \tfrac{1}{g_x \mu_\mathrm{B}} \sqrt{\left[h\nu \pm \tfrac{3}{2}\left(\tfrac{1}{3}D - E\right)\right]^2 - \tfrac{1}{4}\left(D+E\right)^2}. \\
&\mu_0 H \parallel y-\text{axis}: \quad \mu_0 H = \tfrac{1}{g_y \mu_\mathrm{B}} \sqrt{\left[h\nu \pm \tfrac{3}{2}\left(\tfrac{1}{3}D + E\right)\right]^2 - \tfrac{1}{4}\left(D-E\right)^2}. \\
&\mu_0 H \parallel z-\text{axis}: \quad \mu_0 H = \tfrac{1}{g_z \mu_\mathrm{B}} \sqrt{\left(h\nu \pm D\right)^2 - E^2}. \\
&\Delta m_s = \pm 2 \text{ transitions} \\
&\mu_0 H \parallel x-\text{axis}: \quad \mu_0 H = \tfrac{1}{2g_x \mu_\mathrm{B}} \sqrt{\left(h\nu\right)^2 - \left(D+E\right)^2}. \\
&\mu_0 H \parallel y-\text{axis}: \quad \mu_0 H = \tfrac{1}{2g_y \mu_\mathrm{B}} \sqrt{\left(h\nu\right)^2 - \left(D-E\right)^2}. \\
&\mu_0 H \parallel z-\text{axis}: \quad \mu_0 H = \tfrac{1}{2g_z \mu_\mathrm{B}} \sqrt{\left(h\nu\right)^2 - 4E^2}.
\end{aligned}
\tag{2.11}
$$

Representative first derivative of the transmission spectra for an $S = 1$ powdered sample are presented in Fig. 2.7 showing the expected shapes of the resonance peaks with components of the spin state with $\Delta m_s = \pm 1$. The first derivative is commonly used for convenience as the position of the resonances can be observed more easily [116]. For low symmetry, the y and z transitions (field applied parallel to the y and z axis) are peak shapes, whereas the x transition are peak derivative shapes. For uniaxial symmetry ($E = 0$), the z transition is a peak shape and the xy transition is a peak derivative shape. Due to the large amount of resonances that may occur during a measurement, it is necessary to label them appropriately. The labels for this thesis are presented in Fig. 2.7 and Fig. 2.8. For a field applied parallel to the z axis, the half-field transition is labelled ζ, the low-field is Ψ and high-field is ϵ. For xy transitions, the half-field is labelled α, the low-field is β and the high-field is γ. If there is a finite E term, then the subscripts x and y will be used to distinguish between the two directions for the α, β and γ transitions. In an ESR measurement of a powdered sample, ESR spectra at different frequencies are made. All the observed transitions (with known field and frequency values) were then fitted to the simultaneous equations in Eq. 2.11 to obtain the single-ion

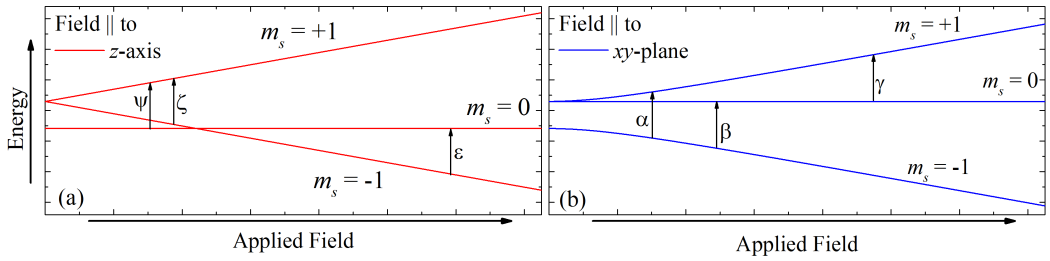

Figure 2.8: Ground state energy level diagram of a D-only $S = 1$ magnetic ion with easy-plane anisotropy which shows the labelling of the transitions in ESR measurements in this project. The field is applied parallel to **(a)** the z-axis and **(b)** xy plane. In the presence of an E term in the Hamiltonian, the xy energy-levels split and α, β and γ resonances will be labelled with x and y subscripts depending on the transition they refer to.

anisotropy parameters and intrinsic g-tensor. Further details of the fitting process can be found in Ref. [30].

It is not possible to obtain the sign of D for powdered $S = 1$ compounds from fitting frequency-dependent ESR data in this manner [12, 116]. This is because the positions of ESR transitions do not change between easy-plane and easy-axis anisotropy. However it is possible to determine the sign of D from observing how the intensities of the resonance peaks changes as the temperature is varied. At very low temperatures, most of the spins occupy the ground state. A transition from this state to an excited state will have a very high intensity. A transition between two excited states will have a very low intensity due to the low occupancy of these energy levels. As the temperature increases, the transition from the ground state will decrease in intensity as spins increasingly occupy the higher energy levels. Transitions between the excited levels will therefore have larger intensities. This can be used to determine the sign of D as the ground state will be different for positive and negative D. For example, the low-field xy (β) transition in Fig. 2.8 is between the ground state $m_s = -1$ and excited $m_s = 0$ level for $D > 0$. At low temperatures it will have a much higher intensity than the high-field xy (γ) transition which is between two excited states. For easy-axis anisotropy, these change. The γ resonance is due to the transition between the ground state $m_s = -1$ and excited $m_s = 0$ level whilst the β transition is now between the excited $m_s = 0$ and $m_s = +1$ levels. The γ resonance will have a much higher intensity than the β transition at low temperatures. Hence, there are two methods to determine the sign of D. The first is the difference in intensity between low and high-field resonances at a given temperature due to transitions with the field aligned along one crystal axes. However, due to the

large magnitudes of D in the compounds in this project, the high-field transitions are often out of the field/frequency range of most spectrometers. In this case the second method can be used: by measuring ESR spectra with the same frequency at different temperature the sign of D can be determined by whether the intensity of one particular resonance increases or decreases.

2.5 Muon-spin spectroscopy

μ-SR stands for muon spin resonance. For low-dimensional quantum magnets, $\mu-$SR has been shown to be sensitive to transitions to long-range order [88, 95–97, 104, 117, 118]. Single crystal and polycrystalline samples were measured using the HIFI spectrometer at ISIS, Rutherford Appleton Laboratory (UK) and the LTF spectrometer at sμ^+s, Paul Scherrer Institut (Switzerland). In both cases the samples were mounted onto a silver backing plate inside the cryostat using Apiezon vacuum grease. The muons at both facilities are created by smashing high energy protons into a carbon target. When a proton collides with a nucleus, charged pions are created. These have a lifetime of 26 ns and decay into a muon and an appropriate neutrino. For stationary pions that decay, the muons that are produced have a relatively low velocity. This allows time for muons to be deposited into the measured sample instead of passing straight through. Another effect of the decay of static pions is that the emerging muons are spin polarised. The pion has no spin, and the neutrino has spin antiparallel to its momentum. To conserve momentum, the muon must also have spin antiparallel to its momentum. Spin-polarised μ^+ ions are then implanted in a sample such that the muons occupy interstitial positions in the crystal lattice [18]. The population of muons then decreases on the time-scale set by their 2.2 μs mean-lifetime. By-products of the muon decay are positrons, which are preferentially emitted parallel to the instantaneous direction of the μ^+ polarisation at the decay event. Two scintillators, positioned in the forward (F) and backward (B) positions relative to the μ^+-beam direction, record the number of positrons as a function of time [$N_i(t)i$ =F, B] during an experiment. The asymmetry, $A(t)$, parametrises the preferred direction of positron emission via

$$A(t) = \frac{N_F(t) - \alpha N_B(t)}{N_F(t) + \alpha N_B(t)} \tag{2.12}$$

where α is an experimental calibration constant accounting for differences in the detectors.

The asymmetry is proportional to the muon polarisation along the beam direction, $p_z(t)$. Muons coherently precess about the local field at the interstitial

sites (**B**) with an angular frequency $\gamma_\mu \mathbf{B}$, where γ_μ is the gyromagnetic ratio for muons. If the direction of **B** with respect to the initial muon polarization direction is random, then averaging over all angles, $\langle p_z(t) \rangle$ varies as [18]:

$$\langle p_z(t) \rangle = \frac{1}{3} + \frac{2}{3} \cos\left(\gamma_\mu |B| t\right). \tag{2.13}$$

The asymmetry is therefore sensitive to two features which signal the onset of long-range order: an oscillatory term given by the coherent precession of $\approx 2/3$ of the implanted muons, which initially had a polarization perpendicular to the local direction of the field at the muon site; and a time-independent "1/3-baseline" from the remaining muons whose polarization was initially along the field direction.

If the strength of the magnetic field at each muon site is taken from a Gaussian distribution of width Δ/γ_μ centred around zero, then averaging over this distribution gives

$$\langle p_z(t) \rangle = \frac{1}{3} + \frac{2}{3} e^{-\Delta^2 t^2/2} \left(1 - \Delta^2 t^2\right). \tag{2.14}$$

This is the Kubo-Toyabe model which describes the evolution of the asymmetry function in a paramagnet, where individual moments and therefore the internal magnetic field point in random directions throughout the sample [119]. On the other hand, a sample exhibiting long-range order contains a uniform and static internal field. The implanted muons will precess at one particular frequency if they are injected into the same site in the unit cell each time. This causes oscillations in $A(t)$. For muons settling in different sites which have a different magnitude of the internal field, the asymmetry will have the form:

$$A(t) = \sum_{i=1}^{n} A_i(0) \left[p_i \mathrm{e}^{-(\lambda_i t)} \cos\left(2\pi \nu_i t\right) \right] \tag{2.15}$$

where there are n oscillatory components with frequency ν_i, relaxing component λ_i and initial asymmetry $A_i(0)$. The temperature dependence of the frequencies of the oscillation can be used to determine the ordering temperature.

2.6 Scattering techniques

X-ray and neutron scattering in condensed matter occur due to different interactions within a sample. X-rays consist of oscillating electric and magnetic fields and therefore interact with the electrons electrons surrounding each atom. X-rays also have a similar wavelength to typical interplanar spacings in coordinations polymers,

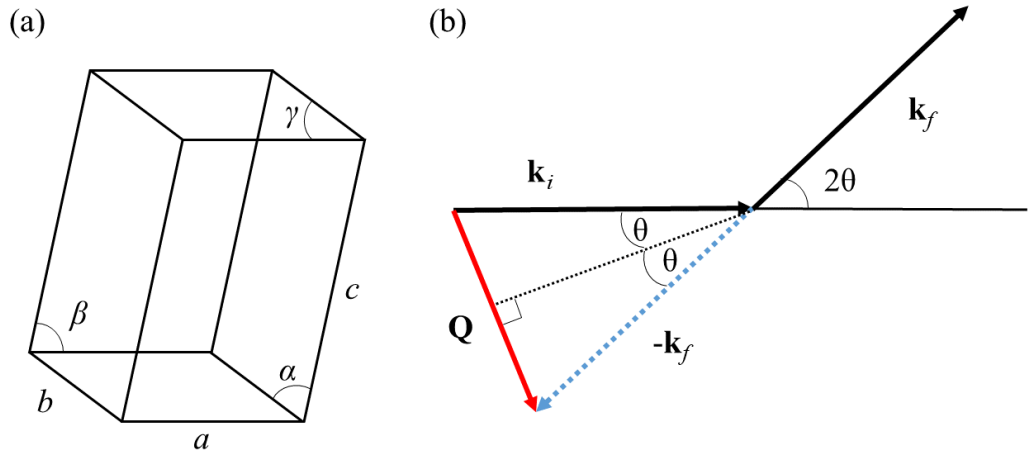

Figure 2.9: **(a)** Diagram of a generic unit cell with crystal axes a, b and c, and angles between them α, β and γ labelled. **(b)** Elastic scattering vector diagram with $|\mathbf{k}_i| = |\mathbf{k}_f|$ through an angle of 2θ.

and therefore scatter off these planes. This makes x-rays highly suited to determining the unit cell and lattice constants [Fig. 2.9(a)]. Neutrons on the other hand are charge neutral but interact with nuclei through the strong force. Neutrons also have a magnetic moment. This allows it to interact via a spin-based dipole-dipole interaction with unpaired electrons. Both of these interactions in tandem can be used to study the unit cell and the ground state magnetic structure of a compound.

Elastic neutron scattering measurements in this project were made using the WISH instrument at the ISIS facility, Rutherford Appleton Laboratory (UK). WISH is a long wavelength diffractometer designed for powder diffraction at long d-spacing. At ISIS, high energy protons are directed at a tantalum target. When a proton collides with a nucleus in the target, it produces an intranuclear cascade which raises the energy level of the nuclei. To release energy, the nuclei evaporate nucleons. Most of these are neutrons, some of which leave the target and are directed through a 100 K solid methane moderator. This slows down the neutron to allow interactions within the sample. The scattered neutron is then detected using pixellated ^{3}He detectors covering a scattering angle in the range of $10° \leq \theta \leq 170°$

The scattering of an x-ray photon or neutron is characterised by the resultant change in momentum $\mathbf{P}$ and energy E. A particle incident with wavevector $\mathbf{k}_i$ and angular frequency w_i which scatters inside of a sample emerges with a final wavevector $\mathbf{k}_f$ and angular frequency w_f. The momentum transfer is expressed as

$$\mathbf{P} = \hbar\mathbf{k}_i - \hbar\mathbf{k}_f = \hbar\mathbf{Q}, \tag{2.16}$$

and energy transfer

$$E = \hbar w \tag{2.17}$$

where $\hbar = h/2\pi$ is the Planck constant and $w = w_i - w_f$. In this thesis, only elastic scattering is used. This means that there is no exchange of energy between the incident photon/neutron and the sample and therefore:

$$E = w = 0. \tag{2.18}$$

Due to Eq. 2.18, the magnitude of the wavevector and therefore the wavelength is unchanged on scattering

$$|\mathbf{k}_i| = |\mathbf{k}_f| = \frac{2\pi}{\lambda}, \tag{2.19}$$

which holds for both neutrons and x-ray photons. The triangle represented by Eq. 2.19 is isosceles (Fig. 2.9) and therefore

$$|\mathbf{Q}| = \frac{4\pi \sin\theta}{\lambda}. \tag{2.20}$$

This can be related to the wavevector transfer from X-rays or neutrons incident onto a vast array of parallel atomic planes a distance d apart:

$$|\mathbf{Q}| = \frac{2\pi N}{d} \ = \frac{4\pi \sin\theta}{\lambda}, \tag{2.21}$$

yielding Bragg's law

$$N\lambda = 2d\sin\theta \tag{2.22}$$

where N denotes the order of the reflections with respect to the straight through beam ($N = 0$). When applied to a compound in powdered form, a large amount of Bragg peaks with different intensities will appear in the diffraction pattern which correspond to the many atomic planes with different d-spacings and orientations. By fitting these peaks, the structure of the sample can be obtained. In the analysis of elastic neutron scattering measurements on a powdered sample in this thesis, there are overlapping peaks with slightly different d-spacings. This can make it difficult to fit as it can be hard to determine the position, lineshape and linewidth of each individual peak. However, prior structural information gained from x-ray measurements can be used as a starting point. The x-ray structural parameters can then be refined to obtain the neutron structural parameters. This is known as the LeBail method [120].

Chapter 3

Determining the magnetic properties of powdered Ni^{2+} complexes

3.1 Introduction

Low-dimensional $S = 1$ quantum magnets have been used as the basis of many experimental studies into novel magnetism [62, 106, 121]. However, further investigations require synthesis of new compounds. Generally, such systems are initially only available as powders. This causes problems when characterising their magnetic properties. This issue is enhanced if the magnitude of the single-ion anisotropy is at a similar energy scale to the strength of magnetic interactions [13, 122]. The powdered nature of the samples causes a loss of information due to the scrambling of the crystal axes with respect to the applied field. Though single crystals solve this issue, attempts to produce crystals large and pure enough for measurements take a lot of time and effort. Thus, it is necessary to know if it is worth pursuing such projects on new, though still powdered, $S = 1$ materials.

A previous study accurately characterised the magnetic ground state of the powdered $S = 1$ Q1D AFM $[Ni(HF_2)(pyz)_2](SbF_6)$ using elastic and inelastic neutron scattering [13]. Pulsed-field magnetisation measurements and numerical modelling of experimental variables were also used to supplement the analysis. However, neutron scattering and pulsed-field techniques are expensive in both time and money as they may require travel to specialist facilities, assuming the relevant proposal is accepted. Neutron scattering measurements also require large amounts of deuterated sample, which can be highly challenging to obtain in new compounds

containing organic molecules. Hence the focus of this chapter will be on the analysis of powdered $S = 1$ AFMs using readily-available, lab based equipment. The aim is to extract enough information on the measured system to determine if further, more time consuming experiments or synthesis of single crystals are necessary. The method used in Ref. [13] is therefore extended to include magnetisation and heat capacity measurements that can be performed at non-specialist institutions.

The compounds studied in this chapter are described by the general $S = 1$ Hamiltonian:

$$\hat{\mathcal{H}} = D\sum_i \hat{S}_i^{z\,2} + E\sum_i \left(\hat{S}_i^{x\,2} - \hat{S}_i^{y\,2}\right) + J\sum_{\langle i,j\rangle} \hat{\boldsymbol{S}}_i \cdot \hat{\boldsymbol{S}}_j + J_\perp \sum_{\langle i,j'\rangle_\perp} \hat{\boldsymbol{S}}_i \cdot \hat{\boldsymbol{S}}_{j'} + \mu_\mathrm{B}\mu_0 \sum_i \boldsymbol{H}\cdot\boldsymbol{g}\cdot\hat{\boldsymbol{S}}_i, \tag{3.1}$$

where J is the magnetic exchange interaction between Ni^{2+} ions within a chain or plane and $J_\perp$ is the exchange interaction perpendicular to J. Angular brackets denote a sum over unique pairs of metal ions and a primed index indicates an ion in an adjacent chain or plane, D and E are the axial and rhombohedral single-ion anisotropy parameters and the final term is the Zeeman splitting.

I have used DC susceptibility, pulsed-field magnetisation and heat capacity measurements of the isolated compounds $[Ni(3,5\text{-lut})_4(H_2O)_2](BF_4)_2$, $Ni(SiF_6)(H_2O)(4\text{-mepz})_4$ and $Ni(H_2O)_2(acetate)_2(4\text{-picoline})_2$ to determine which experimental techniques are suited to determining the effects of single-ion anisotropy in powdered D and E only spin-1 systems. Though the pulsed-field technique is not easily accessible, the maximum applied fields required were no more than 20 T, which are within the reach of commercially available superconducting magnets. I then checked the reliability with which the single-ion anisotropy parameters can be obtained at readily available fields by using high-field ESR measurements. Using what has learnt from studying these systems, I will attempt to characterise the magnetic parameters of the Q2D AFM $[Ni(pyz)_2(H_2O)_2](BF_4)_2$ using similar techniques. A final confirmation of the characterisation method was made by comparing the results with muon-spin relaxation and elastic neutron scattering measurements. Table. 3.1 shows which measurements were made on each sample. I finished by explaining how the single-ion anisotropy changes with structure and composition and compared this with theory [34, 35].

Table 3.1: Table showing which experimental techniques were used to study each compound in this chapter. Red ticks correspond to measurements I have made and analysed. Blue ticks represent measurements analysed by me but not performed by me. μ-SR data was collected and analysed by Fan Xiao, Tom Lancaster, Robert Williams and Stephen Blundell. I participated in the elastic neutron scattering (ENS) experiment, but the analysis were performed Roger Johnson, University of Oxford.

Compound	$\chi(T)$	$M(H)$	$C_p(T)$	ESR	μ-SR	ENS
$[Ni(3,5\text{-lut})_4(H_2O)_2](BF_4)_2$	✓	✓	✓	✓		
$Ni(SiF_6)(H_2O)(4\text{-mepz})_4$	✓	✓		✓		
$Ni(H_2O)_2(acetate)_2(4\text{-picoline})_2$	✓	✓	✓			
$[Ni(pyz)_2(H_2O)_2](BF_4)_2$	✓	✓	✓		✓	✓

3.2 Structures

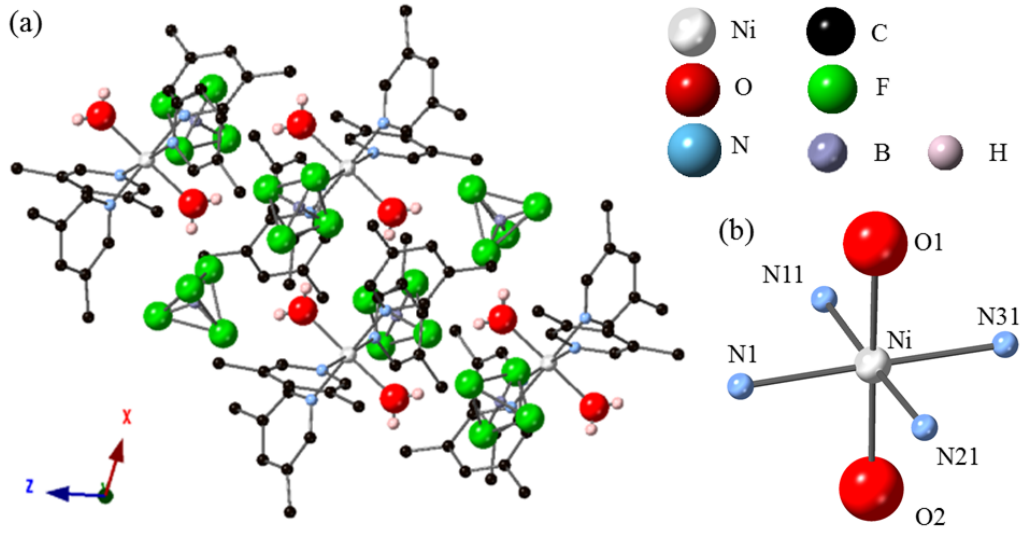

Figure 3.1: **(a)** 100 K structure of $[Ni(3,5\text{-lut})_4(H_2O)_2](BF_4)_2$ contains $Ni(3,5\text{-lut})_4(H_2O)_2$ molecular complexes separated by two BF_4^- ions and stacked along the [101] direction. Lutidine hydrogens are omitted for clarity. **(b)** Local environment around each nickel ion for both $[Ni(3,5\text{-lut})_4(H_2O)_2](BF_4)_2$ and $[Ni(pyz)_2(H_2O)_2](BF_4)_2$. Bond distances are given in Table 3.2.

Single-crystal x-ray diffraction measurements of $[Ni(3,5\text{-lut})_4(H_2O)_2](BF_4)_2$ at 100 K were performed by John Schlueter and Yu-shen Cheng on the 15-ID-B beamline at the Advanced Photon Source, Argonne, USA. The size of the measured crystal was of the order of 100 μm. The monoclinic $[Ni(3,5\text{-lut})_4(H_2O)_2](BF_4)_2$ contains distorted NiN_4O_2 octahedrons (Table 3.2), with four equatorial nitrogen atoms

Table 3.2: Structural parameters of $[Ni(H_2O)_2(3,5\text{-lut})_4](BF_4)_2$ and $[Ni(pyz)_2(H_2O)_2](BF_4)_2$.

Compound	$[Ni(3,5\text{-lut})_4(H_2O)_2](BF_4)_2$	$[Ni(pyz)_2(H_2O)_2](BF_4)_2$
Crystal system	Monoclinic	tetragonal
Space group	$P2_1/n$	$I4/mcm$
a (Å)	12.2611(8)	9.91670(18)
b (Å)	17.0125(12)	9.91670(18)
c (Å)	16.7006(11)	14.8681(4)
NN Ni-Ni (Å)[a]	9.184	6.979
NNN Ni-Ni (Å)[b]	9.754	7.401
Ni-O1 (Å)	2.099(2)	2.050(7)
Ni-O2 (Å)	2.08(2)	2.050(7)
Ni-N1 (Å)	2.110(3)	2.1724(18)
Ni-N11 (Å)	2.105(3)	2.1724(18)
Ni-N21 (Å)	2.094(3)	2.1724(18)
Ni-N31 (Å)	2.115(3)	2.1724(18)

[a] Nearest-neighbour nickel ion distances. For $[Ni(3,5\text{-lut})_4(H_2O)_2](BF_4)_2$ the nearest neighbours are in the [101] crystal direction and for $[Ni(pyz)_2(H_2O)_2](BF_4)_2$ they are within the within the Ni-pyz planes. [b] Next to nearest-neighbour nickel ion distances. For $[Ni(3,5\text{-lut})_4(H_2O)_2](BF_4)_2$ the nearest neighbours are in the [110] crystal direction whilst for $[Ni(pyz)_2(H_2O)_2](BF_4)_2$ this is the distance between nickel ions in adjacent planes.

donated by 3,5-lut molecules and two axial oxygen atoms provided by water molecules (Fig. 3.1). The three bond angles between opposite donor atoms in the nickel octahedra are within the range $176.95° \leq \angle \leq 179.17°$, and the N-Ni-O angle varies from $87.7° \leq \angle \leq 92.4°$ (Table 3.2). Two BF_4^- counter ions, hydrogen bonded to water molecules on adjacent complexes, and non-bridging 3,5-lut molecules keep adjacent molecules separated [Fig. 3.1(a)].

Single-crystal x-ray diffraction measurements of $Ni(SiF_6)(H_2O)(4\text{-mepz})_4$ and $Ni(H_2O)_2(acetate)_2(4\text{-picoline})_2$ at 150 K were performed using a Bruker Kappa APEX II CCD-equipped single-crystal diffractometer by Atta Arif at the University of Utah, USA. The size of the measured crystals were of the order of 100 μm. $Ni(SiF_6)(H_2O)(4\text{-mepz})_4$ is a monoclinic system made up of low-symmetry, axially elongated $NiFON_4$ octahdra [Fig. 3.2(a)]. Equatorial nitrogen atoms are donated by the 4-mepz (mepz = methylpyrazolyl; $C_4H_6N_2$) while the axial fluorine and oxygen atoms come from the SiF_6 and water molecules respectively. The nearest neighbour Ni-Ni distance is ≈ 8.5 Å between Ni^{2+} ions in the [101] direction (see Table. 3.3). There appears to be weak hydrogen bonding between an SiF_6 molecule coordinated to one nickel ion and a water molecule coordinated to an adjacent nickel ion in the [-110] direction.

$Ni(H_2O)_2(acetate)_2(4\text{-picoline})_2$ contain slightly axially elongated NiN_2O_4

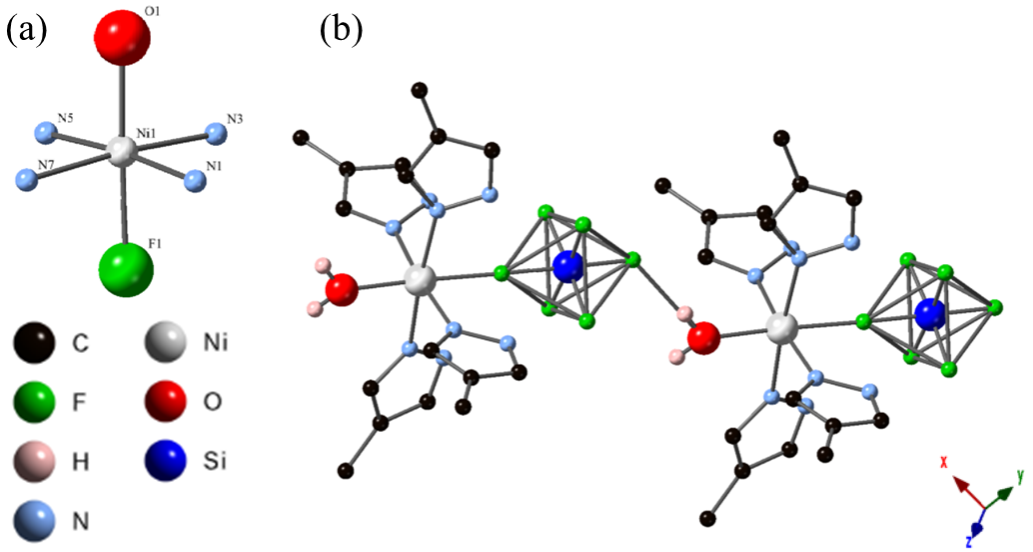

Figure 3.2: 150 K structure of $Ni(SiF_6)(H_2O)(4\text{-mepz})_4$. **(a)** Local environment around each Ni^{2+} ion. **(b)** The $NiFON_4$ octahedra are arrayed with an SiF_6 molecule coordinated to one Ni^{2+} ion hydrogen bonded to one water molecules coordinated to an adjacent Ni^{2+} ion. Mepz hydrogen atoms are omitted for clarity

octahedrons [Fig. 3.3(a)]. These are made up of two axial nitrogen atoms donated by the 4-picoline molecules (picoline = $CH_3C_5H_5N$) and four equatorial oxygen atoms, two donated by acetate (acetate = CH_3COO^-) molecules and the other two from water molecules. All ligands are non-bridging. The bond lengths within the NiN_2O_4 octahedron is shown in Table. 3.3. The bond lengths are different for all three crystal directions. $Ni(H_2O)_2(\text{acetate})_2(\text{4-picoline})_2$ units are kept separated in the crystal b (y) direction via acetate molecules and in the c (z) direction by the 4-picoline molecules [Fig. 3.3(b)]. Water molecules point in the a (x) direction. The Ni-Ni nearest neighbour distance is 7.631 Å which occurs between adjacent Ni^{2+} ions in the xy-plane.

X-ray diffraction measurements of powdered $[Ni(pyz)_2(H_2O)_2](BF_4)_2$ at room temperature were performed by Saul Lapidus on the 11-BM beamline at the Advanced Photon Source, Argonne, USA. $[Ni(pyz)_2(H_2O)_2](BF_4)_2$ is a tetragonal crystal system consisting of sheets of Ni^{2+} ions in the $ab(xy)$-plane linked via pyrazine ligands in a square planar arrangement [Fig. 3.4(a)]. Water molecules keep the planes separated in the $c(z)$ direction. The metal centres occupy axially compressed NiN_4O_2 octahedra [Fig. 3.1(b)], with the equatorial nitrogen atoms deriving from the pyrazine network and oxygen atoms donated from the H_2O ligands. Opposite Ni-ligand bonds in the nickel octahedra are all 180° whilst all N-Ni-O and N_x-Ni-N_y

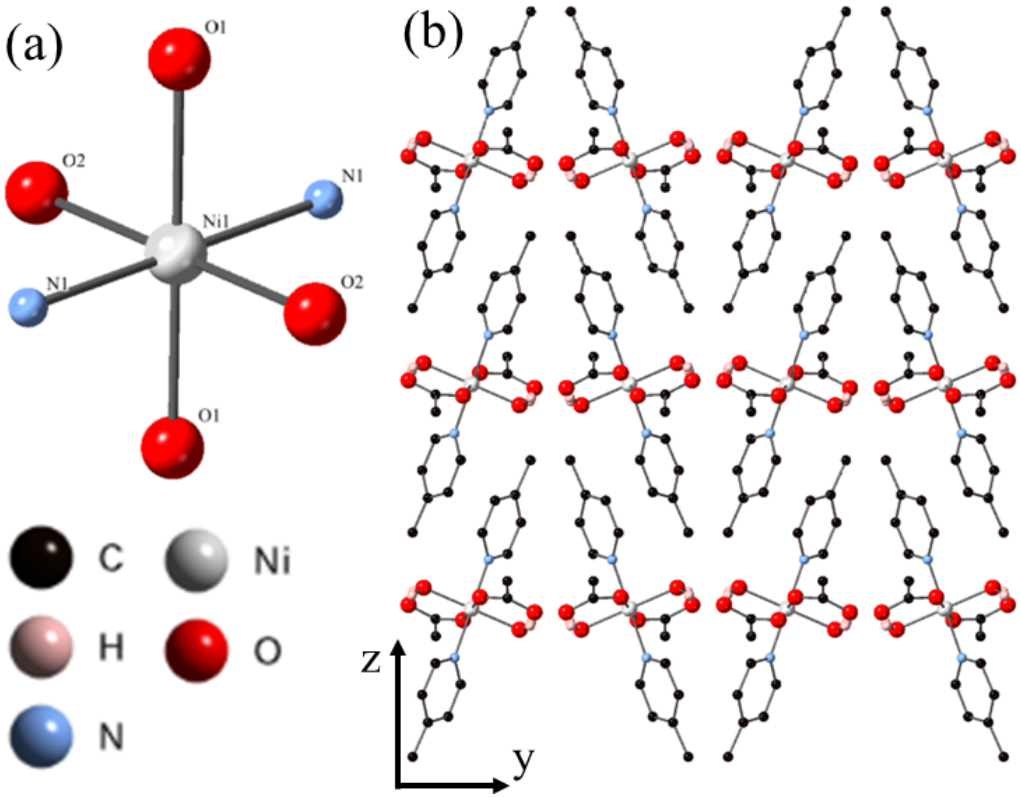

Figure 3.3: 150 K structure of $Ni(H_2O)_2(acetate)_2(4\text{-picoline})_2$. **(a)** The NiN_2O_4 octahedron. **(b)** Arrangements of $Ni(H_2O)_2(acetate)_2(4\text{-picoline})_2$ complexes in the yz plane. Water molecules in the x direction keep these planes separated.

angles are 90°. The H_2O ligands are non-bridging, and in conjunction with a spacer layer of BF_4^- counter ions act to keep the sheets well separated [Fig. 3.4(b)]. The hydrogen atoms in the water molecules can occupy four equally probable positions, all of which are shown in Fig. 3.4(b).

The nearest-neighbour Ni-Ni distance is larger in $[Ni(3,5\text{-lut})_4(H_2O)_2](BF_4)_2$ compared to $[Ni(pyz)_2(H_2O)_2](BF_4)_2$. The non-bridging lutidine molecules do not lead to any through-bond pathway for magnetic interactions between Ni^{2+} ions in the system. Likewise, $Ni(SiF_6)(H_2O)(4\text{-mepz})_4$ and $Ni(H_2O)_2(acetate)_2(4\text{-picoline})_2$ have no obvious bond pathways to mediate magnetic exchange. Therefore, $[Ni(3,5\text{-lut})_4(H_2O)_2](BF_4)_2$, $Ni(SiF_6)(H_2O)(4\text{-mepz})_4$and $Ni(H_2O)_2(acetate)_2(4\text{-picoline})_2$ are expected to be well modelled by the Hamiltonian described in Eq. 3.1, with $J = J_\perp = 0$. It is likely that there is a significant E term due to the inequivalence of the x and y axes around each Ni^{2+} ion [33].

Table 3.3: Structural information and bond lengths for $Ni(SiF_6)(H_2O)(4\text{-mepz})_4$ and $Ni(H_2O)_2(acetate)_2(4\text{-picoline})_2$. See Fig. 3.2 and Fig. 3.3 for the location of the ligands bonded to the Ni^{2+} ion.

Compound	$Ni(SiF_6)(H_2O)(4\text{-mepz})_4$	$Ni(H_2O)_2(acetate)_2(4\text{-picoline})_2$
Structure	Monoclinic	Orthorhombic
Space group	$C1c1$	$Pcab$
Ni- (Å)	N1 = 2.0658(19)	N1 = 2.107(3)
Ni- (Å)	N3 = 2.089(2)	N1 = 2.107(3)
Ni- (Å)	N5 = 2.068(2)	O1 = 2.073(2)
Ni- (Å)	N7 = 2.096(2)	O1 = 2.073(2)
Ni- (Å)	F1 = 2.1260(12)	O2 = 2.059(2)
Ni- (Å)	O1 = 2.5038(17)	O2 = 2.059(2)
a (Å)	12.7840(6)	8.8996(3)
b (Å)	14.2862(6)	12.3995(4)
c (Å)	13.5967(6)	17.6516(7)

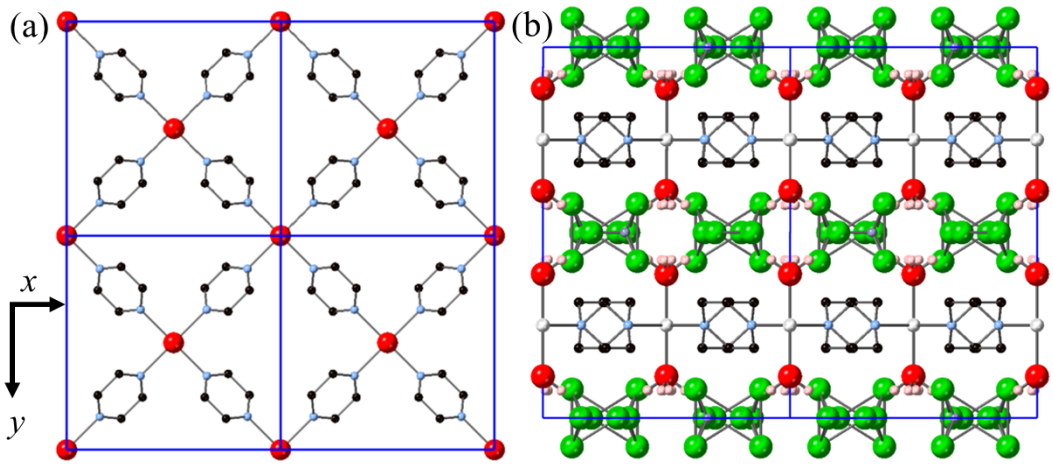

Figure 3.4: Room temperature structure of $[Ni(pyz)_2(H_2O)_2](BF_4)_2$. (**a**) $[Ni(pyz)_2]^{2+}$ sheets. (**b**) Sheets are stacked directly above each other along c. Non-coordinated BF_4^- counter-ions keep the layers well separated. Each of the water hydrogen atoms occupies one of four equally probable locations. Pyrazine hydrogen atoms are omitted for clarity. The key is located in Fig. 3.1

Pyrazine is known as a good mediator of magnetic exchange [1, 88]. Also, the x and y axes around each Ni^{2+} ion in $[Ni(pyz)_2(H_2O)_2](BF_4)_2$ are equivalent. The structure of $[Ni(pyz)_2(H_2O)_2](BF_4)_2$ therefore suggests that each Ni^{2+} ion in this material can be represented using Eq. 3.1 with $J \neq 0$ and $E = 0$. As the inter-plane distances are larger than the intra-plane distances with no direct bridging between nickel ions in adjacent planes, it is assumed that $J_\perp \ll J$ for $[Ni(pyz)_2(H_2O)_2](BF_4)_2$ in the analysis below. Single-ion anisotropy is a crystalline-electric field effect and is dependent on the environment around the magnetic ion. $[Ni(pyz)_2(H_2O)_2](BF_4)_2$ contains a comparable local octahedra around the Ni^{2+} ions to $[Ni(3,5\text{-lut})_4(H_2O)_2](BF_4)_2$, though $[Ni(3,5\text{-lut})_4(H_2O)_2](BF_4)_2$ has lower tetragonal symmetry. This can therefore be used to investigate the structural dependence of D in for Ni^{2+} ions in octahedral environments.

3.3 Isolated Ni^{2+} systems

3.3.1 $[Ni(3,5\text{-lut})_4(H_2O)_2](BF_4)_2$

Magnetometry

Pulsed-field magnetisation measurements of powdered $[Ni(3,5\text{-lut})_4(H_2O)_2](BF_4)_2$ rise smoothly towards a broad saturation [Fig. 3.5(a)]. The differential susceptibility [Fig. 3.5(b)] becomes steeper on cooling, and develops a very weak maximum at $\mu_0 H_C = 6.0 \pm 0.6$ T at 0.63 K. This feature has previously been observed in polycrystalline Ni^{2+} coordination polymers [101] and is attributed to the ground state energy level crossing between the $m_s = 0$ and $m_s = -1$ levels when a magnetic field is applied parallel to the z-axis [101]. This occurs in isolated $S = 1$ easy-plane systems ($D \gg J$) and causes a sharp rise in $M_z(H)$. As the data in Fig. 3.5 was measured on a powder, the peak in $\mathrm{d}M/\mathrm{d}H$ is weakened substantially such that it is difficult to accurately determine the position of the maximum. Therefore, by differentiating $\mathrm{d}M/\mathrm{d}H$ again, H_C is found from the midpoint of the differential peak shape in $\mathrm{d}^2M/\mathrm{d}H^2$ [Fig. 3.5(c)]. Using Eq. 2.2, an estimate of $\sqrt{D^2 - E^2} = +9.0 \pm 0.9$ K is obtained.

DC susceptibility measurements of $[Ni(3,5\text{-lut})_4(H_2O)_2](BF_4)_2$ (Fig. 3.6) show a slow rise in $\chi(T)$ as the temperature is lowered until $T \approx 3$ K, where the data starts to flatten out. As the analysis of the magnetisation measurements suggests that $D \gg J$, the data was fitted to a D and E only model [32, 101] which includes a temperature independent diamagnetic term χ_0. Values of $D = +8.69(3)$ K, $E = 1.3(1)$ K, $g = 2.24(1)$ and $\chi_0 = -8.5(1.0) \times 10^{-9}$ m^3mol^{-1} were extracted.

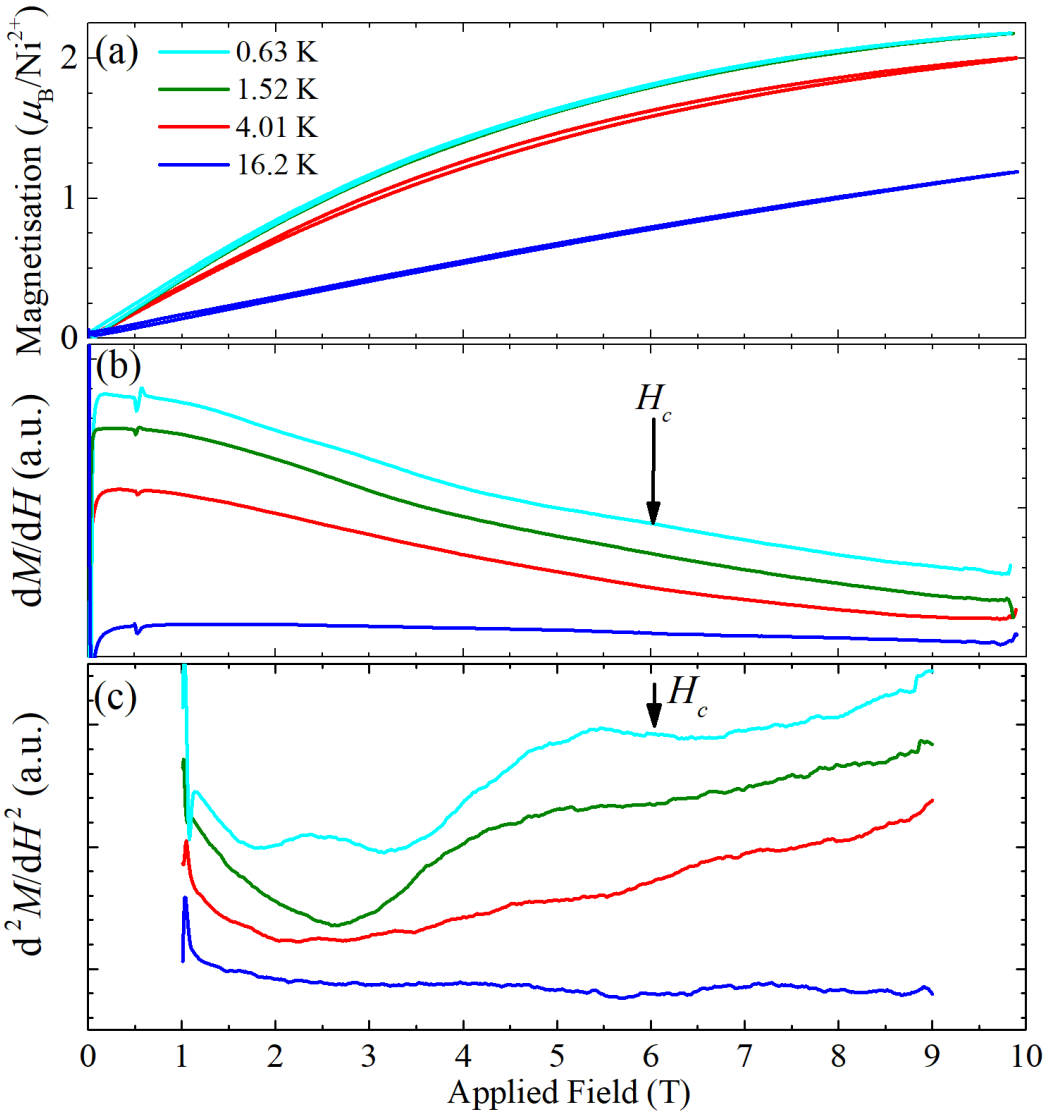

Figure 3.5: **(a)** Pulsed-field magnetization and **(b)** differential susceptibility data of $[Ni(3,5\text{-lut})_4(H_2O)_2](BF_4)_2$, calibrated using DC SQUID magnetometry. **(c)** Gradient of the differential susceptibility indicates a derivative shape which develops on cooling to 0.63 K. The centre of this feature (arrow) marks H_C (see text).

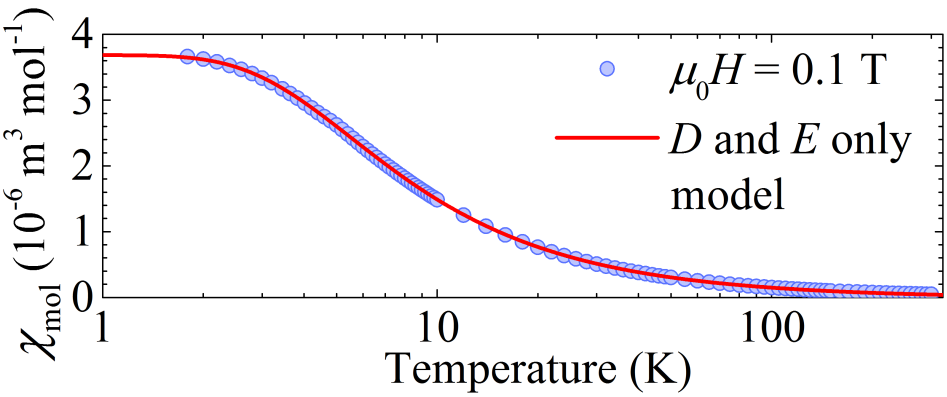

Figure 3.6: DC susceptibility measurements of powdered $[Ni(3,5\text{-lut})_4(H_2O)_2](BF_4)_2$ made at a field of 0.1 T. The data was fitted to a D and E only model with a small, temperature independent diamagnetic term.

The model is in good agreement with the data over the whole temperature range. The values of D and E gives a magnitude of $\sqrt{D^2 - E^2}$ that is within the error of the value obtained from the pulsed-field measurement. If D is allowed to be negative, then the resultant fitted value of E does not meet the condition $|D| > 3E$. This, along with the presence of the bump in the pulsed-field differential susceptibility data, strongly suggests that $[Ni(3,5\text{-lut})_4(H_2O)_2](BF_4)_2$ is easy-plane.

Heat capacity

Zero-field heat capacity measurements of powdered $[Ni(3,5\text{-lut})_4(H_2O)_2](BF_4)_2$ pressed into a pellet are shown as $C_p/T(T)$ in Fig. 3.7. The data shows two peaks, one between 40 and 50 K which is due to phonons, and a second at ≈ 3 K which is attributed to a Schottky anomaly. The latter feature occurs due to thermal excitations between two energy states. If present in the zero-field measurements, it is a sign of single-ion anisotropy in the sample. In between these two peaks is a region where there are significant contributions from both single-ion anisotropy and lattice phonons. Due to this, it is very difficult to model the lattice phonons accurately without including contributions from the single-ion anisotropy. This can be overcome by fitting the whole data range to a model incorporating lattice phonons and single-ion anisotropy.

The heat capacity of an N-level system is given by [25]

$$C_p = k_B T \left[2 \left(\frac{\partial \ln Z}{\partial T} \right) + T \left(\frac{\partial^2 \ln Z}{\partial T^2} \right) \right], \tag{3.2}$$

where the partition function Z is

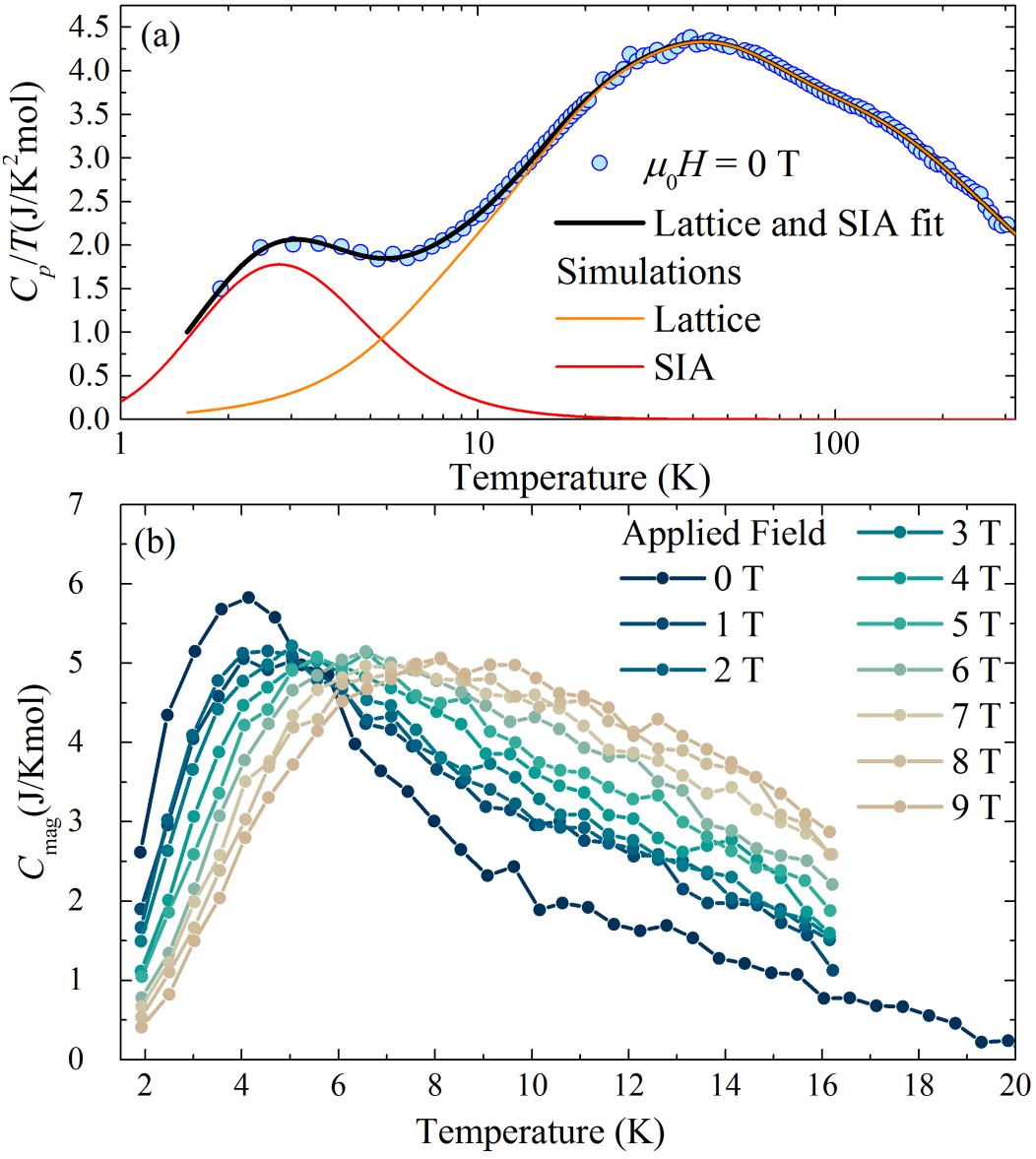

Figure 3.7: Heat capacity measurements of $[Ni(3,5\text{-lut})_4(H_2O)_2](BF_4)_2$. **(a)** Zero-field measurements presented as C_p/T. The whole data range is fitted to a model incorporating contributions from lattice phonons (Eq. 2.1) and single-ion anisotropy (Eq. 3.5). The parameters obtained are shown in Table. 3.4. **(b)** Magnetic heat capacity, resulting from the subtraction of C_{latt}, as a function of temperature at fields in the range $0 \leq \mu_0 H \leq 9$ T.

Table 3.4: Parameters obtained from the lattice and single-ion anisotropy fit to zero-field heat capacity measurements of $[Ni(3,5\text{-lut})_4(H_2O)_2](BF_4)_2$ [Fig. 3.6(a)].

Parameter	Value
A_{D}	53(3) J/Kmol
θ_{D}	50(1) K
A_{E1}	128(5) J/Kmol
θ_{E1}	87(3) K
A_{E2}	199(5) J/Kmol
θ_{E2}	195(7) K
A_{E3}	387(6) J/Kmol
θ_{E3}	540(9) K
D	10.4(1) K
E	2.6(2) K

$$Z = \sum_{\alpha}^{N} \mathrm{e}^{-\beta E_{\alpha}}. \tag{3.3}$$

For spin-1 systems with non-zero D and E, the three m_s energy levels are separated by $D - E$ and $2E$ in zero-field (Fig. 2.8). For easy-plane anisotropy, the $m_s = 0$ state has the lowest energy. For easy-axis anisotropy, the $m_s = -1$ level is in the ground state. As it is only the difference in energy that is important, setting $m_s = 0$ as E_0, this gives $E_{-1} = \pm|D| - E$ and $E_{+1} = \pm|D| + E$ for all D. As $\pm|D|$ is the same as D, the partition function of a spin-1 D and E only system is

$$Z = 1 + \mathrm{e}^{-\beta(D-E)} + \mathrm{e}^{-\beta(D+E)} = 1 + 2\mathrm{e}^{-\beta D}\cosh(\beta E). \tag{3.4}$$

Substituting Eq. 3.4 into Eq. 3.2, the zero-field heat capacity of a D and E only spin-1 system is thus:

$$C_p = k_{\mathrm{B}} N_{\mathrm{A}} \frac{2\mathrm{e}^{\beta D}\left[\left(D^2 + E^2\right)\cosh(\beta E) - 2ED\sinh(\beta E)\right] + 4E^2}{T^2\left[\mathrm{e}^{\beta D} + 2\cosh(\beta E)\right]^2}. \tag{3.5}$$

This can be used to model both easy-axis and easy-plane anisotropy, with the fitted sign of D being used to distinguish between the two cases. A model incorporating both Eq. 3.5 and Eq. 2.1 was used to fit the data in Fig. 3.7. The parameters extracted are shown in Table. 3.4. The model is in good agreement with the data over the whole range. The values of $D = +10.4(1)$ K and $E = 2.6(2)$ K are consistent with the magnetometry measurements. If D is allowed to be negative, then fitted value of E doesn't meet the condition $|D| > 3E$. The lattice parameters

in Table. 3.4 were then used to subtract the lattice contribution from the total heat capacity to obtain the field dependence of the magnetic heat capacity of [Ni(3,5-lut)$_4$(H$_2$O)$_2$](BF$_4$)$_2$, shown as $C_{\mathrm{mag}}(T)$ in Fig. 3.7(b). This shows the position of the Schottky anomaly increase in temperature as the field is raised. There is an initial drop in amplitude between 0 and 1 T. As the field is increased further, the amplitude remains relatively constant. Comparing with Fig. 2.5, this is further confirmation of the presence of easy-plane anisotropy in [Ni(3,5-lut)$_4$(H$_2$O)$_2$](BF$_4$)$_2$.

ESR

ESR is the measurement technique most suited to characterising the single-ion anisotropy of quantum magnets. Equipment to perform ESR measurements using low-frequency ($\nu < 100$ GHz) microwaves and low-fields ($\mu_0 H < 4$ T) are commercially available. However, to accurately determine the zero field splitting parameters with $D \gtrsim 10$ K requires much higher frequencies and fields. These require custom built spectrometers at specialist facilities. ESR measurements of [Ni(3,5-lut)$_4$(H$_2$O)$_2$](BF$_4$)$_2$ were therefore made at the National High Magnetic Field Laboratory, Tallahassee, USA. The purpose of these measurements is to confirm the sign and magnitudes of the single-ion anisotropy parameters of [Ni(3,5-lut)$_4$(H$_2$O)$_2$](BF$_4$)$_2$ obtained from magnetometry and heat capacity measurements.

Low-temperature ESR measurements of powdered [Ni(3,5-lut)$_4$(H$_2$O)$_2$](BF$_4$)$_2$ were made at frequencies in the range $100 < \nu < 630$ GHz (Fig. 3.8). Low-frequency data [Fig. 3.8(a)] show the high-field z transition (ϵ) which moves down in field as the frequency increases. The high frequency data shows two large, broad resonances that move to higher fields as the frequency is increased [Fig. 3.8(b)]. These resonances sharpen and get closer together as the frequency is raised. By comparison to previous published ESR data of a powdered $S = 1$ quantum magnet, this suggests that they might be the half-field x and y transitions (α_x and α_y respectively) [101]. There are two, smaller resonances observed at higher fields which are due to the low and high-field x resonances (β_x and γ_x respectively) [Inset to Fig 3.8(a), Fig. 3.8(b)] by comparison to Fig. 2.7.

The positions of these transitions were fitted to a D and E only model [30]. To obtain the best fit, it was found that the high-field resonance of the two large resonances is the low-field y resonance (β_y) for $\nu < 330$ GHz and the α_x transition for $\nu > 330$ GHz. The reason why the β_y transition is not observed at higher frequencies or the α_x transition at lower frequencies is unknown. The low-field resonance is the γ_x transition. The parameters extracted from the fit are $g_x = 2.20(1)$, $g_y = 2.33(2)$, $g_z = 2.05(12)$, $|D| = 10.4(1)$ K and $E = 2.12(4)$ K.

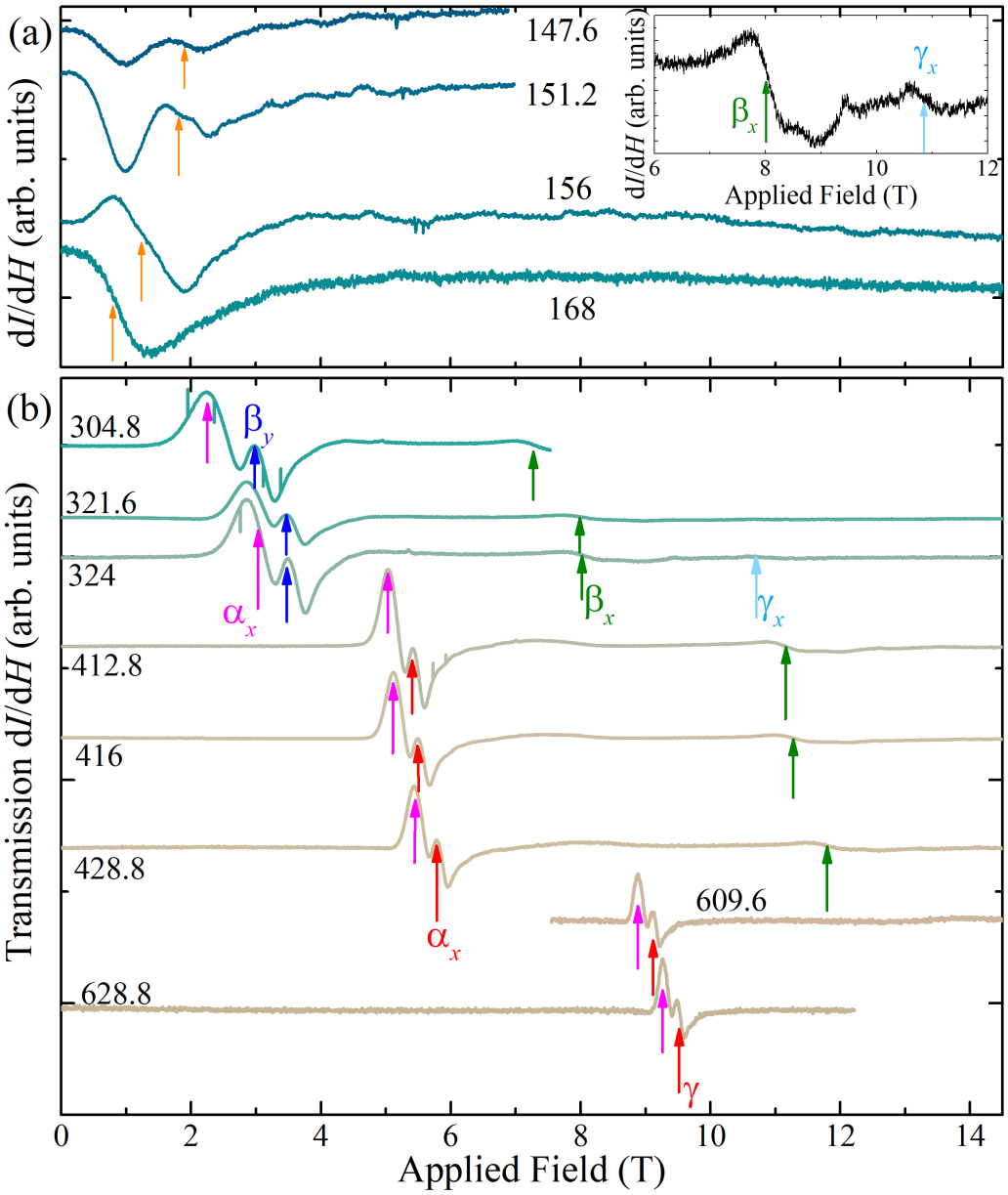

Figure 3.8: ESR measurements of $[Ni(3,5\text{-lut})_4(H_2O)_2](BF_4)_2$ at different frequencies, labelled in GHz and measured at temperatures of ≈ 3 K, apart from the 321.6 and 416 GHz spectra which were recorded at 5 K. Resonances of known transitions are labelled. Spectra were made in the frequency range **(a)** $145 < \nu < 170$ GHz and **(b)** $300 < \nu < 630$ GHz. Inset: 324 GHz spectra showing the β_x and γ_x transition.

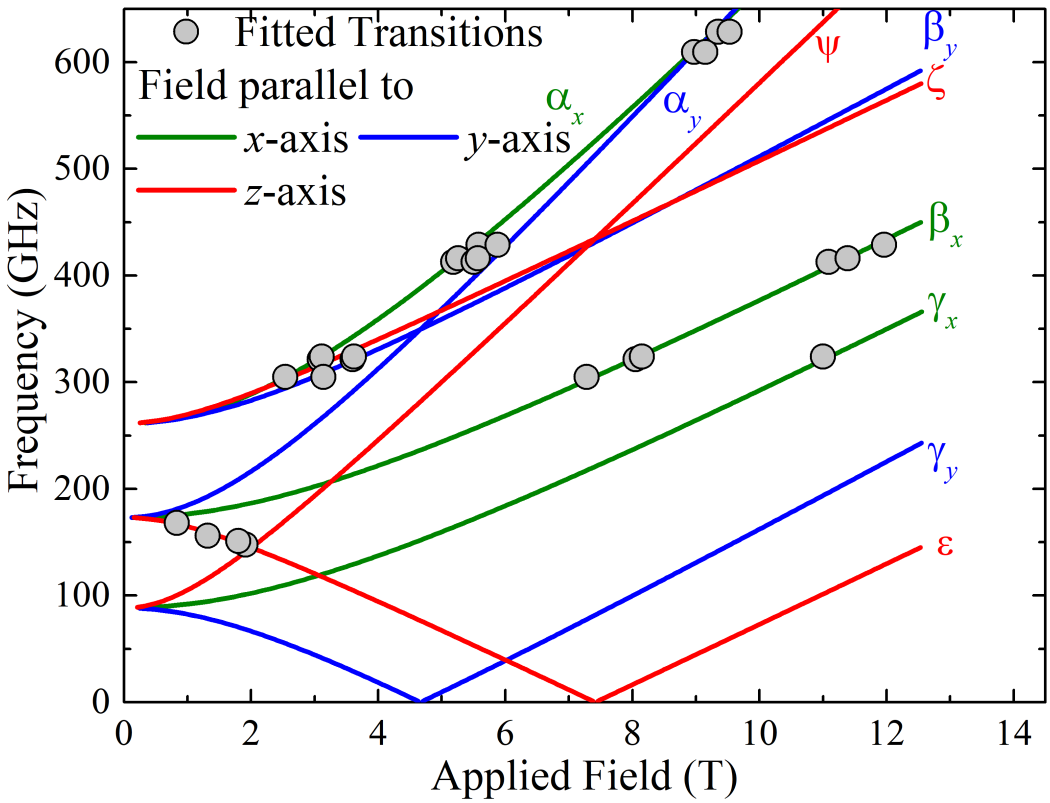

Figure 3.9: Fitting the observed resonances from Fig. 3.8 to a D and E only model with parameters $g_x = 2.20(1)$, $g_y = 2.33(2)$, $g_z = 2.05(12)$, $D = 10.42(7)$ K and $E = 2.12(4)$ K extracted in good agreement with the data.

These parameters are consistent with the experimental data over the whole frequency range of the experiment, and with previous magnetometry and heat capacity experiments. A simulation at $\nu = 412.8$ GHz is shown in Fig. 3.10. It captures the α_x and β_x transitions well. The α_y resonance is also recreated but at a much lower intensity than in the data. The very broad resonance in the data between 7 and 8 T is seen in the simulation but with a much smaller linewidth. The sign of D can be found from a temperature dependent ESR study [Fig. 3.10]. This shows the β_x transition located at 11 T. The β_x resonance decreases in intensity as temperature is increased. The β_x transition is also more intense than the γ_x transition (Inset to Fig. 3.10) at low temperatures. Both of these observations indicate that [Ni(3,5-lut)$_4$(H$_2$O)$_2$](BF$_4$)$_2$ exhibits easy-plane anisotropy. That $g_x > g_z$ is further evidence of easy-plane anisotropy and the value of $\lambda = -139$ K is consistent with theory (see section 1.2.3). ESR measurements of [Ni(3,5-lut)$_4$(H$_2$O)$_2$](BF$_4$)$_2$ confirm the single-ion anisotropy analysis from magnetometry and heat capacity measurements.

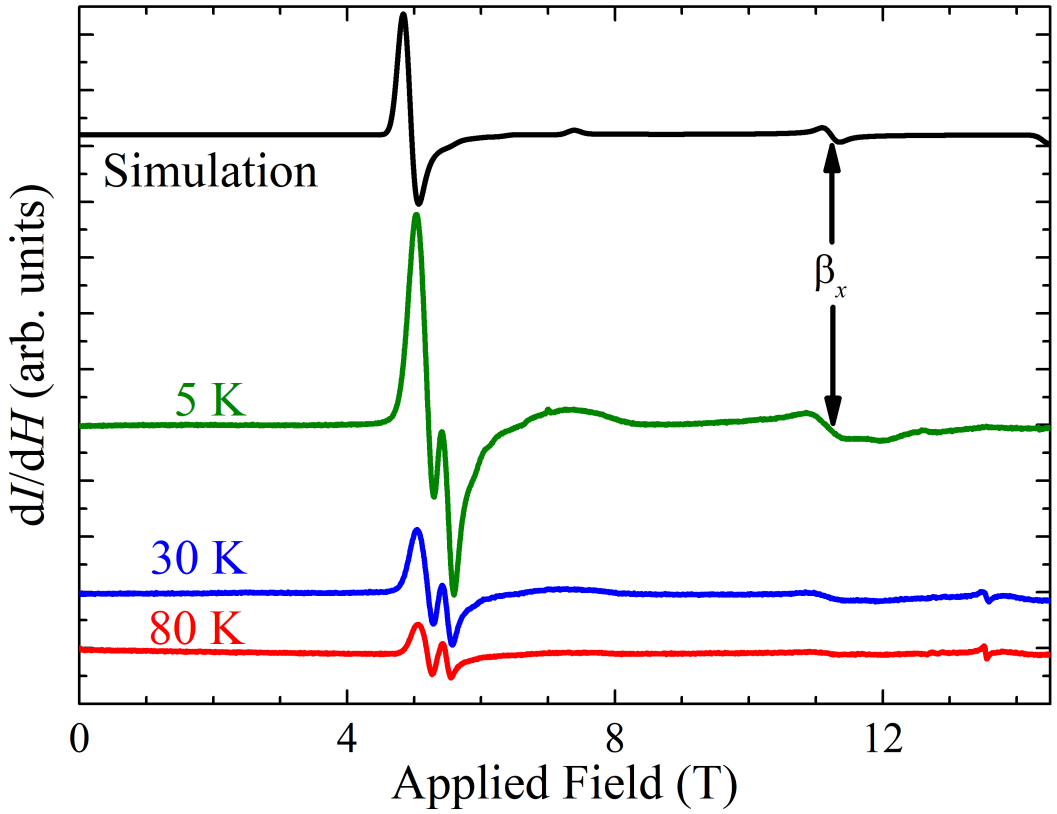

Figure 3.10: Temperature dependent ESR measurements of [Ni(3,5-lut)$_4$(H$_2$O)$_2$](BF$_4$)$_2$ at 5 K (green line), 30 K (red line) and 80 K (blue line) at $\nu = 412.8$ GHz. The black line is an ESR simulation obtained from a fit to all observed resonances [see Fig. 3.9(b)] at 5 K.

3.3.2 Ni(SiF$_6$)(H$_2$O)(4-mepz)$_4$

Magnetometry

Pulsed-field measurements of powdered Ni(SiF$_6$)(H$_2$O)(4-mepz)$_4$ rises slowly to saturation [Fig. 3.11(a)]. The data was calibrated using quasi-static SQUID measurements and shows that Ni(SiF$_6$)(H$_2$O)(4-mepz)$_4$ saturates at 2.25(1)μ_B, which Eq. 1.16 suggests $g = 2.25(1)$. The differential susceptibility at 0.58 K drops smoothly until a weak peak at ≈ 8 T. This is indicative of an easy-plane Ni^{2+} compound with negligible magnetic interactions [101]. The data continues to drop smoothly after the weak peak. The position of H_C is found from the midpoint of the peak derivative shape in the d^2M/dH^2 data and is located at $H_C = 7.8(6)$ T. Using Eq. 2.2, an estimate of $\sqrt{D^2 - E^2} = +11.8(7)$ K is obtained.

DC susceptibility of powdered Ni(SiF$_6$)(H$_2$O)(4-mepz)$_4$(Fig. 3.12) rises as the temperature is lowered until the data starts to plateau below $T = 3$ K. The

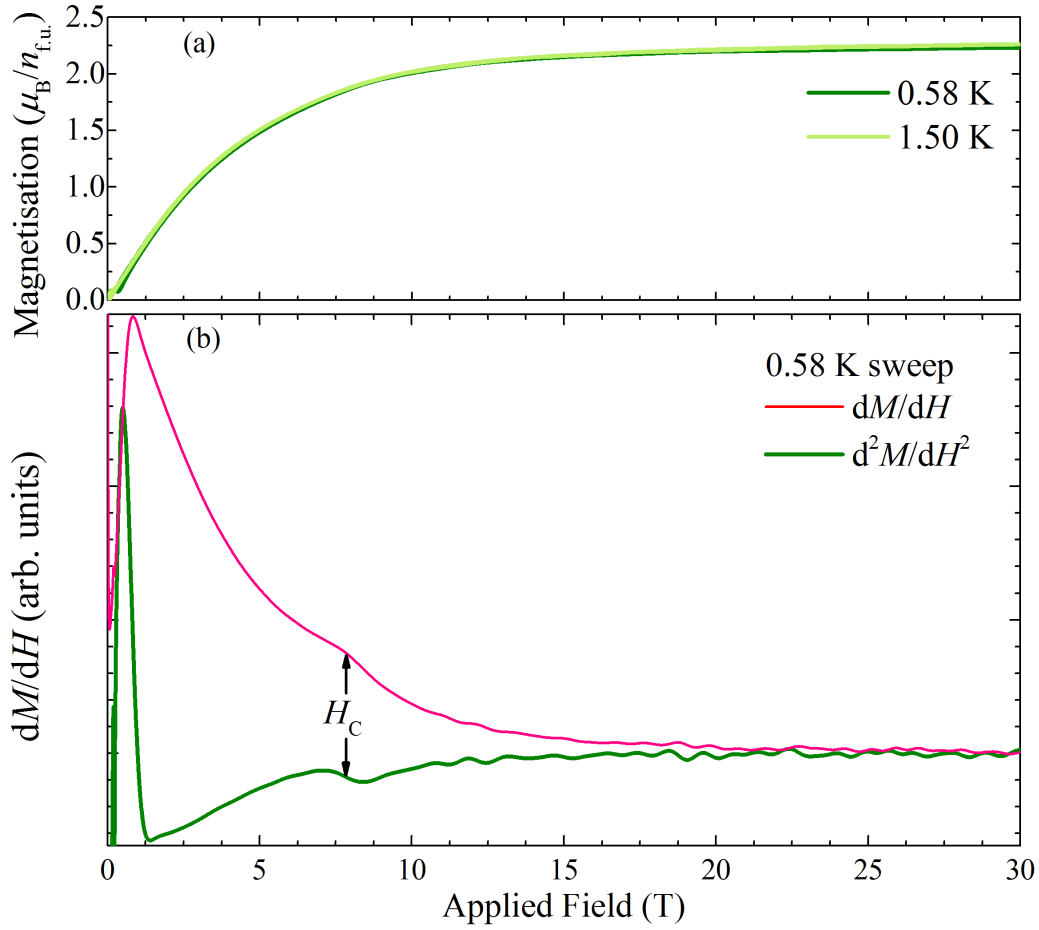

Figure 3.11: **(a)** Low temperature pulsed-field magnetisation measurements, calibrated with SQUID magnetisation measurements, of $Ni(SiF_6)(H_2O)(4\text{-mepz})_4$. **(b)** Differential susceptibility and gradient of the differential susceptibility shows the feature attributed to easy-plane anisotropy at 7.8(6) T.

plateau is suggestive of easy-plane anisotropy [32]. The analysis of the magnetisation measurements indicates $D \gg J$. Therefore a D and E only model is used to fit the data, with the parameters $D = +11.25(2)$ K, $E = 0.6(1)$ K and $g = 2.25(1)$ extracted. These are within the errors of the parameters obtained from the magnetisation measurements.

ESR

Low temperature ESR spectra of powdered $Ni(SiF_6)(H_2O)(4\text{-mepz})_4$ were made in the frequency range $100 \leq \nu \leq 326.4$ GHz [Fig. 3.13(a)]. Two different temperatures were used. The 108, 208 and 325.4 GHz spectra were made at 5 K, all other

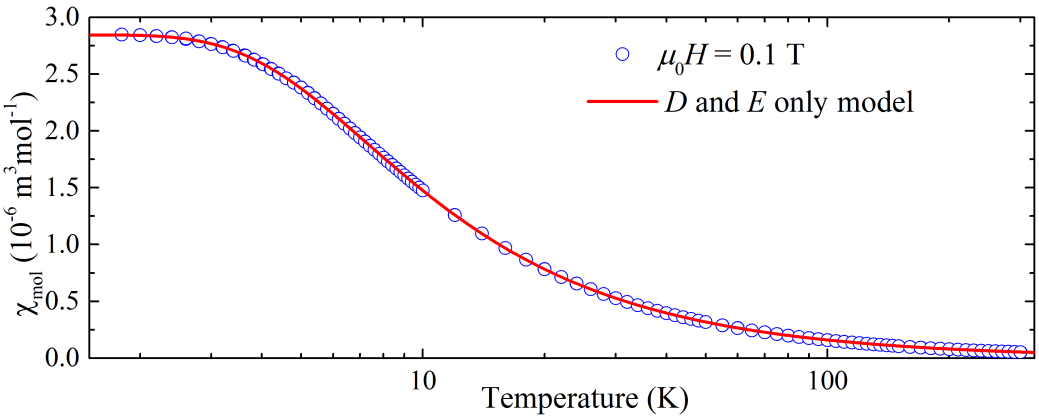

Figure 3.12: DC susceptibility measurement of $Ni(SiF_6)(H_2O)(4\text{-mepz})_4$shows a rise in the data before it plateaus as the temperature is lowered. This was fitted to a D and E only model with the parameters $D = 11.25(2)$ K, $E = 0.57(10)$ K and $g = 2.25(1)$ extracted. The model is in good agreement with the data.

spectra were made at the base temperature of the cryostat (≈ 3 K). Resonances corresponding to high-field x (γ_x) and y (γ_y) transitions are observed in the 104 and 108 GHz sweeps. The high-field z (ϵ) transition is the most intense resonance for $\nu \leq 208$ GHz and gives a direct measure of D by linearly extrapolating the position of the transition at different ν back to zero. The zero-field intercept occurs at $\approx$ 230 GHz, which corresponds to a zero-field splitting energy of ≈ 11 K. The 108 GHz and 208 GHz sweeps were also measured at 30 K and show the ϵ transition decrease in intensity as the temperature is raised [Fig. 3.13(b)]. This is indicative of easy-plane anisotropy in $Ni(SiF_6)(H_2O)(4\text{-mepz})_4$. The γ_y transition is only observed in the high temperature data [Inset to Fig. 3.13(b)] and is further evidence that $D > 0$. The z (Ψ) half-field transition also figures prominently in the low frequency sweeps. For $\nu \geq 230$ GHz, the low field x (β_x), y (β_y) and z (ζ) transitions are observed. Apparent features that likely correspond to the half-field x (α_x) and y (α_y) transitions are positioned to the high-field side of ζ in the 326 GHz spectra, though there is too much noise for their positions to be accurately resolved.

The observed transitions were plotted and fitted to a D and E only model (Fig. 3.14). The parameters $D = 11.45(2)$ K, $E = 0.49(1)$ K, $g_x = 2.240(7)$, $g_y = 2.228(5)$ and $g_z = 2.158(5)$ were extracted, and the model is in good agreement

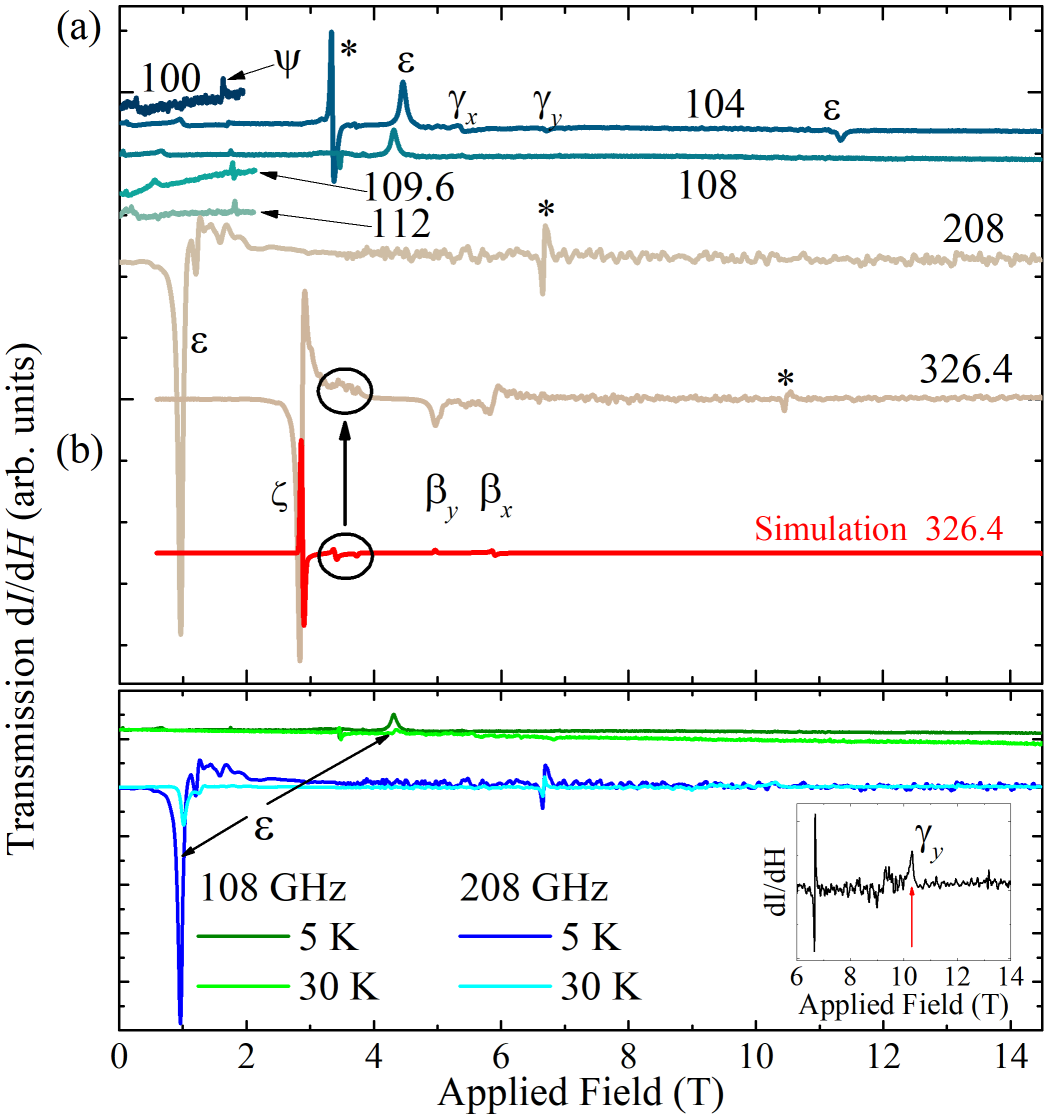

Figure 3.13: **(a)** ESR spectra of powdered $Ni(SiF_6)(H_2O)(4\text{-mepz})_4$ labelled in GHz for each spectra. Measurements were performed at ≈ 3 K (100, 104, 109.6, and 112 GHz) and 5 K (108, 208 and 326.4 GHz). Resonances of known transitions are labelled. The resonances marked with * are likely to be due to impurities. A 5 K simulation at 326.4 GHz with the parameters obtained from a D and E only fit to the observed resonances (Fig. 3.14) has been added in good agreement with the data. The circled resonances in the 326 GHz data and simulation correspond to the α_x and α_y transitions. **(b)** Temperature dependent ESR spectra at 108 and 208 GHZ. The decrease in the intensity of the low-field z-transition as the temperature is increased is clearly observed in both spectra, indicating that $D > 0$. Inset: 30 K ESR spectra at 208 GHz showing the γ_y transition at 10.3 T. This is not observed in the low temperature data and suggests that $D > 0$.

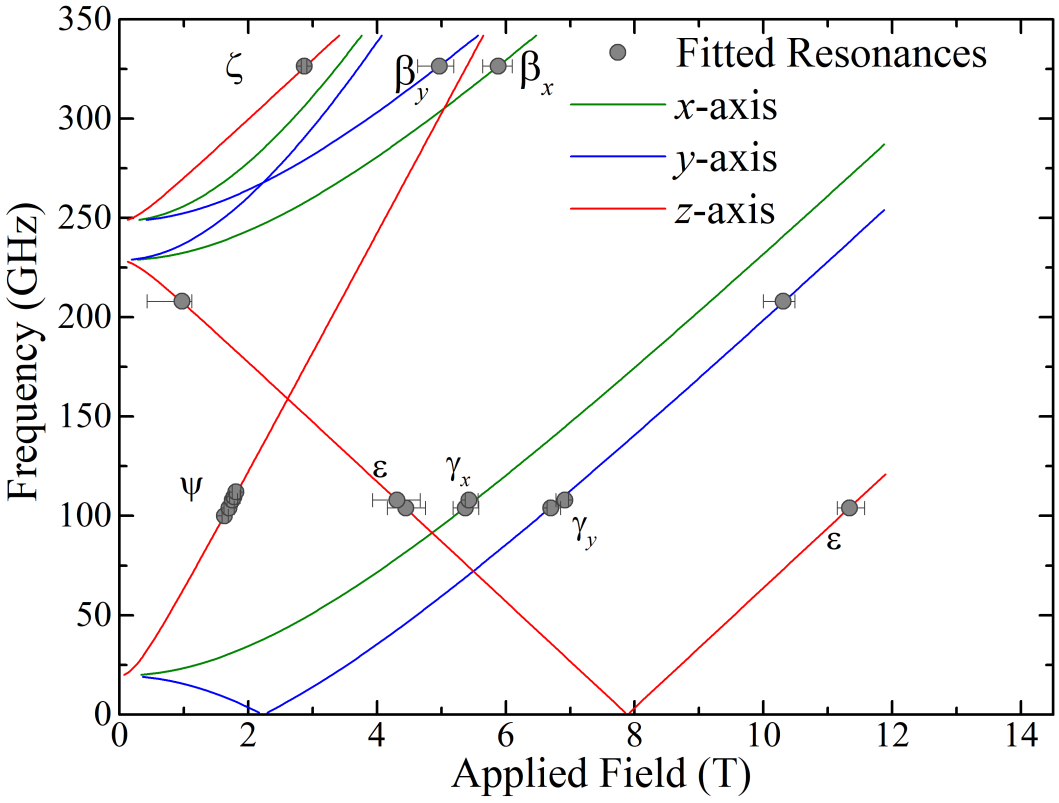

Figure 3.14: Fitting of the transitions from Fig. 3.13 to a D and E only model which yields the parameters $D = 11.45(2)$ K, $E = 0.49(1)$ K, $g_x = 2.240(7)$, $g_y = 2.228(5)$ and $g_z = 2.158(5)$.

with the data. A 326 GHz simulation using these parameters at 5 K is shown in Fig. 3.13 and recreates the β_x and β_y transitions. The simulated ζ resonance at 3 T is also in good agreement with the data, whilst the α_x and α_y resonances are shown to lie in the noisy region to the high-field side of ζ, confirming the analysis earlier. That $g_x > g_z$ is consistent with easy-plane anisotropy and a value of $\lambda = -279$ K is obtained for the spin-orbit coupling parameter [34]. This is of the same order of magnitude that is expected for Ni^{2+} ions. The parameters obtained from the ESR measurements confirm those obtained from the magnetometry measurements. Therefore, $Ni(SiF_6)(H_2O)(4\text{-mepz})_4$ can be described by Eq. 3.1 with $J = J_\perp = 0$, $D = 11.25(2)$ K and $E = 0.6(1)$ K.

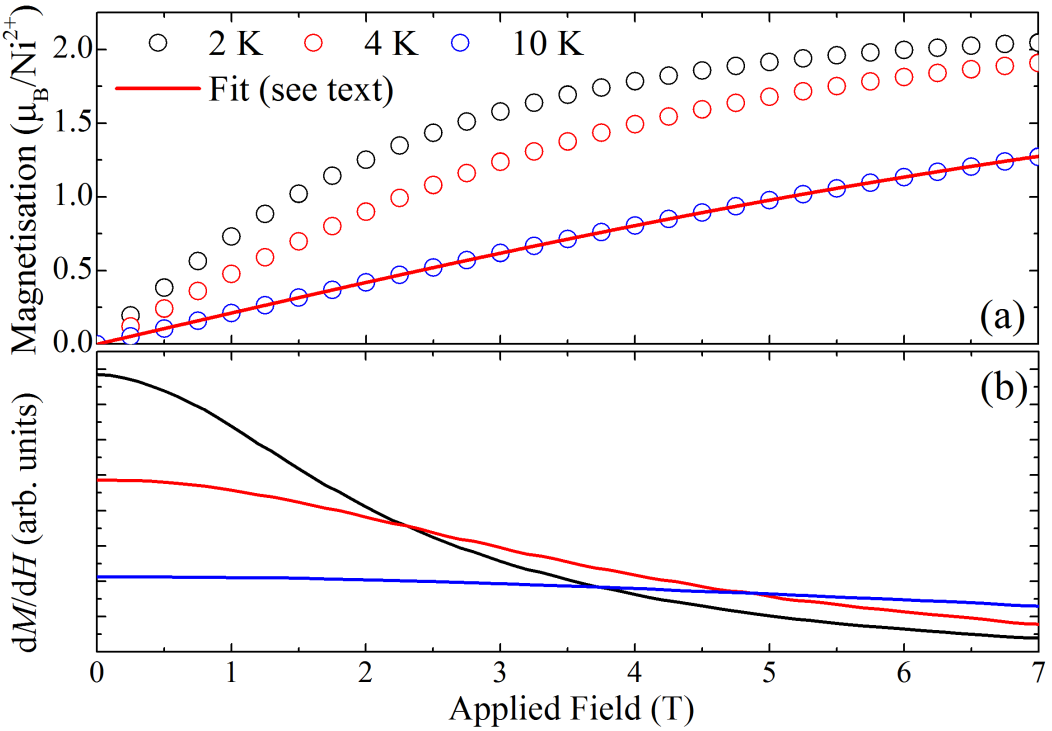

Figure 3.15: **(a)** SQUID magnetisation measurements of powdered $Ni(H_2O)_2(acetate)_2(4\text{-picoline})_2$ at different temperatures. The lowest temperature data saturates above $2\mu_B$. The 10 K data has been fitted with a Brillouin function, with $g = 2.178(1)$ extracted. **(b)** Differential susceptibility of $Ni(H_2O)_2(acetate)_2(4\text{-picoline})_2$ shows no evidence of critical fields due magnetic interactions or ground state energy-level crossings.

3.3.3 $Ni(H_2O)_2(acetate)_2(4\text{-picoline})_2$

Magnetometry

Quasi-static SQUID magnetisation measurements of powdered $Ni(H_2O)_2(acetate)_2(4\text{-picoline})_2$ rise to a broad saturation point [Fig. 3.15(a)]. The low temperature data saturates above $2\mu_B$, consistent with expected g-values for N^{2+} ions in octahedral environments [34]. The differential susceptibility of the 2 K data falls smoothly over the whole field range of the measurements. There is no evidence of magnetic interactions or ground state energy level crossings. It is possible that the temperature isn't low enough for a feature to be observed or that $Ni(H_2O)_2(acetate)_2(4\text{-picoline})_2$ is easy-axis.

DC susceptibility measurements of powdered $Ni(H_2O)_2(acetate)_2(4\text{-picoline})_2$ continually rise as the temperature is lowered to 1.8 K (Fig. 3.16). There is no

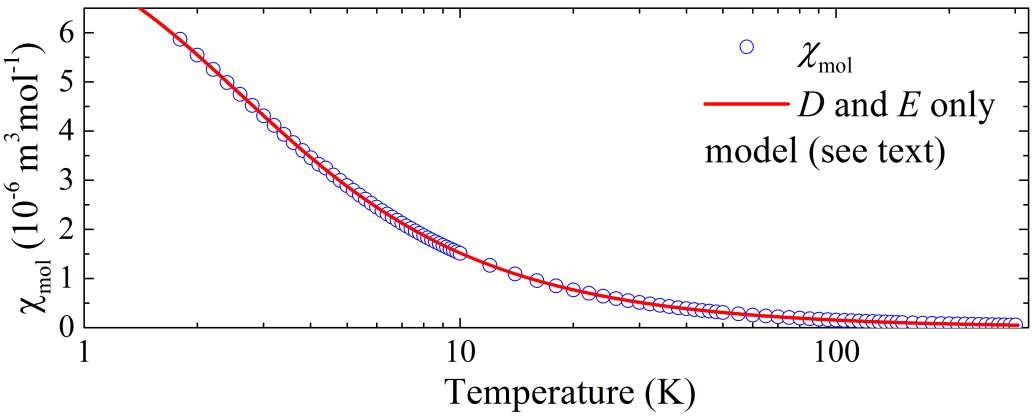

Figure 3.16: DC susceptibility measurement of $Ni(H_2O)_2(acetate)_2(4\text{-picoline})_2$ shows a rise in the data as the temperature is lowered. This was fitted to a D and E only model with a small diamagnetic component. The parameters $D = -5.78(8)$ K, $E = 1.38(2)$ K, $g = 2.22(1)$ and $\chi_0 = -2.4(1.0)$ m^3mol^{-1} extracted. The model is in good agreement with the data.

sign of a peak or a plateau in the data. The data was fitted to a D and E only model which includes a small temperature independent contribution χ_0. The parameters extracted are $D = -5.8(1)$ K, $E = 1.38(2)$ K, $g = 2.22(1)$ and $\chi_0 = -2.4(1.0)$ m^3mol^{-1}. These parameters model the data very well. If the D parameter is allowed to be positive, then the condition $|D| \geq 3E$ is not met. Therefore, magnetometry measurements suggest $Ni(H_2O)_2(acetate)_2(4\text{-picoline})_2$ contains easy-axis anisotropy with $D = -5.8(1)$ K and $E = 1.38(2)$ K.

Heat capacity

Zero-field heat capacity measurements of powdered $Ni(H_2O)_2(acetate)_2(4\text{-picoline})_2$ were performed by Jamie Brambleby at The University of Warwick. The powdered sample was pressed into a pellet for the measurement and the data is shown as $C_p/T(T)$ in [Fig. 3.17(a)]. The data shows a peak between 40 and 50 K due to lattice phonons. Below the peak, the data drops until $\approx$ 6 K where it starts to rise. As magnetisation measurement indicated negligible magnetic interactions in $Ni(H_2O)_2(acetate)_2(4\text{-picoline})_2$ the rise in the data is attributed to be the high-temperature side of a Schottky anomaly peak. Therefore, a model incorporating lattice phonons (Eq. 2.1) and single-ion anisotropy (Eq. 3.5) was used to fit the data. It was not possible to fit this model over the whole temperature range due to an over-parameterisation of the fit. Therefore, the data below 30 K was fitted to a model with one Debye mode, one Einstein mode and a single-ion anisotropy term.

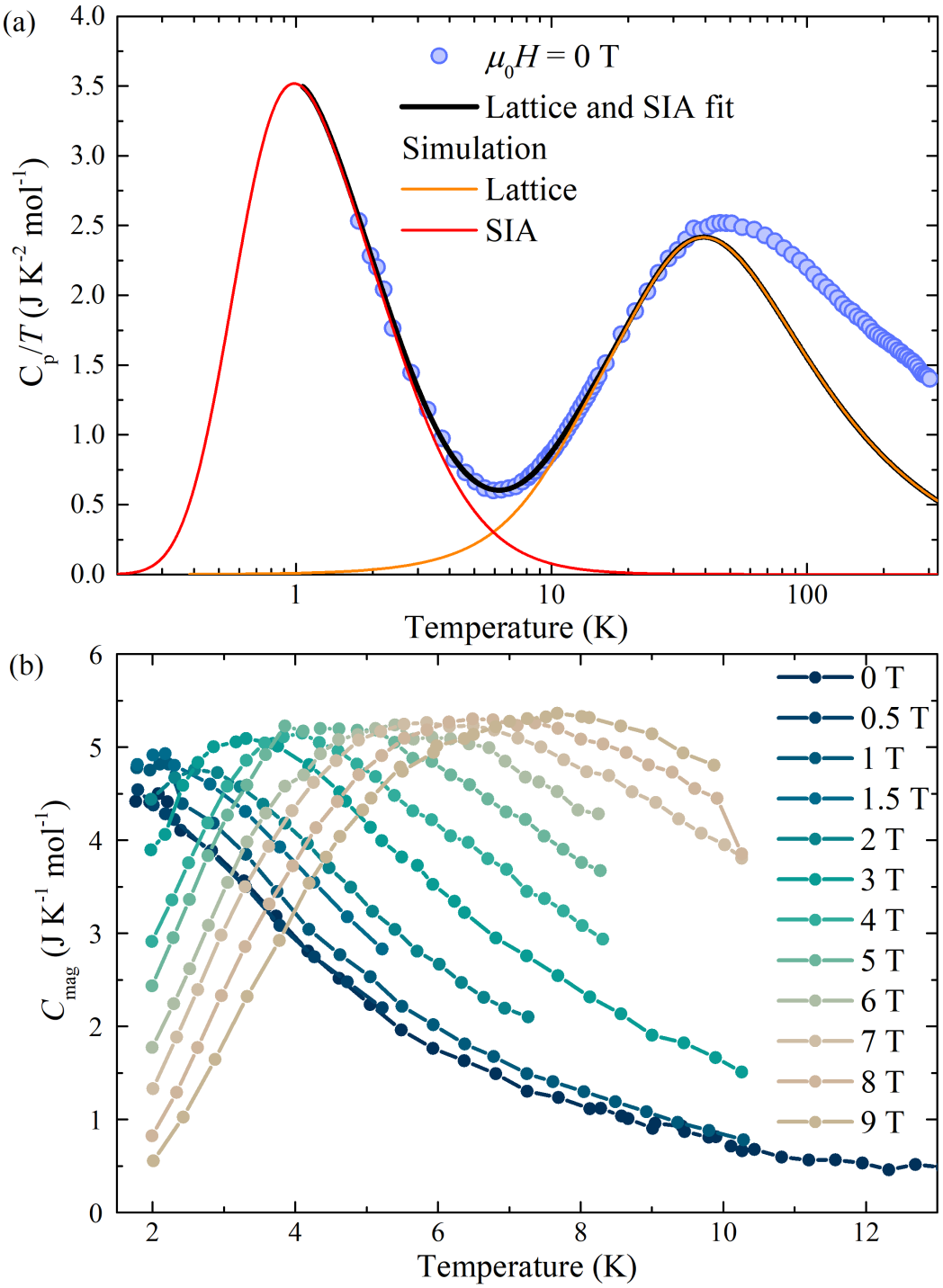

Figure 3.17: **(a)** Zero-field heat capacity measurement of $Ni(H_2O)_2(acetate)_2(4\text{-picoline})_2$. The data below 30 K is fitted to a model with one Debye, one Einstein mode and a single-ion anisotropy term. The parameters obtained are shown in Table. 3.5. **(b)** Magnetic heat capacity of $Ni(H_2O)_2(acetate)_2(4\text{-picoline})_2$ resulting from the subtraction of C_{latt}.

Table 3.5: Parameters obtained from the lattice and single-ion anisotropy fit to zero-field heat capacity measurements of $Ni(H_2O)_2(acetate)_2(4\text{-picoline})_2$ [Fig. 3.17(1)].

A_D	61(3) J/K mol
θ_D	82(2) K
A_{E1}	112(8) J/K mol
θ_{E1}	135(6) K
D	-6.6(1) K
E	1.51(1) K

The parameters extracted are shown in Table. 3.5. The model is in good agreement with the data over the fitted range. The values of $D = -6.6(1)$ K and $E = 1.51(1)$ K extracted. The value of D differs from that obtained in the susceptibility measurements by 12%, whereas the E parameters are in much better agreements. If D is allowed to be negative in the fit, then the values of D and E obtained do not meet the condition $|D| > 3E$. The parameters in Table. 3.4 were then used to subtract the lattice contribution from the total heat capacity to obtain the magnetic heat capacity measured at different magnetic fields of $Ni(H_2O)_2(acetate)_2(4\text{-picoline})_2$ [3.17(b)]. This shows the position of the Schottky anomaly increases in temperature as the field increase. There is an initial increase in amplitude between 0 and 1 T. As the field is increased further, the amplitude increases at a slower rate. Comparing with Fig. 2.5, this is further confirmation of easy-axis anisotropy in $Ni(H_2O)_2(acetate)_2(4\text{-picoline})_2$.

3.3.4 Discussion

The magnetic characteristics of powdered samples of the isolated $S = 1$ magnets $[Ni(3,5\text{-lut})_4(H_2O)_2](BF_4)_2$, $Ni(SiF_6)(H_2O)(4\text{-mepz})_4$ and $Ni(H_2O)_2(acetate)_2(4\text{-picoline})_2$ have been analysed. The magnetic parameters obtained from each technique for each system is shown in Table. 3.6. The parameters obtained from the different experimental techniques for each compound are consistent with each other. Magnetometry measurements are able to give a good initial characterisation of powdered $S = 1$ samples. Whilst the magnetisation technique doesn't always show a feature indicating the size and sign of D, it does show if $D \gg J$ or not. The sign and size of D can then be extracted from susceptibility measurements of powdered samples of isolated compounds with $E \neq 0$. As was found for all three compounds above, if the sign of D obtained from the fit is incorrect, then the condition $|D| \geq 3E$ is not met. Hence susceptibility measurements can be used to obtain the D and E parameters of systems that are known to be isolated. If $E = 0$, the behaviour of

Table 3.6: Magnetic parameters obtained from all measurements on [Ni(3,5-lut)$_4$(H$_2$O)$_2$](BF$_4$)$_2$, Ni(SiF$_6$)(H$_2$O)(4-mepz)$_4$ and Ni(H$_2$O)$_2$(acetate)$_2$(4-picoline)$_2$. The $M(H)$ value represents the $\sqrt{D^2 - E^2}$ value.

Compound		$\chi(T)$	$M(H)$	C_p	ESR
[Ni(3,5-lut)$_4$(H$_2$O)$_2$](BF$_4$)$_2$	D (K)	8.69(3)	9.0(9)	10.4(1)	10.4(1)
	E (K)	1.25(12)		2.6(2)	2.12(4)
Ni(SiF$_6$)(H$_2$O)(4-mepz)$_4$	D (K)	11.25(2)	11.8(7)	-	11.45(2)
	E (K)	0.6(1)			0.49(1)
Ni(H$_2$O)$_2$(acetate)$_2$(4-picoline)$_2$	D (K)	-5.8(1)	-	-6.6(1)	-
	E (K)	1.38(2)		1.51(1)	

the susceptibility at very low temperatures is distinct for easy-plane and easy-axis anisotropy and can be used to determine the sign of D. For easy-plane anisotropy, χ_{xy} plateaus and $\chi_z \to 0$ as $T \to 0$ [32]. In the presence of easy-axis anisotropy, the χ_{xy} component still plateaus but $\chi_z \to \infty$ as the temperature approaches zero.

Likewise, heat capacity measurements of isolated systems can also accurately determine the sign and size of D if there is a significant E term. When fitting the heat capacity data of [Ni(3,5-lut)$_4$(H$_2$O)$_2$](BF$_4$)$_2$ and Ni(H$_2$O)$_2$(acetate)$_2$(4-picoline)$_2$ it was found that the condition $|D| \geq 3E$ is not met if the sign of D was allowed to be incorrect. The sign and size of D is simple to extract if there is no E term. This is due to the difference in the zero-field entropy of the Schottky anomaly between easy-axis and easy-plane systems when $E = 0$. The amplitude of the Schottky anomaly behaves differently between the two cases as the field is raised, giving a straightforward identification of the zero-field ground state. The magnitude of D can then be obtained using Eq. 3.5 with E set to zero. The method of determining D from the field dependence of the Schottky anomaly that was outlined in section 2.2 was not used due to the non-zero E term in the Hamiltonians of [Ni(3,5-lut)$_4$(H$_2$O)$_2$](BF$_4$)$_2$ and Ni(H$_2$O)$_2$(acetate)$_2$(4-picoline)$_2$.

ESR measurements are highly suited to determining SIA parameters, and have confirmed the parameters obtained from magnetometry and heat capacity measurements. However, powder-averaging increases the number of peaks in each field sweep compared to measurements of single crystals. There can be up to 9 different resonances that can occur in any ESR spectra. It may require numerous ESR spectra at slightly different frequencies to determine which transition each resonance belongs to. Even then, it may require fits to known resonances to indicate what transitions a particular feature can correspond to. Resonances may also overlap. For example, three transitions occur between 7 and 8 T in the 412.8 GHz sweep of [Ni(3,5-lut)$_4$(H$_2$O)$_2$](BF$_4$)$_2$ (Fig. 3.10). Whilst this may explain the broadness

of the resonance observed in Fig. 3.10, it can make it difficult, if not impossible, to determine an accurate field at which these transitions occur. This significantly increases the time required to make and analyse ESR measurements of powdered $S = 1$ samples.

3.4 Interacting Ni^{2+} ions

3.4.1 $[Ni(pyz)_2(H_2O)_2](BF_4)_2$

Magnetometry

Susceptibility measurements of powdered $[Ni(pyz)_2(H_2O)_2](BF_4)_2$ were made by Jamie Brambleby at The University of Warwick. The data shows a rise in $\chi(T)$ as the temperature is lowered towards a broad peak at $T = 3.6(2)$ K [Fig. 3.18(a)]. This feature indicates the build up of short range correlations between Ni^{2+} ions within the Ni-pyz planes. Below the peak, the data drops before appearing to flatten out. By differentiating the χT data, a peak can be clearly seen at $T = 3.0(2)$ K [Inset to Fig. 3.18(a)], which is attributed to long-range ordering in $[Ni(pyz)_2(H_2O)_2](BF_4)_2$ via the Fisher Relation [43]. A fit to the $\chi(T)$ data was not attempted due to a lack of suitable anisotropic $S = 1$ Q2D models. The high temperature inverse susceptibility is fitted to a Curie-Weiss model with a temperature independent contribution χ_0 [Fig. 3.18(b)]. The extracted parameters are $g = 2.19(1)$, $\chi_0 = +1.3(1)$ m^{-3}mol and $\theta_W = -3.4(3)$ K. The negative Weiss temperature indicates antiferromagnetic interactions between adjacent Ni^{2+} ions in the xy planes.

The magnetisation curve of $[Ni(pyz)_2(H_2O)_2](BF_4)_2$ recorded at 0.58 K rises, with a slight concave shape at low temperatures, towards a broad saturation. This is indicative of low-dimensional magnetism in this compound [123]. The differential susceptibility [Fig. 3.19(b)] exhibits two critical fields, with no indication of a spin-flop, suggesting that $D > 0$. The first critical field is taken to be the peak at $H_{C1} = 5.7(3)$ K [Inset to Fig. 3.19(b)]. The upper critical field is more difficult to determine. In Ref. [13], it is taken at the point where $dM/dH = 0$. However, in the present data, this value is never reached. Therefore, it is taken to be when d^2M/dH^2 first approaches zero [Inset to Fig. 3.19(b)]. This occurs at $H_{SAT} = 15.7(5)$ K. Using Eq. 2.3 and Eq. 2.4, with the g-factor taken from the Curie-Weiss model, values of $J = 1.05(5)$ K, $D = 7.3(7)$ K and $E = 0$ are extracted.

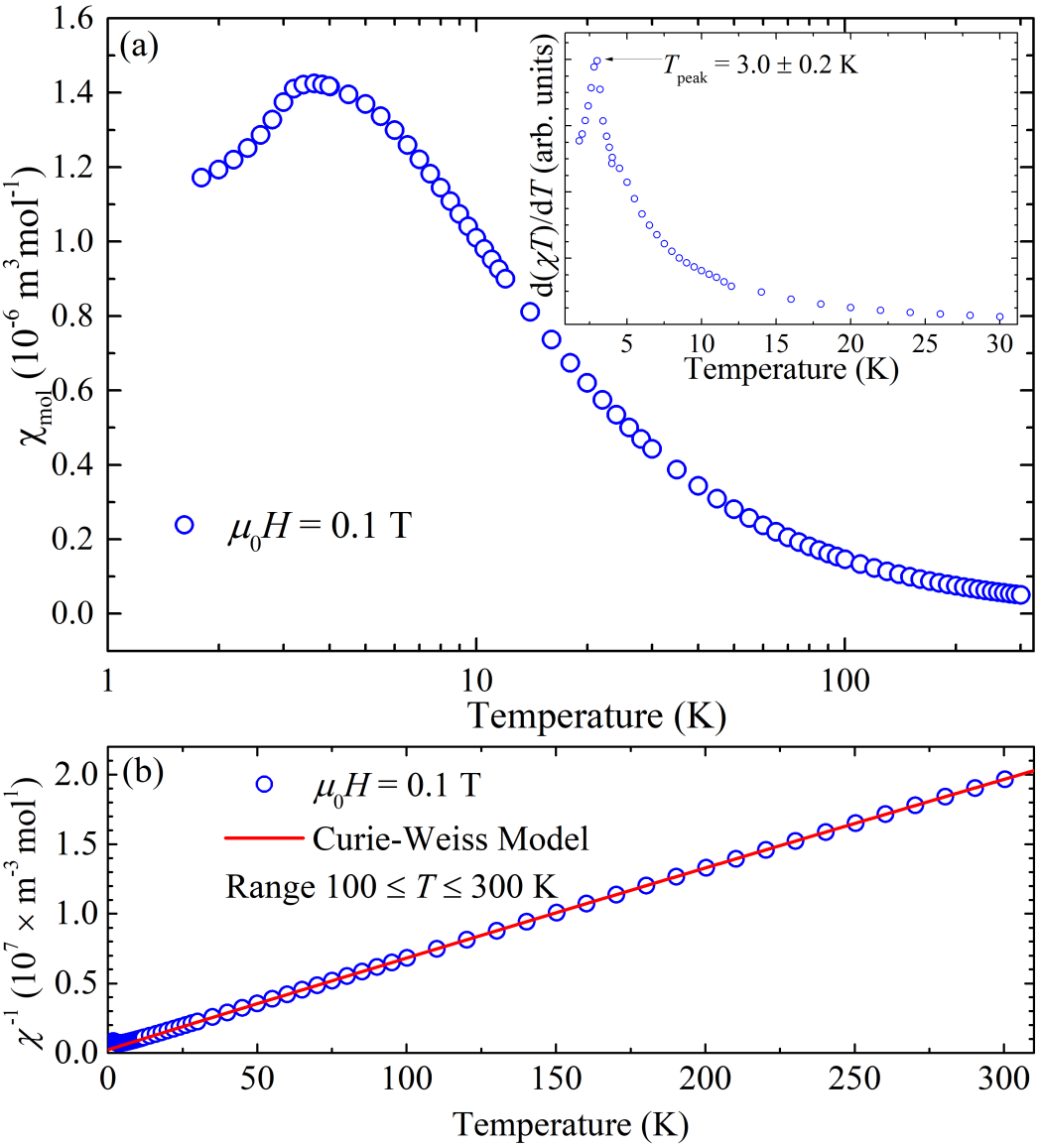

Figure 3.18: **(a)** DC susceptibility measurements and [inset]: d(χT) /dT of powdered $[Ni(pyz)_2(H_2O)_2](BF_4)_2$. **(b)** Inverse susceptibility fitted to a Curie-Weiss model over the range $100 \leq T \leq 300$ K with parameters $g = 2.19(1)$, $\theta_w = -3.4(3)$ K and $\chi_0 = +1.3(1)$ m^{-3}mol extracted.

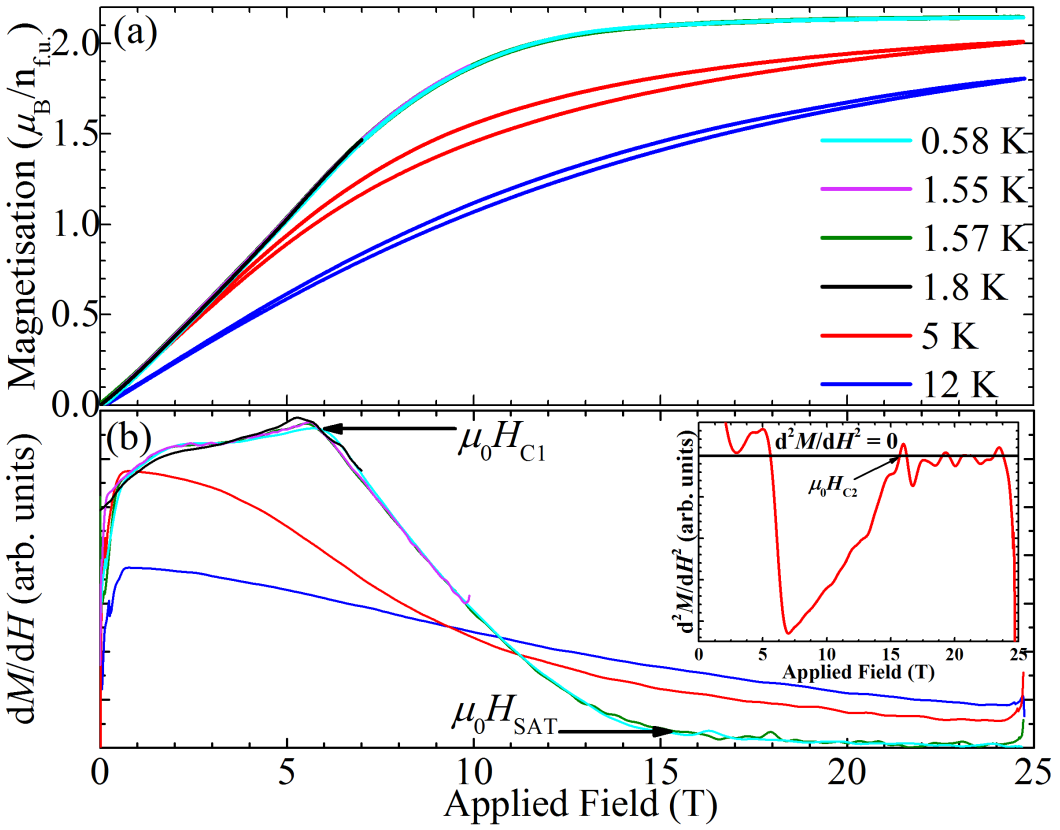

Figure 3.19: **(a)** Pulsed-field magnetisation vs. applied field for powdered $[Ni(pyz)_2(H_2O)_2](BF_4)_2$. **(b)** Differential susceptibility shows two critical fields (measured from the lowest temperature pulsed-field up sweep). Inset: gradient of the differential susceptibility is used to determine H_{SAT} (see text).

Heat capacity

The heat capacity of powdered $[Ni(pyz)_2(H_2O)_2](BF_4)_2$ (plotted as C_p/T vs. T) is shown in Fig. 3.20(a). The data exhibits a sharp lambda peak at 3.0(2) K, which is indicative of a transition to a magnetically ordered state. This is in excellent agreement with the value of T_N obtained from susceptibility measurements. However, the magnetisation data indicates that J is of the same order of magnitude as D. Currently, there is no model to describe the zero-field heat capacity of a system of magnetically interacting moments. Therefore the method of fitting the whole heat capacity used in section 3.3.1 and section 3.3.3 cannot be repeated. The data was fitted to the lattice heat capacity model in Eq. 2.1 with one Debye mode and three Einstein modes of the range $24 \leq T \leq 300$ K. Integration of the resultant C_{mag} yields an entropy change at low temperature consistent with that expected for an

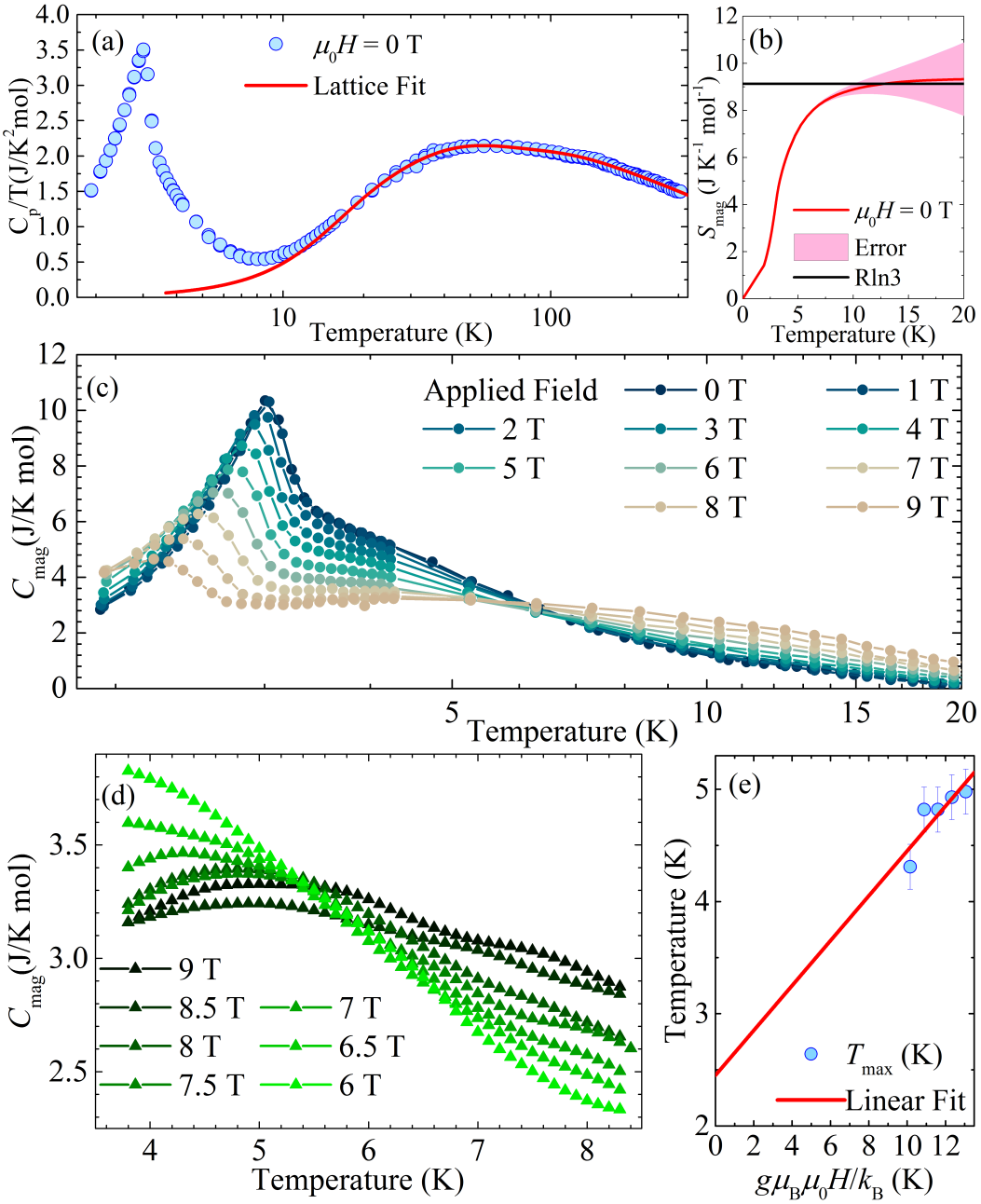

Figure 3.20: **(a)** Ratio of heat capacity to temperature vs. temperature for $[Ni(pyz)_2(H_2O)_2](BF_4)_2$ in zero-field. The solid line is a fit to the data from $24 \leq T \leq 304$ K to a model of one Debye and three Einstein modes. **(b)** Entropy vs. temperature in zero-field. **(c)** Magnetic heat capacity vs. temperature for $[Ni(pyz)_2(H_2O)_2](BF_4)_2$, resulting from the subtraction of C_{latt}, in applied fields in the range $0 \leq \mu_0 H \leq 9$ T.**(d)** Magnetic heat capacity vs. temperature around the Schottky anomaly. **(e)** Measured temperature of the broad maximum vs. applied field scaled by the g-factor.

Table 3.7: C_{latt} parameters for $[Ni(pyz)_2(H_2O)_2](BF_4)_2$ obtained from modelling high-temperature heat capacity data in Fig. 3.20(a).

Parameter	Fitted Value (K)
A_{D}	98(13)
θ_{D}	116(9)
A_{D1}	109(6)
θ_{D1}	208(21)
A_{D2}	234(10)
θ_{D2}	509(20)
A_{D3}	247(27)
θ_{D3}	1287(128)

easy-plane $S = 1$ system. The resultant lattice parameters are shown in Table. 3.7. With these parameters, the model is in good agreement with the data over the fitted range.

The magnetic heat capacity [Fig. 3.20(c)] recreates the lambda peak caused by the transition to long-ranged order. As the applied field is increased, the peak is suppressed in height and moves to lower temperatures. This is is consistent with a primary antiferromagnetic exchange interaction in $[Ni(pyz)_2(H_2O)_2](BF_4)_2$. For applied fields in excess of 6 T, a small broad maximum emerges with a peak at approximately 5 K. This moves to higher temperatures as the applied field is raised [Fig. 3.20(d)], strongly resembling the behaviour of a Schottky anomaly. The measured values of this maximum T_{max} vs. applied field are shown in Fig. 3.20(e). The data linearly extrapolates to a positive temperature-axis intercept of 2.5(8) K, and has a gradient $\delta = 0.20(7)$. Using Eq. 2.8, the value of D for $[Ni(pyz)_2(H_2O)_2](BF_4)_2$ is either: (i) an easy-plane anisotropy of $D = +7.1(3.5)$ K; or (ii) an easy-axis anisotropy with $D =$ -8.2(3.5) K. The easy-plane case is in good agreement with the value of D obtained in the magnetisation measurement and therefore $[Ni(pyz)_2(H_2O)_2](BF_4)_2$ is easy-plane with $D = +7.3(7)$ K. It is possible that the magnetic heat capacity can give a negative D parameter, and this will be discussed further in section 3.4.2.

Muon spin relaxation

μ-SR measurement were performed and analysed by F. Xiao, T. Lancaster, R. Williams and Stephen Blundell. Spectra at 2.18 and 3.50 K are plotted in Fig 3.21(a). At temperatures below 3.2 K the asymmetry shows heavily damped oscillations at two distinct frequencies. The amplitudes of the oscillations decreases with increasing temperature. For $T > 3.2$ K, oscillations are seen at a lower frequency, but show little variation as the temperature is further increased. The oscillations measured for

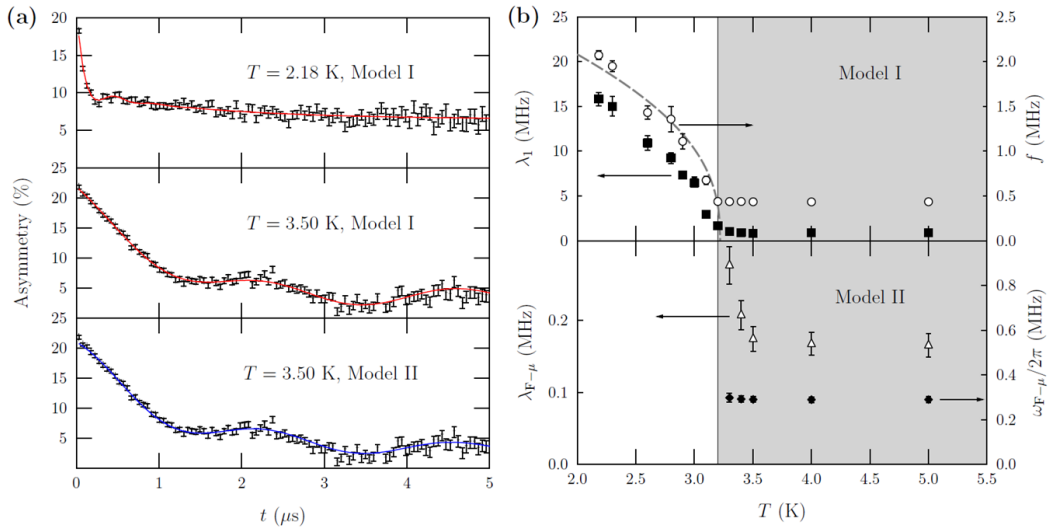

Figure 3.21: **(a)** Example spectra for $[Ni(pyz)_2(H_2O)_2](BF_4)_2$ at selected temperatures. Red lines are a fit using Eq. 3.6 and the blue line is a fit to Eq. 3.7. **(b)** Temperature dependence of the fitted parameters using Eq. 3.6 (top) and Eq. 3.7 (see text). The border of the white/gray area is at $T = 3.2$ K and the dashed line is a guide to the eye.

$T < 3.2$ K are characteristic of a quasi-static local magnetic field at the muon stopping site, indicating the presence of long-range order in $[Ni(pyz)_2(H_2O)_2](BF_4)_2$. The asymmetry $A(t)$ was initially fitted to a model with three components (two oscillatory and one non-oscillatory) across all temperatures:

$$A(t) = A_{\text{rel}}[p_1 e^{-\lambda_1 t}\cos(2\pi\nu_1 t) + p_2 e^{-\lambda_2 t}\cos(2\pi\nu_2 t) + (1 - p_1 - p_2)\, e^{-\lambda_3 t}] + A_{\text{bg}}, \tag{3.6}$$

where A_{rel} corresponds to the total relaxing amplitude, p_1 and p_2 are the weights of the oscillatory components that have frequencies ν_1 and ν_2, and λ_1 and λ_2 are the respective relaxation rates. The constant term A_{bg} accounts for the non-relaxing contribution from those muons that stop at the sample holder/cryostat tail. Fitted values of λ_1 and f are plotted against temperature in the top panel of Fig 3.21(b). A sharp change is observed in both λ_1 and f at around $T = 3.2$ K, strongly indicative of a magnetic phase transition. The frequencies fall as the temperature nears the transition at T_{N} [124]. However, oscillations in $A(t)$ persists up to $T = 20$ K. This oscillation is due to a muon-fluorine entangled state [125] and is described using:

$$A(t) = A_{\text{rel}}\left[p_1 e^{-\lambda_{\text{F}-\mu} t} D_z(\omega_{\text{F}-\mu}, t) + p_2 e^{-\Lambda t}\right] + A_{\text{bg}}. \tag{3.7}$$

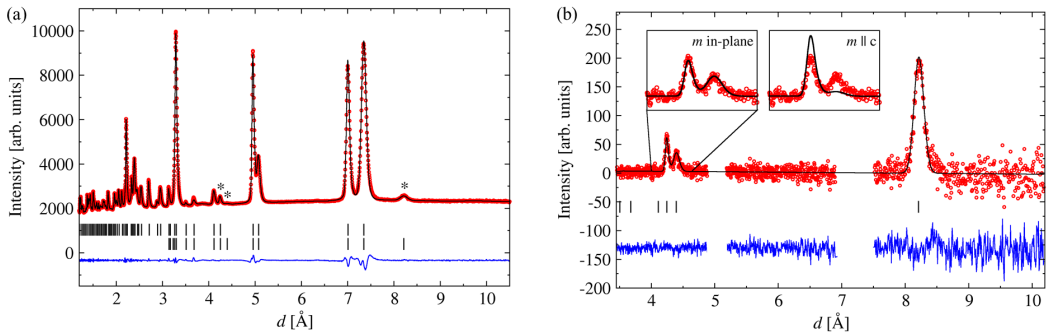

Figure 3.22: **(a)** Scattered neutron intensity at 1.5 K as a function of d-spacing for $[Ni(pyz)_2(H_2O)_2](BF_4)_2$. The three magnetic peaks are marked with * and correspond to (from left to right) the [101], [103] and [211] families of reciprocal lattice vectors. **(b)** The 10 K data has been subtracted leaving the magnetic contribution to the 1.5 K measurement. The relative diffraction intensities are consistent with easy-plane anisotropy. Note that the artefacts that arise in the subtraction of the brightest nuclear reflections in the presence of a slight lattice contraction have been masked.

The function describing the muon-fluorine dipolar interaction $D_z(\omega_{F-\mu}, t)$ [125], models the interaction of the muon with a single $I = 1/2$ fluorine nucleus. $[Ni(pyz)_2(H_2O)_2](BF_4)_2$ undergoes a transition to a state of long range magnetic order at $T_N = 3.2(1)$ K, which is within the errors of susceptibility and heat capacity measurements.

Elastic neutron scattering

Elastic neutron scattering measurements of the deuterated, powdered $[Ni(D_2O)_2(pyz\text{-}d_4)_2]({}^{11}BF_4)_2$ were made on the WISH diffractometer at ISIS, Rutherford Appleton Laboratory, UK. The data was analysed by Roger Johnson from the Clarendon Laboratory, Oxford University. Due to the dynamics of the water molecules in $[Ni(pyz)_2(H_2O)_2](BF_4)_2$ a full quantitative refinement is difficult to obtain. A LeBail [120] fit to Bragg peaks observed in the 1.5 K measurement is in good agreement with the reflection conditions of the space group $I4/mcm$ [Fig. 3.22(a)]. The lattice parameters extracted are $a = b = 9.8859(2)$ Å and $c = 14.6625(4)$ Å, consistent with the room temperature x-ray parameters (Table. 3.2). Reflections with a large projection onto the $\mathbf{c}*$ reciprocal lattice vector was found to be broader than the others and required an inclusion of a strain model when fitting. This represents a degree of decoherence along the c-axis.

The sign of D in $[Ni(D_2O)_2(pyz\text{-}d_4)_2]({}^{11}BF_4)_2$ was determined by fitting the relative intensities of the magnetic diffraction peaks [Fig. 3.22(b)]. As the magnetic

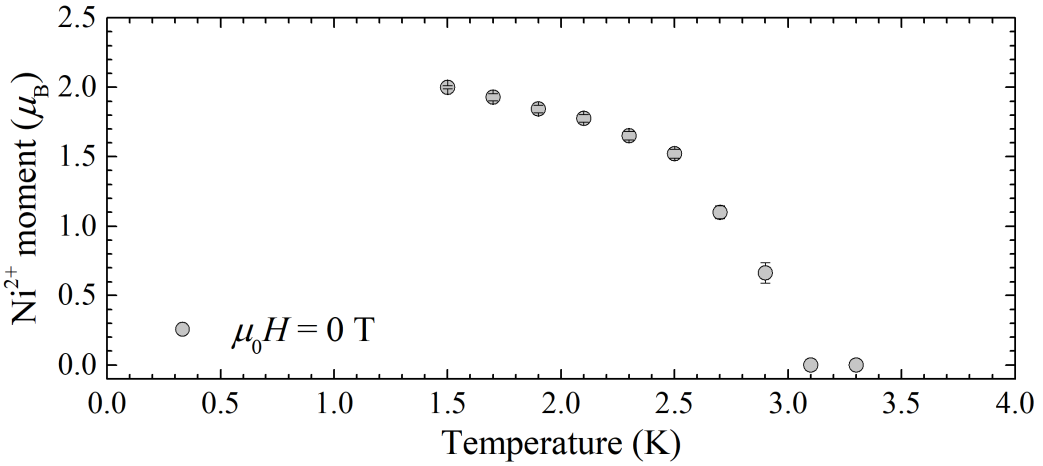

Figure 3.23: Temperature dependence of the ordered moment in $[Ni(D_2O)_2(pyz\text{-}d_4)_2](^{11}BF_4)_2$.

intensity couldn't be quantitatively scaled, the magnitude of the magnetic moments were set to the theoretical, spin only value of $2\mu_B$. The scale of the magnetic phase was then left to refine. The diffraction intensities in Fig. 3.22(b) are consistent with magnetic moments pointing perpendicular to the z-axis. This is indicative of easy-plane anisotropy. This is in excellent agreement with the sign of D obtained from magnetometry measurements. The temperature dependence of the integrated intensity of the [101] magnetic diffraction peak, which is proportional to the ordered moment, is shown in Fig. 3.23. The data is very consistent with a transition to long-range order at 3.0(2) K.

3.4.2 Discussion

$[Ni(pyz)_2(H_2O)_2](BF_4)_2$ has been analysed using fields that can be reached using commercially available magnetometry and heat capacity measurement systems. Magnetisation measurements have shown $[Ni(pyz)_2(H_2O)_2](BF_4)_2$ to be quasi two-dimensional antiferromagnet with $J = 1.05(5)$ K. It exhibits easy-plane anisotropy with $D = +7.3(7)$ K and $E = 0$, consistent with the heat capacity data. The sign of D is in excellent agreement with neutron scattering measurements. Susceptibility and heat capacity measurements also show a transition to long-range order at $T_N = 3.0(2)$ K. This has been confirmed using μ-SR and neutron scattering measurements. The resultant phase diagram of $[Ni(pyz)_2(H_2O)_2](BF_4)_2$ is shown in Fig. 3.24. On cooling from high-temperatures in zero-field, the material develops easy-axis anisotropy within the paramagnetic phase due to D, before the onset to antiferromagnetic ordering at 3.0 $\pm$ 0.2 K. In an applied field, the powdered sam-

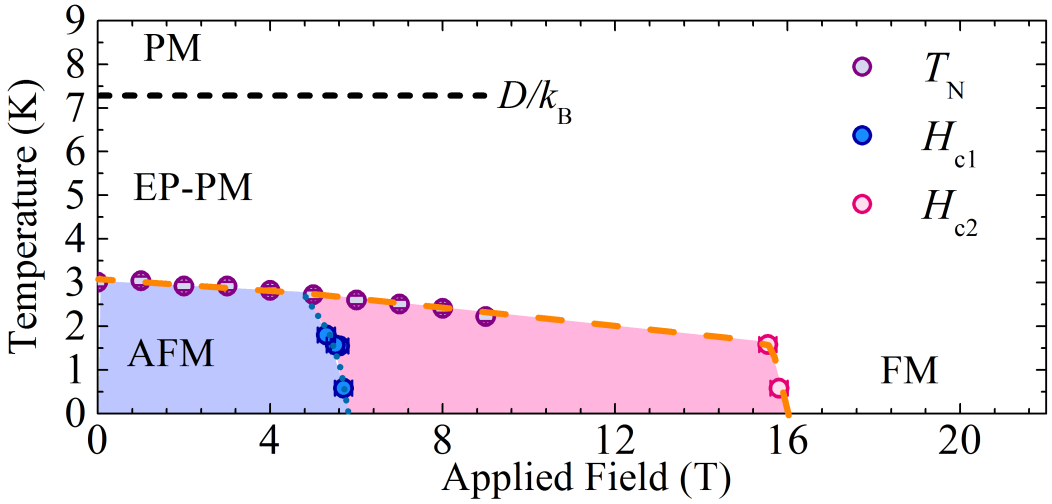

Figure 3.24: Phase Diagram of $[Ni(pyz)_2(H_2O)_2](BF_4)_2$. As the temperature is lowered below 7.3(7) K the sample moves from a pure paramagnetic (PM) into an easy-plane anisotropy dominated paramagnetic phase (PM-EP). As the temperature drops further, the sample undergoes a transition to long-range order below 3.0(2) K (AFM). On increasing the field, moments saturate for fields perpendicular to and then parallel to the z-axis. The moments are fully saturated at $\approx$ 16 T (FM). Lines are a guide to the eye.

ple passes through two critical fields corresponding to the saturation field for fields within and perpendicular to the easy-plane.

The errors obtained in calculating the D-parameter from the behaviour of the Schottky anomaly in heat capacity measurements are very large. This is due to three things. Firstly, the Schottky anomaly is naturally a broad feature [24]. Further broadening is caused by the powdered nature of the sample. Lastly, in the case of $[Ni(pyz)_2(H_2O)_2](BF_4)_2$, the important low-field behaviour of the Schottky anomaly is obscured by long-range ordering. Extrapolation of the observed peaks with large errors towards zero causes a propagation of these errors through Eq. 2.8. This leads to a very high error in the calculated value of D, making heat capacity measurement unsuited to modelling the single-ion anisotropy of interacting $S = 1$ moments. On the other hand, magnetisation measurements have been successful at separating the effect of J and D.

3.5 Summary

I have found that readily available magnetisation and heat capacity techniques are sensitive to the energy scale of the SIA of Ni^{2+} $S = 1$ systems, though in powdered

AFM systems it has been shown that their features can be masked by magnetic interactions. However, by comparison with simulations, the effects of SIA and magnetic interactions can be separated. Using these methods, I have been able to characterise three compounds made up of isolated Ni^{2+} complexes; $[Ni(3,5\text{-lut})_4(H_2O)_2](BF_4)_2$, $Ni(SiF_6)(H_2O)(4\text{-mepz})_4$ and $Ni(H_2O)_2(acetate)_2(4\text{-picoline})_2$. Magnetometry and heat capacity measurements have been very successful in obtaining the sign of D. A check with ESR measurements have shown that the magnitude of the single-ion anisotropy parameters obtained from lab-based methods are reasonably accurate. Whilst there have been a few differences in the size of D and E between some measurements, they are small. A confident decision about whether further single-crystal or more specialist characterisation techniques are required can therefore be made.

The quasi-two dimensional $[Ni(pyz)_2(H_2O)_2](BF_4)_2$ has also been successfully characterised using magnetisation measurements. It can modelled be using Eq. 3.1, with $J = 1.05(5)$ K, $D = +7.3(7)$ K and $E = 0$ K. The SIA parameters are consistent with heat-capacity measurements of $[Ni(pyz)_2(H_2O)_2](BF_4)_2$ and similar to those found for $[Ni(3,5\text{-lut})_4(H_2O)_2](BF_4)_2$. The J parameter is comparable to other compounds with $[Ni(pyz)_2]^{2+}$ square planes [1, 13]. Susceptibility and heat capacity measurements show that $[Ni(pyz)_2(H_2O)_2](BF_4)_2$ orders antiferromagnetically at $T_N = 3.0(2)$ K, in good agreement with muon spin relaxation and elastic neutron scattering measurements. The sign of D has also been confirmed by neutron scattering measurements.

The main issue with characterising systems of interacting $S \geq 1$ ions is the aforementioned competition between single-ion anisotropy and magnetic interactions. Whilst magnetisation measurements are successful at decomposing the effects of single-ion anisotropy and magnetic interactions, heat capacity measurements are not. However, heat capacity measurements are still highly suited to mapping out the field dependent behaviour of T_N. If the ordering temperature is significantly far away from the Schottky anomaly, then theoretically the magnitude of D could be obtained from heat capacity measurements. Further measurements on suitable systems are required to confirm this however.

The structural dependence of the single-ion anisotropy for the compounds in this chapter will now be discussed. Table. 3.2 and Table. 3.3 show that $[Ni(pyz)_2(H_2O)_2](BF_4)_2$ and $[Ni(3,5\text{-lut})_4(H_2O)_2](BF_4)_2$ contain slightly axially compressed octahedra whereas $Ni(H_2O)_2(acetate)_2(4\text{-picoline})_2$ and $Ni(SiF_6)(H_2O)(4\text{-mepz})_4$ contain axially elongated octahedra. According to previous predictions, this suggests that $[Ni(3,5\text{-lut})_4(H_2O)_2](BF_4)_2$ and $[Ni(pyz)_2(H_2O)_2](BF_4)_2$ should be easy-axis and $Ni(H_2O)_2(acetate)_2(4\text{-picoline})_2$ and $Ni(SiF_6)(H_2O)(4\text{-mepz})_4$ should

be easy-plane [34, 35]. This is not the case. The electronic properties of the coordinated atoms that make up the Ni^{2+} octahedra also have a contribution to the zero-field splitting. The easy-axis $Ni(H_2O)_2(acetate)_2(4\text{-picoline})_2$ contain NiN_2O_4 octahedra whereas the other, easy-plane, compounds have NiN_4O_2 or NiN_4OF environments. The magnetic moments seem to align in the direction of the nitrogen atoms. Nitrogen atoms are less electronegative than oxygen and fluorine atoms [126], suggesting moments prefer to point away from the most electronegative ligand. This will be discussed in detail in the next chapter.

Chapter 4

Towards the control of the magnetic properties of Ni^{2+} chains.

4.1 Introduction

The aim of this chapter is to characterise NiF_2(3,5-lut)$_4$·H_2O and the NiX_2(3,5-lut)$_4$ (lut = lutidine, C_7H_9N. X = Cl, Br, I and HF_2) family to determine to what extent the control of the magnetic properties of Ni^{2+} chains can be achieved. This will make use of different bridging halide ions which causes structural changes between the different members of NiX_2(3,5-lut)$_4$ and NiF_2(3,5-lut)$_4$·H_2O. By linking this change in structure and composition to any change in the magnetic properties, a greater understanding of how to create bespoke magnetic systems can be achieved. Copper- and nickel-halide pathways have already been shown to be able to mediate magnetic exchange with varying magnitudes of J [1, 117, 127, 128]. These previous efforts indicated changing magnetic behaviour linked to the halide ions. J. Schlueter *et al.*, studied the CuX_2(pyzO)$(H_2O)_2$ (X = Cl,Br. pyzO = pyrazine-N,N'-dioxide, $C_4H_4N_2O_2$) family made up of Cu-X-X-Cu chains bridged by pyzO molecules [127].

Table 4.1: Experimentally obtained magnetic parameters and unit cell lengths for the NiX_2(pyz)$_2$ family. This table is adapted from Table. 3 in [1]

X	J_{pyz} (K)	J_X (K)	D K	Ni-pyz-Ni (Å)	NiX-X-Ni (Å)
Cl	0.49(1)	<0.05	8.03(16)	7.0425(2)	10.7407(3)
Br	1.00(5)	0.26(5)	0	7.0598(2)	11.3117(3)
I	<1.19	>1.19	0	7.057502(18)	12.25594(5)

Table 4.2: Table showing which experimental techniques were used to study each compound in this chapter. Red ticks correspond to measurements performed and analysed by myself. Blue ticks represent measurements analysed but not performed by myself. Pulsed-field measurements were performed by Jamie Manson, John Singleton and Serena Birnbaum at the National High Magnetic Field Laboratory (NHMFL), Los Alamos, USA. ESR measurements were performed by Jamie Manson and Andrew Ozarowski at NHMFL, Tallahassee, USA.

Compound	$\chi(T)$	$M(H)$	$C_p(T)$	ESR
$NiF_2(3,5\text{-lut})_4{\cdot}H_2O$		✓		
$Ni(HF_2)_2(3,5\text{-lut})_4$				✓
$NiCl_2(3,5\text{-lut})_4$	✓	✓		
$NiBr_2(3,5\text{-lut})_4$	✓	✓		✓
$NiI_2(3,5\text{-lut})_4$	✓	✓	✓	✓

Whilst the structures of the two compounds remained reasonably similar, it was found that $J_{\mathrm{Br}} = 4J_{\mathrm{Cl}}$. The bigger bromide ion clearly mediates the superexchange interaction better than the chloride ion. J. Liu *et al.* showed that by increasing the size of the halide ion increases the strength of magnetic interactions through Ni-X-X-Ni pathways in Q2D systems. However, the distance between the Ni^{2+} ions also increased from $X = \mathrm{Cl} \rightarrow \mathrm{I}$ (Table. 4.1) which would also contribute to this change in J. It also appeared that the single-ion anisotropy decreased as the size of the halide ion increased and moved further away from the Ni^{2+} ion. However, this change could not be studied in depth due to the stronger magnetic interactions within Ni-pyz planes masking the effect of D. Therefore, $NiF_2(3,5\text{-lut})_4{\cdot}H_2O$ and $NiX_2(3,5\text{-lut})_4$ were synthesised to investigate the effect of halide substitution on the magnetism of spin-1 chains. Pyrazine is a well known mediator of magnetic exchange [1]. As observed in the previous chapter, lutidine molecules create a very inefficient pathway for magnetic exchange. Therefore replacing pyrazine with non-bridging lutidine molecules creates quasi one-dimensional magnetic structures along Ni-halide-halide-Ni chains in $NiF_2(3,5\text{-lut})_4{\cdot}H_2O$ and $NiX_2(3,5\text{-lut})_4$. Magnetometry, heat capacity and ESR measurements were made on $NiF_2(3,5\text{-lut})_4{\cdot}H_2O$ and $NiX_2(3,5\text{-lut})_4$ to determine the magnetic properties of these compounds. Table. 4.2 shows which measurements were made on the compounds in this chapter.

4.2 Structure

Single crystal x-ray diffraction measurements of $NiF_2(3,5\text{-lut})_4{\cdot}H_2O$ were made by Robert Williams and Sam Curley at The University of Warwick. Crystals with

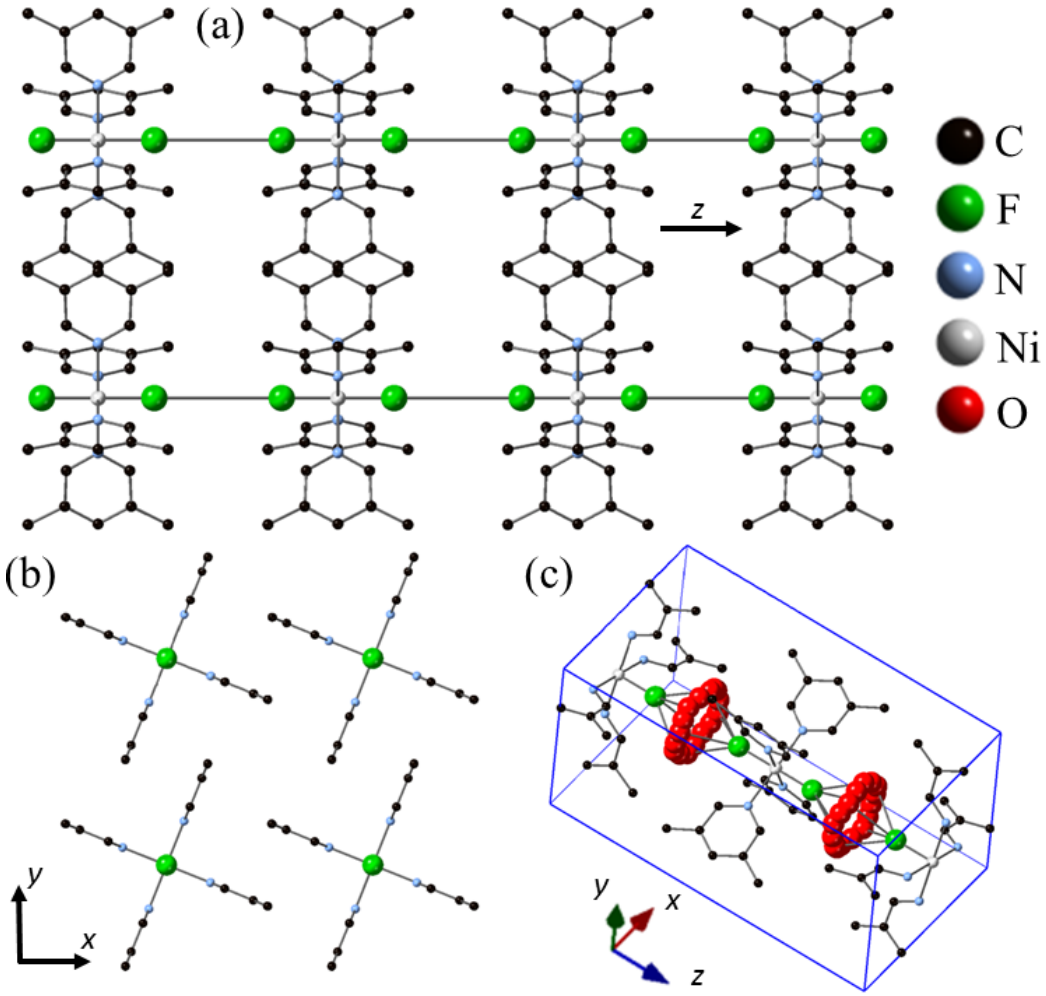

Figure 4.1: Room-temperature structure of $NiF_2(3,5\text{-lut})_4{\cdot}H_2O$ **(a)**: Chains of Ni^{2+} ions (silver) are bridged by two F^- ions (green) along the z-axis. H_2O molecules have been omitted for clarity. **(b)**: Chains are separated in the xy plane by lutidine molecules. **(c)**: Unit cell of $NiF_2(3,5\text{-lut})_4{\cdot}H_2O$. The red ring indicates the structurally disordered oxygen atom from the water molecule. Lutidine and water hydrogen atoms have been omitted for clarity.

size ~ 100 μm were loaded into a Gemini R spectrometer and data taken at room temperature. $NiF_2(3,5\text{-lut})_4{\cdot}H_2O$ is a tetragonal system in the $P/4mcc$ space group. Ni^{2+} ions chains are bridged via Ni-F-H_2O-F-Ni pathways [Fig. 4.1(a)] with nearest neighbour Ni-Ni distance 8.6399(2) Å along the crystal c-direction. The z-axis is defined as being in this direction. The x and y directions are defined as the a and b crystal directions respectively. The oxygen in the water molecule is structurally disordered, as indicated in Fig. 4.1(a). The position of the water hydrogen atoms

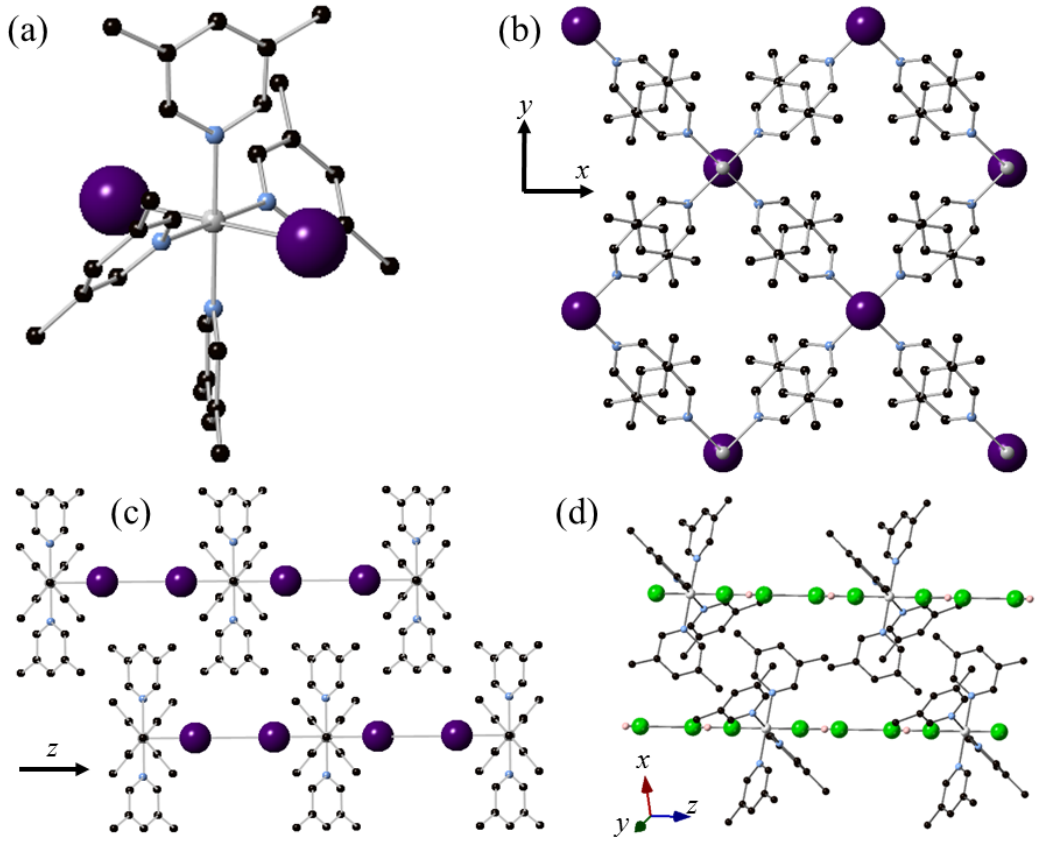

Figure 4.2: 100 K structure of NiX_2(3,5-lut)$_4$. **(a)** Layout of local environment around each Ni^{2+} ion (silver) in NiX_2(3,5-lut)$_4$. **(b)** Lutidine molecules (carbon = black) keep Ni-X-X-Ni chains well separated in the xy-plane. Lutidine hydrogen atoms have been omitted for clarity. **(c)** Ni-X-X-Ni chains in NiX_2(3,5-lut)$_4$ (X= Cl, Br, I = purple). Nickel ions in adjacent chains are offset in the z direction. **(d)** Chains of Ni^{2+} ions are bridged by HF_2^- ions (H = beige and F = green) in Ni$(HF_2)_2$(3,5-lut)$_4$.

could not be resolved. The chains are separated by lutidine molecules and arranged in squares with 9.29750(13) Å between Ni^{2+} ions on adjacent chains [Fig. 4.1(b)]. The local environment around each Ni^{2+} ion is octahedral and compressed along the z-axis (F-Ni-F) [Fig. 4.1(c)]. The equatorial Ni-N bonds are all 2.133(4) Å and symmetric around the axial bond. Ni(3,5-lut)$_4$ planes on individual Ni^{2+} sites are rotated around the z-axis by $\pm 22.5°$ relative to the x and y axis [Fig. 4.1(b),(c)]. This leads to no clear pathway for magnet superexchange between Ni^{2+} ions in the xy plane. Therefore any significant superexchange interactions will likely be along the z-axis.

Single crystal x-ray diffraction measurements of NiX_2(3,5-lut)$_4$ were per-

Table 4.3: Unit cell parameters for NiX_2(3,5-lut)$_4$.

Compound	a,b (Å)	c(Å)	space group
NiF_2(3,5-lut)$_4$·H_2O	9.29750(13)	17.2798(3)	$P/4mcc$
Ni(HF_2)$_2$(3,5-lut)$_4$	11.1000(3)	11.7446(3)	$P4/nnc$
$NiCl_2$(3,5-lut)$_4$	11.4902(9)	10.5512(11)	$P4/nnc$
$NiBr_2$(3,5-lut)$_4$	11.7232(5)	10.1153(4)	$P4/nnc$
NiI_2(3,5-lut)$_4$	12.0048(5)	9.9568(4)	$P4/nnc$

Table 4.4: Bond lengths in NiX_2(3,5-lut)$_4$. NN Ni-Ni corresponds to the nearest neighbour Ni-Ni distance along the Ni-X-X-Ni chains. For Ni(HF_2)$_2$(3,5-lut)$_4$, the Ni-HF_2 distance is between the nickel ion and the adjacent fluorine ion. The HF_2-HF_2 distance is between adjacent fluorines.

Compound	Ni-X (Å)	NN Ni-Ni (Å)	X-X (Å)	Ni-N (Å)
NiF_2(3,5-lut)$_4$·H_2O	2.031(4)	8.6399(2)	4.578(9)	2.133(4)
Ni(HF_2)$_2$(3,5-lut)$_4$	2.0108(12)	11.7446(3)	3.108	2.0922(11)
$NiCl_2$(3,5-lut)$_4$	2.4502(9)	10.5512(11)	5.651(2)	2.122(2)
$NiBr_2$(3,5-lut)$_4$	2.6170(4)	10.1153(4)	4.881(2)	2.121(2)
NiI_2(3,5-lut)$_4$	2.8292(4)	9.9568(4)	4.298(2)	2.123(3)

formed by John Schlueter and Yu-shen Cheng on the 15-ID-B beamline at the Advanced Photon Source, Argonne, USA. Single crystals with size of the order 100 μm were measured at 100 K. The NiX_2(3,5-lut)$_4$ (X=Cl, Br, I, HF_2) compounds are tetragonal systems in the space group $P4/nnc$. Ni^{2+} ions are linearly bridged along the z-axis via the two HF_2^- [Fig. 4.2(b)] or the two halide ions [Fig. 4.2(c)]. In Ni(HF_2)$_2$(3,5-lut)$_4$, the H-F-H ligands are linear along the Ni-HF_2-HF_2-Ni axis. Non-bridging lutidine molecules keep the chains well separated [Fig. 4.2(d)] and nickel ions in adjacent chains are offset from each other in the z direction. Again, there are no clear pathways between adjacent nickel ions in the xy-plane, and therefore it is likely that any dominant magnetic interaction will be through the nickel-halide and nickel-HF_2^- chains. The local environment around each Ni^{2+} ion is octahedral and elongated along the z-axis for X = Cl, Br, I and compressed for Ni(HF_2)$_2$(3,5-lut)$_4$. The nickel octahedra contains four nitrogen atoms from the lutidine molecules and the two halide ions [Fig. 4.2(a)]. All four equatorial bonds are the same length within each compound respectively. Hence the rhombohedral anisotropy parameter E is expected to be zero [33] for all NiX_2(3,5-lut)$_4$.

The relevant structural and bond information for all NiX_2(3,5-lut)$_4$ are given in Table 4.3 and Table 4.4. NiF_2(3,5-lut)$_4$·H_2O has a different structure compared to the other members of the NiX_2(3,5-lut)$_4$ family. Firstly, it contains water molecules in the expected superexchange pathway. Secondly, along with Ni(HF_2)$_2$(3,5-lut)$_4$,

it has an axially compressed local octahedron around the nickel ion. This should change the sign of D compared to the X = Cl, Br, I compounds as they contain axially elongated local octahedra [34]. This is caused by an increase in the Ni-X bond length from F $\rightarrow$ I. However, the Ni-N bond lengths across the NiX_2(3,5-lut)$_4$ are all very similar, making it easier to extract how the single-ion anisotropy changes due to the substitution of the halide ion. Lastly, the trend along the NiX_2(3,5-lut)$_4$ family is for the nearest-neighbour Ni^{2+}-Ni^{2+} distance along the chain to decrease as the size of the Halide ion increases. NiF_2(3,5-lut)$_4$·H_2O does not follow this trend; it has a much smaller nearest-neighbour Ni^{2+}-Ni^{2+} distance compared to $NiCl_2$(3,5-lut)$_4$. The increase in size of bridging halide ions have been shown to contribute to an increase in the strength of magnetic interactions between nickel ions [1]. HF_2^- has also been shown to be good mediator of magnetic exchange in nickel systems [13, 96, 129].

The structures suggest that NiF_2(3,5-lut)$_4$·$H_2O$and NiX_2(3,5-lut)$_4$ can be described using the Hamiltonian:

$$\hat{\mathcal{H}} = D\sum_i \hat{S}_i^{z2} + J\sum_{\langle i,j\rangle} \hat{\boldsymbol{S}}_i \cdot \hat{\boldsymbol{S}}_j + J_\perp \sum_{\langle i,j'\rangle_\perp} \hat{\boldsymbol{S}}_i \cdot \hat{\boldsymbol{S}}_{j'} + \mu_B\mu_0 \sum_i \boldsymbol{H}\cdot\boldsymbol{g}\cdot\hat{\boldsymbol{S}}_i, \qquad (4.1)$$

where J is the nearest-neighbour magnetic exchange interaction between Ni^{2+} ions within the same Ni-X-X-Ni chain and $J_\perp$ is the exchange interaction perpendicular to the chains. Angular brackets denote a sum over unique pairs of metal ions and a primed index indicates an ion in a next to nearest chain, D is the single-ion anisotropy parameter and the final term is the Zeeman splitting.

4.3 NiF_2(3,5-lut)$_4$·H_2O

4.3.1 Magnetisation

Pulsed-field magnetisation measurements of powdered NiF_2(3,5-lut)$_4$·H_2O show a concave rise to saturation at $\approx$ 10 T [Fig. 4.3(a)]. The differential susceptibility drops initially before a small hump at $\approx$ 6 T [Fig. 4.3(b)]. This indicates a ground state crossing between the $m_s = 0$ and $m_s = -1$ energy levels and can be seen as a slight flattening of the $M(H)$ curve around 5 T. The position of the crossing point is given by the midpoint of the peak differential shape in the gradient of the differential susceptibility [Fig. 4.3(b)] and is at 5.7(5) T. The shape of the differential susceptibility is indicative of an easy-plane D-only system with negligible

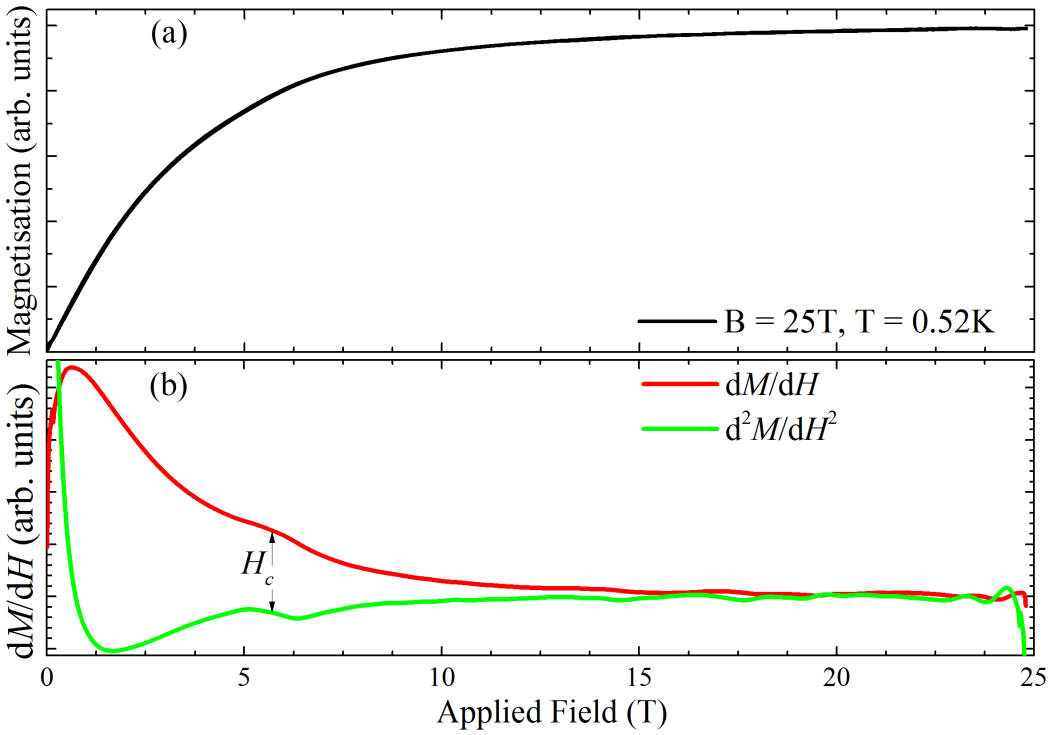

Figure 4.3: **(a)** Low-temperature magnetisation and **(b)** differential susceptibility measurements of $NiF_2(3,5\text{-lut})_4{\cdot}H_2O$. A critical field indicating the ground-state energy-level crossing is observed at $\mu_0 H_C = 5.7(5)$ T.

magnetic interactions. Using Eq. 2.2, the value of 5.7(5) T corresponds to a value of $D = +8.4(7)$ K.

4.4 $Ni(HF_2)_2(3,5\text{-lut})_4$

4.4.1 ESR

High frequency ESR spectra of powdered $Ni(HF_2)_2(3,5\text{-lut})_4$were measured at frequencies of 203.2, 326.6 and 406.4 GHz and a temperature of 20 K. Resonances corresponding to four transitions are clearly observed in the data [Fig. 4.4(a)]. These resonances were fitted to a D-only Hamiltonian, with the resulting parameters extracted: $g_{xy} = 2.23(2)$, $g_z = 2.16(2)$ and $D = \pm 11.97(2)$ K. Frequency dependency is unable to determine the sign of D in D-only powdered compounds [12]. Therefore, a temperature dependant study at 321.6 GHz was performed [Fig. 4.4(c)]. The data shows an increase in the intensity of the low-field xy transition (β) as the temperature decreases. This is due to an increased occupationof the $m_s = -1$ state at low temperatures. At the same time, the intensity of the high-field xy resonance

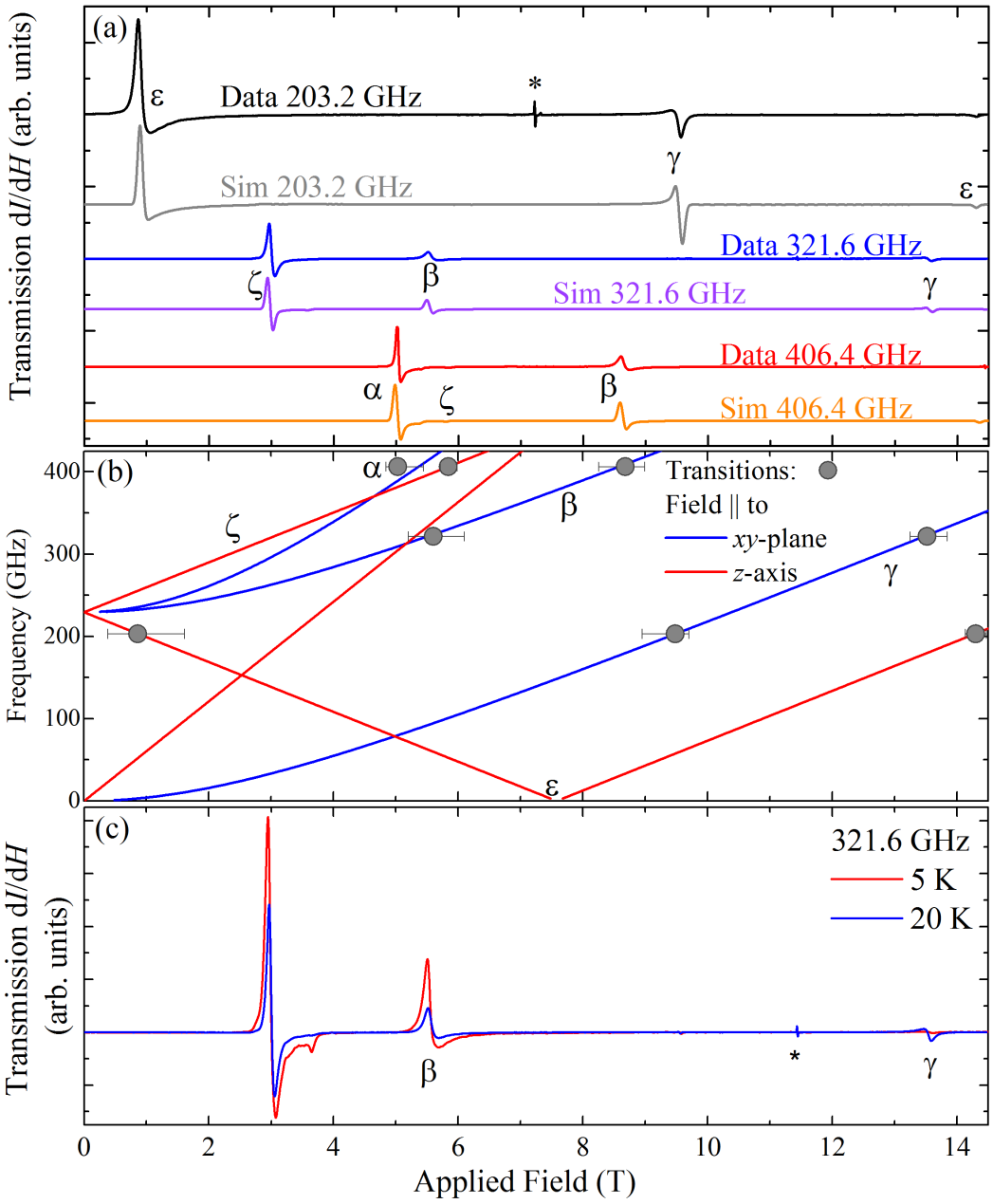

Figure 4.4: **(a)** ESR spectra of $Ni(HF_2)_2(3,5\text{-lut})_4$ made at 20 K and frequencies of 203.2, 321.6 and 406.4 GHz. Large resonances are observed in all three spectra which were fitted using a D-only Hamiltonian. The obtained parameters were then simulated in good agreement with the data. **(b)** The results of the fit to a D only Hamiltonian are $g_{xy} = 2.23(2)$, $g_z = 2.16(2)$ and $D = \pm 11.97(2)$ K, and the position of all transitions are overlaid onto the resonances in good agreement. **(c)** Temperature dependence of the 321.6 GHz $Ni(HF_2)_2(3,5\text{-lut})_4$ ESR spectra. The intensity of the low-field xy transition (β) decreases as temperature increases whereas the high-field transition (γ) increases. This is indicative of easy-plane anisotropy.

(γ) decreases as temperature decreases due to a lowering of the occupation of the $m_s = 0$ state. This shows that $Ni(HF_2)_2(3,5\text{-lut})_4$ exhibits easy-plane anisotropy. Using Eq. 4.12 in Ref. [34], the value of the spin–orbit splitting parameter is $\lambda = -342$ K for $Ni(HF_2)_2(3,5\text{-lut})_4$. This is of the same order as the expected value of -454 K for Ni^{2+} ions. However, the sign of D is different to that which is expected from the axially compressed structure [34]. In conclusion, the ESR data indicates that $Ni(HF_2)_2(3,5\text{-lut})_4$ contains easy-plane anisotropy with $D = +11.97(2)$ K, $g_{xy} = 2.23(2)$ and $g_z = 2.16(2)$. The magnitude of magnetic interactions in $Ni(HF_2)_2(3,5\text{-lut})_4$ has currently not been determined.

Along with $Ni(HF_2)_2(3,5\text{-lut})_4$, the easy-plane anisotropy exhibited in $NiF_2(3,5\text{-lut})_4{\cdot}H_2O$ isn't consistent with what is predicted in Ref. [34]. This suggests that when modelling single-ion anisotropy, it is necessary to not just take the position of atoms around magnetic ions, their respective electronic properties should also be considered. This will be discussed further in Section 4.8.

4.5 $NiCl_2(3,5\text{-lut})_4$

4.5.1 Magnetometry

Pulsed-field magnetisation measurements of powdered $NiCl_2(3,5\text{-lut})_4$ show a concave rise to a broad saturation point [Fig. 4.5(a)]. The $\mathrm{d}M/\mathrm{d}H$ data [Fig. 4.5(b)] is consistent with the simulations for an $S = 1$ easy-plane system with negligible magnetic interactions (Fig. 2.4). There is a weak bump in $\mathrm{d}M/\mathrm{d}H$ at $H_\mathrm{C} = 6.6(5)$ T [Fig. 4.5(b)] which is obtained from the position of the trough in the double differential of the differential susceptibility. This feature is due to the energy-level crossing in easy-plane spin-1 systems and indicates that $D > 0$ for $NiCl_2(3,5\text{-lut})_4$. Using Eq. 2.2, the position of the crossing point corresponds to $D = +9.6(7)$ K.

This energy scale is also observed in the susceptibility data. Powdered samples of $NiCl_2(3,5\text{-lut})_4$ were zero-field cooled to 1.8 K before susceptibility measurements were made at 0.1 T on warming to 300 K. The data rises towards low temperature before it appears to flatten out at ≈ 2 K [Fig. 4.6(a)]. The inverse susceptibility was fitted to a Curie-Weiss model with a small, temperature independent diamagnetic term χ_0 (inset to Fig. 4.6). The parameters extracted are $g = 2.13(1)$, $\theta_\mathrm{W} = +0.23(7)$ and $\chi_0 = -1.46(7) \times 10^{-9}$ $\mathrm{m^3mol^{-1}}$. The data deviates from the Curie-Weiss model below 20 K, strongly suggesting that there is an energy scale acting on the spins of the order of 10 K. Susceptibility measurements have been shown to be accurate at determining the magnitude of the single-ion anisotropy of D-only systems, especially if the sign of D is already known. The data was fitted to

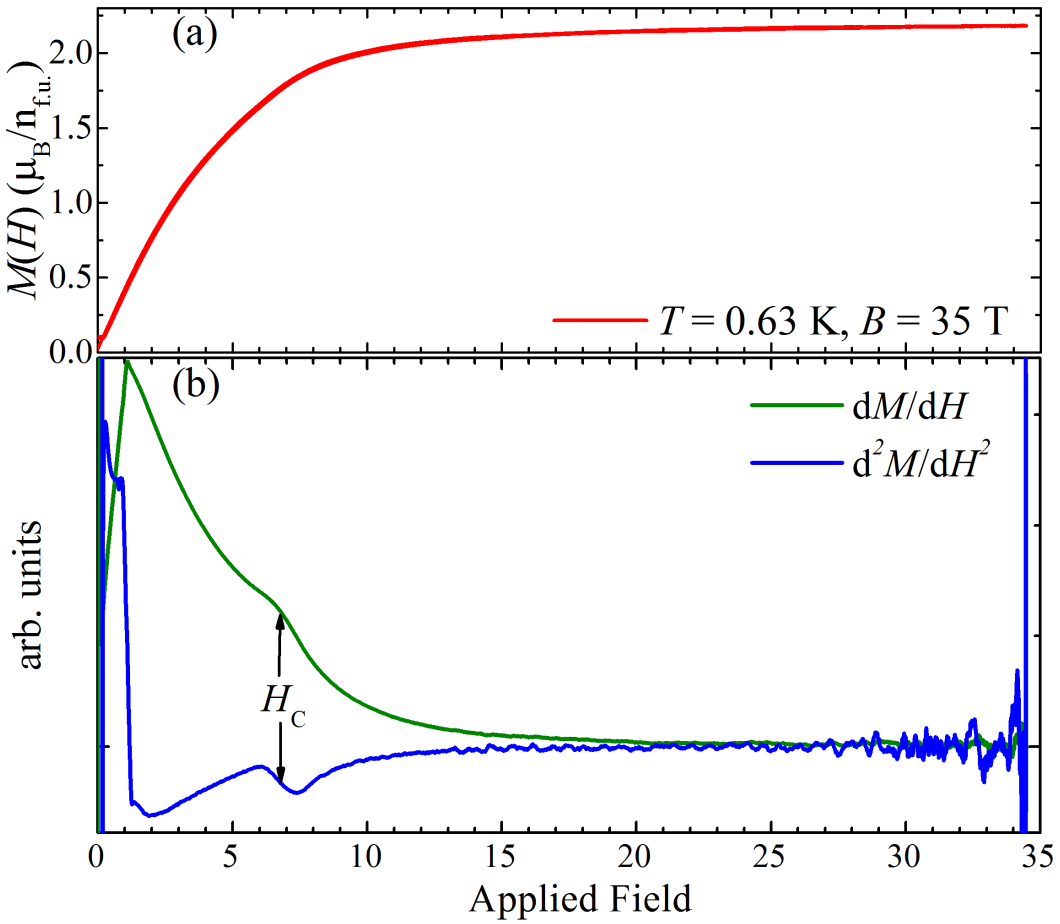

Figure 4.5: **(a)** Pulsed-field magnetisation, **(b)** differential susceptibility and $\mathrm{d}^2M/\mathrm{d}H^2$ measurements of powdered $NiCl_2(3,5\text{-lut})_4$ at $T = 0.63$ K data. H_C indicates the energy-level crossing point described in Fig. 2.4(c)

a D-only susceptibility model [32] and the small χ_0 obtained from the Curie-Weiss fit. The parameters obtained were $D = +10.06(1)$ K, $g = 2.16(1)$ and. The value of D is within the error of the magnitude obtained from the position of the hump in the magnetisation measurements. Both magnetometry measurements are in agreement that $NiCl_2(3,5\text{-lut})_4$ is a D-only easy-plane system of isolated Ni^{2+} moments with $D = 10.06(1)$ K and a powder averaged $g = 2.16(1)$.

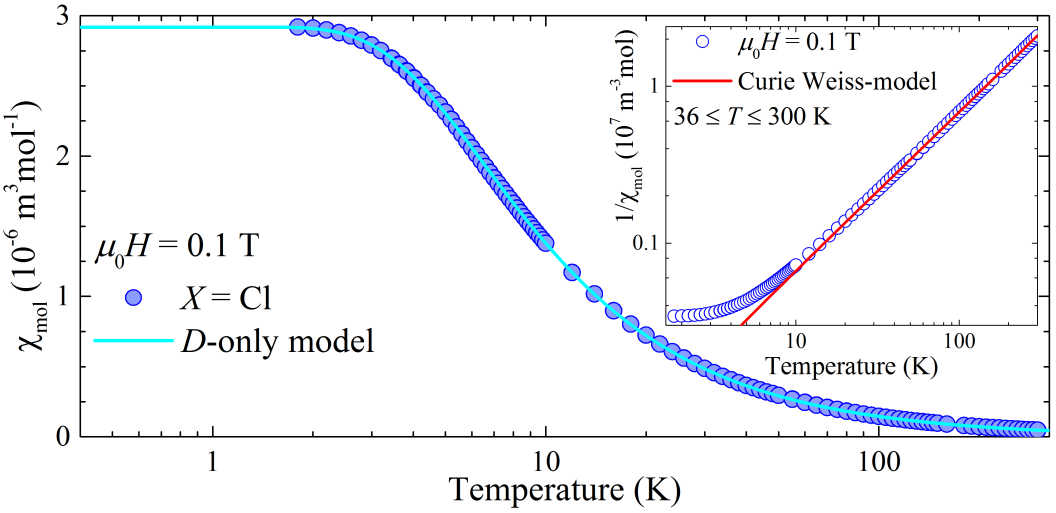

Figure 4.6: DC susceptibility measurements made at an applied field of 0.1 T using a Quantum Design MPMS SQUID of $NiCl_2$(3,5-lut)$_4$. Inset: $\chi^{-1}(T)$ for $NiCl_2$(3,5-lut)$_4$ showing the deviation from the Curie-Weiss model at $T \approx 20$ K.

4.6 $NiBr_2$(3,5-lut)$_4$

4.6.1 ESR

Low-temperature ESR data of powdered $NiBr_2$(3,5-lut)$_4$ [Fig. 4.7(a)] between 197 and 326.4 GHz shows peaks corresponding to resonances where the applied magnetic field is parallel to the z axis and xy plane. The resonance marked with * is likely due to an impurity or end-chain effects. The resonances observed in all the ESR spectra are plotted in Fig. 4.7(b) and were fitted to a D-only Hamiltonian. The extracted parameters are $g_{xy} = 2.17(2)$, $g_z = 2.14(3)$ and $D = +6.4 \pm 1.2$ K. Some transitions occur within the same linewidth, such as ζ and α in the 208 GHz spectra. It is not possible to accurately determine the position of these resonances and as such these were not included in the fit. They are shown as the purple points in Fig. 4.7(b). The expected position of resonances with these parameters are overlaid with the observed resonances and found to be in good agreement. A Simulations using these parameters and a frequency of 326 GHz is plotted in Fig. 4.7(b), consistent with the data. The sign of D is extracted from a temperature dependent study [Fig. 4.7(c)] which shows the low-field xy-transition (β) increasing in intensity as the temperature decreases. This is due to a more populated $m_s = -1$ state and indicates that $D > 0$ for $NiBr_2$(3,5-lut)$_4$. As $g_{xy} > g_z$, this is another indication of easy-plane anisotropy [34]. The calculated value of $\lambda = -427$ K is consistent with the expected value for nickel complexes.

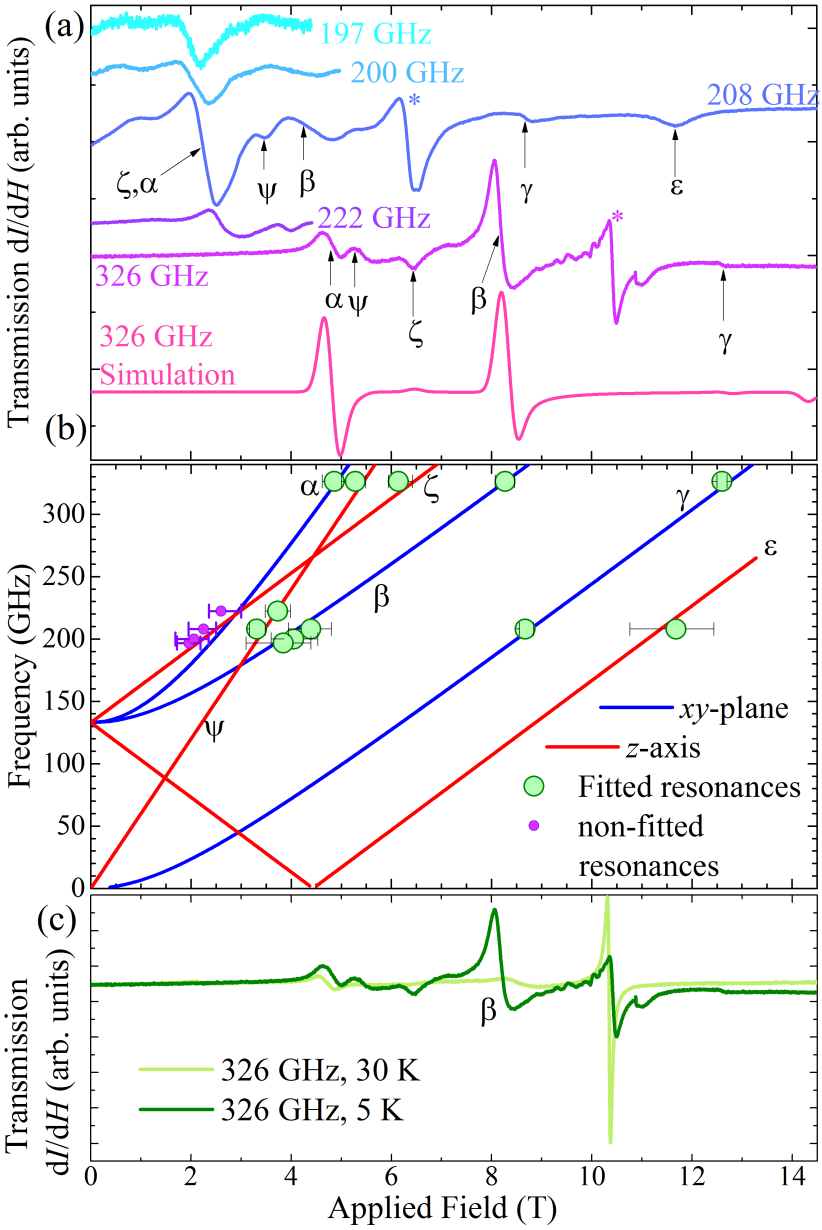

Figure 4.7: **(a)** ESR measurements of powdered $NiBr_2(3,5\text{-lut})_4$ at 5 K. All observed resonances are are labelled depending on which branch they belong to in the field-frequency plot in **(b)**. The resonance marked with * is of an unknown origin but is likely to be an impurity. A Simulation at 326 GHz using the parameters extracted from a D only fit was added and is consistent with the data. **(b)** Fitting the resonances in all the ESR spectra of $NiBr_2(3,5\text{-lut})_4$ to a D-only Hamiltonian. **(c)** Temperature dependent ESR spectra of $NiBr_2(3,5\text{-lut})_4$ at 326 GHz showing the increase in the intensity of the low-field xy transition as temperature drops. This indicates that $D > 0$ for $NiBr_2(3,5\text{-lut})_4$.

4.6.2 Magnetometry

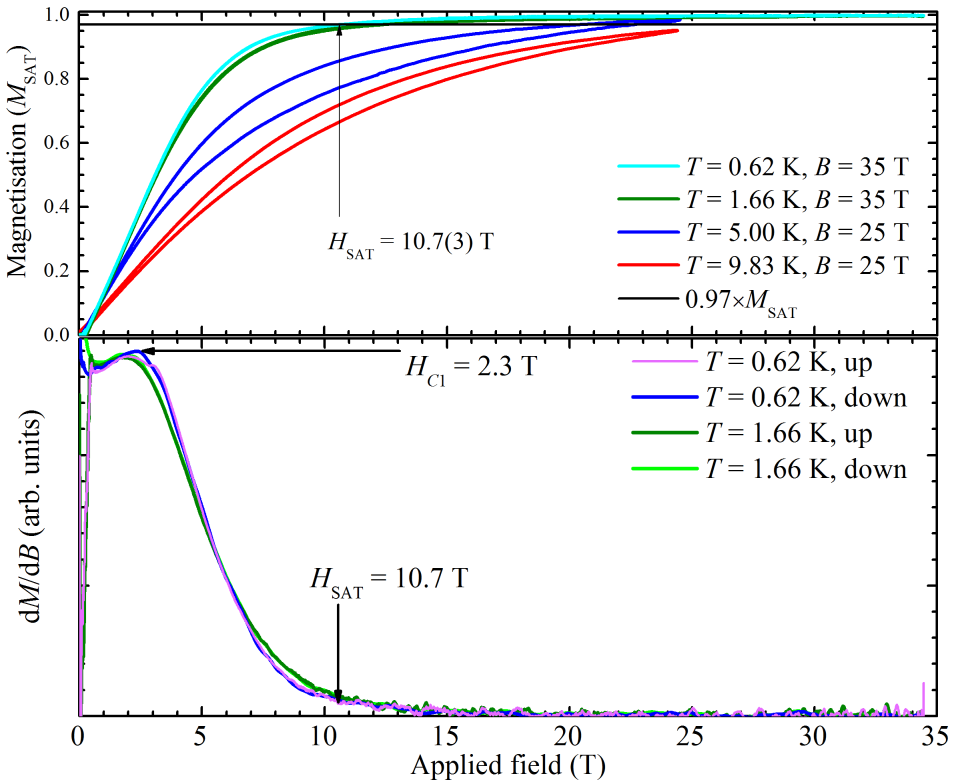

Figure 4.8: **(a)** Low-temperature magnetisation and **(b)** differential susceptibility measurements of powdered $NiBr_2(3,5\text{-lut})_4$.

Pulsed-field magnetisation [Fig. 4.8(a)] measurements of powdered $NiBr_2(3,5\text{-lut})_4$ rise towards a broad transition at the saturation point. The differential susceptibility [Fig. 4.8(b)] shows a peak at $H_{C1} = 2.3(2)$ T and the magnetisation saturates at $H_{SAT} \approx 10$ T. Due to the finite temperature at which the measurement was made, it is very difficult to pinpoint precisely where the magnetisation saturates. H_{SAT} is estimated to be the field at which the magnetisation reaches within 3% of the fully saturated value. This occurs at $H_{SAT} = 10.7(3)$ T. The differential susceptibility is similar to other easy-plane Ni^{2+} systems which contain magnetic interactions (Fig. 3.19). There is no indication of a spin-flop which indicates that $D > 0$. Therefore, using the easy-plane description of the critical fields (Eq. 2.3 and Eq. 2.4) and g=2.10(1), obtained from a Curie-Weiss (CW) fit to $\chi^{-1}(T)$ (see below), values of $J = 0.8(1)$ K and $D = +6(1)$ K are obtained.

DC susceptibility data of powdered $NiBr_2(3,5\text{-lut})_4$ show [Fig. 4.9(a)] an increase in $\chi(T)$ as the temperature is lowered. The inverse susceptibility data

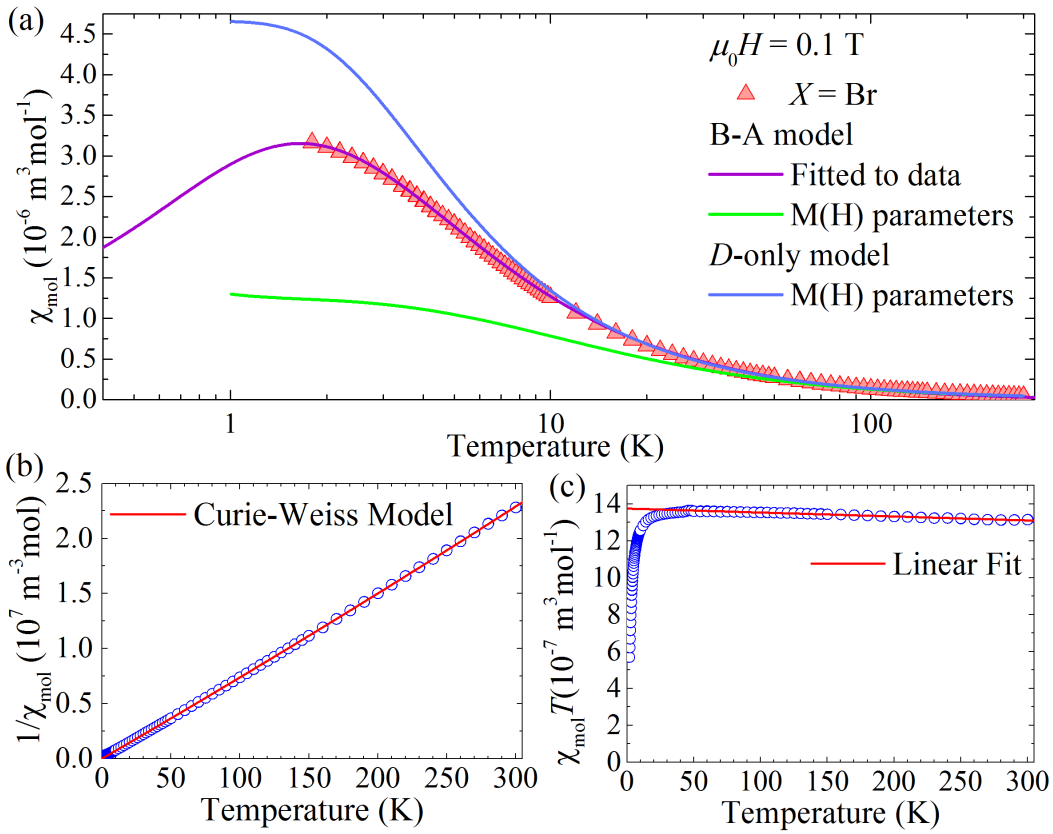

Figure 4.9: **(a)** Susceptibility measurements of powdered $NiBr_2$(3,5-lut)$_4$. Whilst a Borrás-Almenar fit models the data well, the parameters do not agree with other experimental techniques. As it has been shown that many combinations of J and D can give the same fit [13], simulations of the Borrás-Almenar and D-only model using the parameters from the magnetisation measurements were overlaid. There is no agreement with the data and the simulations. **(b)** Inverse susceptibility measurements of $NiBr_2$(3,5-lut)$_4$ show a good agreement with a Curie-Weiss model down to low temperatures. This can be seen more clearly in **(c)** where there is a deviation from a straight line in χT below $\approx$ 30 K.

shows paramagnetic behaviour down to very low temperatures and was fitted to a Curie-Weiss model [Fig. 4.9(b)]. The parameters obtained are $g = 2.10(1)$ and $\theta_W = -0.17(16)$ K. There is also a small temperature independent diamagnetic component with $\chi_0 = -2.14(3) \times 10^{-9}$ $m^3 mol^{-1}$ [Fig. 4.9(c)]. The data can be modelled using the Borrás-Almenar (B-A) model for $S = 1$ AFM chains with easy-plane anisotropy [52]. The fitted parameters are $J = 1.24(3)$ K and $D = +0.7(3)$ K. Though the J parameter is in reasonable agreement with value extracted from the magnetisation measurements, the magnitude of the D parameter is not. It has been shown with this model that numerous combinations of values of J and D can give

an equally good fit [13]. Therefore, the parameters obtained from the magnetisation measurements were used to simulate the expected $\chi(T)$ [Fig. 4.9(a)] using the B-A model. As the magnitude of D was found to be more than J from magnetisation measurements, it is possible that the low fields used cannot pick up the effect of J. Therefore, a simulated D-only model using the parameters from the magnetisation measurements has also been added. The g-factor used in the simulations came from the CW fit [Fig. 4.9(b)]. None of the simulations model the data well.

It has been shown that in the limit of uniform chains the BA model does not agree with Quantum Monte Carlo simulations by Yamamoto and Miyashita, who found that the peak in susceptibility decreases in temperature as the magnitude of D increases [130]. This contradicts the prediction by Borrás-Almenar *et al.* Further calculations by Nakano *et al.* confirmed the results obtained by Yamamoto and Miyashita, and also found that the BA model, whilst accurate for $D = 0$, is incorrect for $D \neq 0$ [131]. Use of the BA model to determine the D parameter from susceptibility data of one-dimensional antiferromagnets have been unsuccessful [132, 133] and most other uses of the model have fixed $D = 0$. Theresult of the fit to the susceptibility data of $NiBr_2$(3,5-lut)$_4$ confirms that the BA model is unsuitable to be used to charactise $S = 1$ antiferromagnets with a significant single-ion anisotropy term in the Hamiltonian. The model proposed by Yamamoto and Miyashita, and Nakano *et al.* is also unable to be used in the analysis of $S = 1$ chains in powdered form as χ_x is yet to be calculated [130, 131]. Due to this, and the accuracy of ESR when determining the single-ion anisotropy parameters, I will use the parameters obtained from the ESR measurements.

4.7 NiI_2(3,5-lut)$_4$

4.7.1 Introduction

NiI_2(3,5-lut)$_4$ has been found to an almost ideal realisation of a Heisenberg antiferromagnet and contains strong magnetic interactions. Using ESR and magnetometry measurements, the parameters $J = 17.5(1)$ K and $|D| = 0.06(4)$ K are extracted. Evidence of an energy gap (Δ) in magnetometry and heat capacity measurements suggest that NiI_2(3,5-lut)$_4$ is a spin-1 chain in the Haldane phase with $\Delta = 6.3(1)$ K. This is consistent with the theoretical prediction for the magnitude of the parameters obtained [4]. ESR and magnetomotry measurements also show evidence of end-chain excitations which act like isolated paramagnetic spin-1/2 moments.

4.7.2 ESR

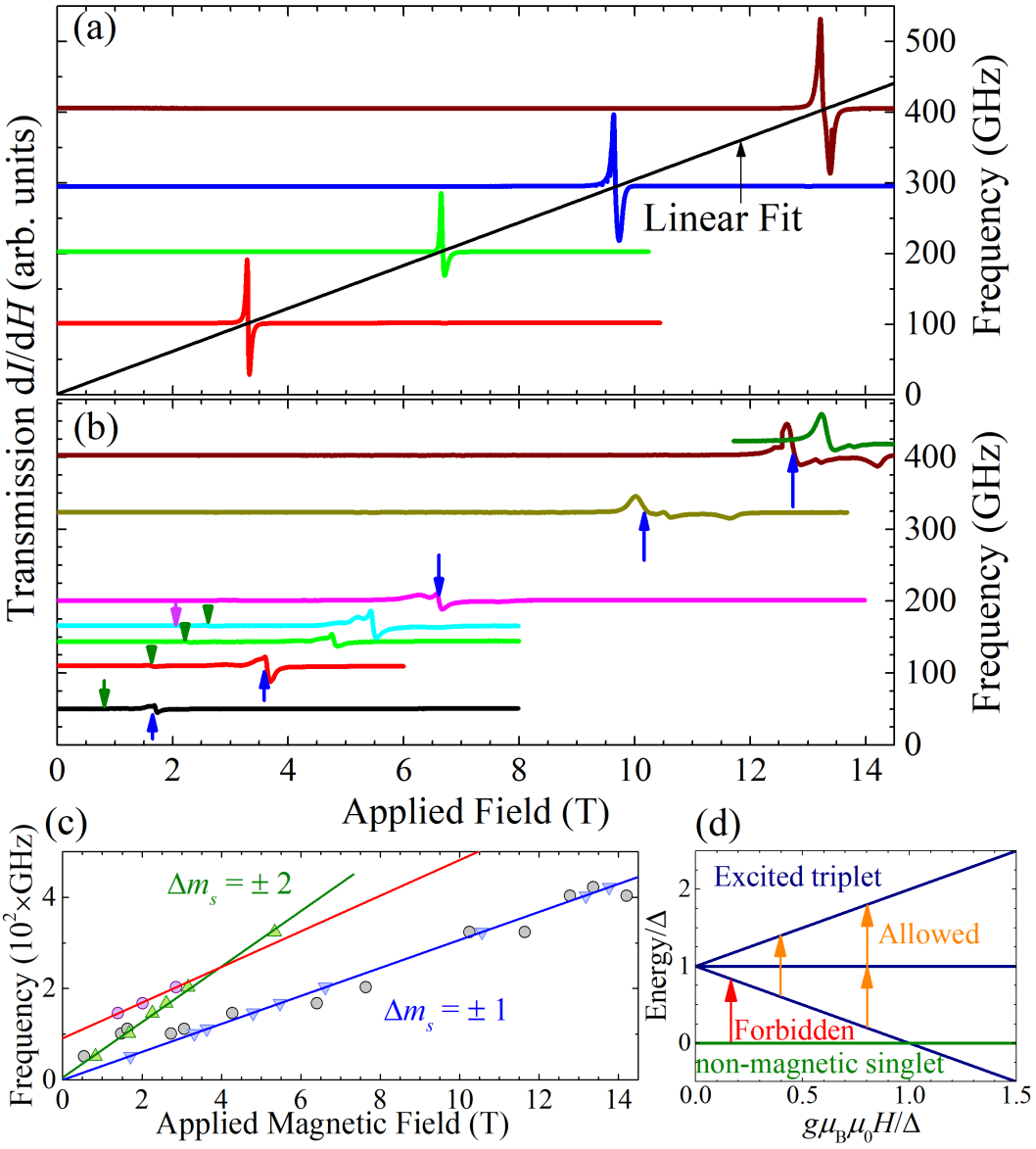

Figure 4.10: Frequency dependent ESR measurements of powdered $NiI_2(3,5\text{-lut})_4$ at **(a)** 30 K and **(b)** 3 K. The positions of the single resonance at 30 K has been modelled with a linear fit (see text). In (b), the blue and green resonances are due to $m_s = \pm 1$ and $m_s = \pm 2$ transitions within the triplet state respectively. **(c)** Resonances observed in the 3 K data are plotted with linear fits. The red resonances are unknown transitions (see text).**(d)** Energy level diagram of a spin-1 AFM chain in the Haldane phase showing the allowed and forbidden ESR transitions.

High temperature, frequency dependent ESR measurements of powdered

NiI_2(3,5-lut)$_4$ at 30 K [Fig. 4.10(b)] show a single resonance which, using a linear fit, extrapolates to $\nu = 1.3(9)$ GHz in zero-field. As 30 K is much higher than Δ, the size of the energy gap extracted from magnetometry and heat capacity data (see below), this resonance is attributed to transitions within an excited triplet state in the Haldane model. In the Haldane model, transitions between the singlet ground state and the excited triplet state are forbidden as they violate momentum conservation [20] [Fig. 4.10(a)]. Transitions have been observed in other compounds, but these contain staggered magnetic field [72, 134, 135]. They are not expected or observed in the ESR spectra of NiI_2(3,5-lut)$_4$ as all the Ni^{2+} sites are equivalent. If the gapped behaviour observed in the magnetisation measurements below were due to a large single-ion anisotropy, this would have been observed in the ESR measurements. They are not and therefore the gapped behaviour in NiI_2(3,5-lut)$_4$ is described using a Haldane model. The zero-field frequency $\nu = 1.3(9)$ GHz corresponds to a single ion anisotropy of $|D| = h\nu/k_B = 0.06(4)$ K, and the gradient of the linear fit of these transitions gives a powder averaged $g = 2.168(1)$. The sign of D cannot be determined from this measurement.

Low-temperature, frequency dependent ESR measurements of powdered NiI_2(3,5-lut)$_4$ at $\approx$ 3 K [Fig. 4.10(c)] show that this resonance splits into up to three different transitions. This could be due to a g-factor anisotropy or the small single-ion anisotropy resolving at low temperatures. Spin-1/2 moments at the end of chains may also contribute to resonances in the range $2 < g < 2.2$ as the ESR transition of $S = 1/2$ spins lie on top of those from $S = 1$ spins with negligible D. The 3 K transitions are also much lower in intensity than the 30 K transitions due to a decreased occupancy of the excited triplet state. Other resonances are caused by the half field transition within the first excited triplet state [Fig. 4.10(d)], whilst there are three resonances in the 140-210 GHz range which cannot be attributed to a particular transition. These may be due to an $S = 1$ impurity with $D \approx 4$ K.

4.7.3 Magnetometry

Pulsed-field magnetisation measurements of NiI_2(3,5-lut)$_4$ [Fig.4.11(a)] shows a small initial rise to a flat plateau at low fields before a kink at $\approx$ 5 T. Above the kink, there is a sharper, approximately linear rise until close to the saturation point where the data shows a concave shape indicative of low-dimensionality [123]. The low-field magnetisation of NiI_2(3,5-lut)$_4$ in the range $0 \leq \mu_0 H \leq 7$ T was also studied using a QDMPMS SQUID [Fig.4.12(b)]. The initial rise in the magnetisation towards a plateau between 2 and 4 T is recreated. The kink at 5 T is also observed. This low-field behaviour is indicative of an energy gap. From the analysis of the ESR

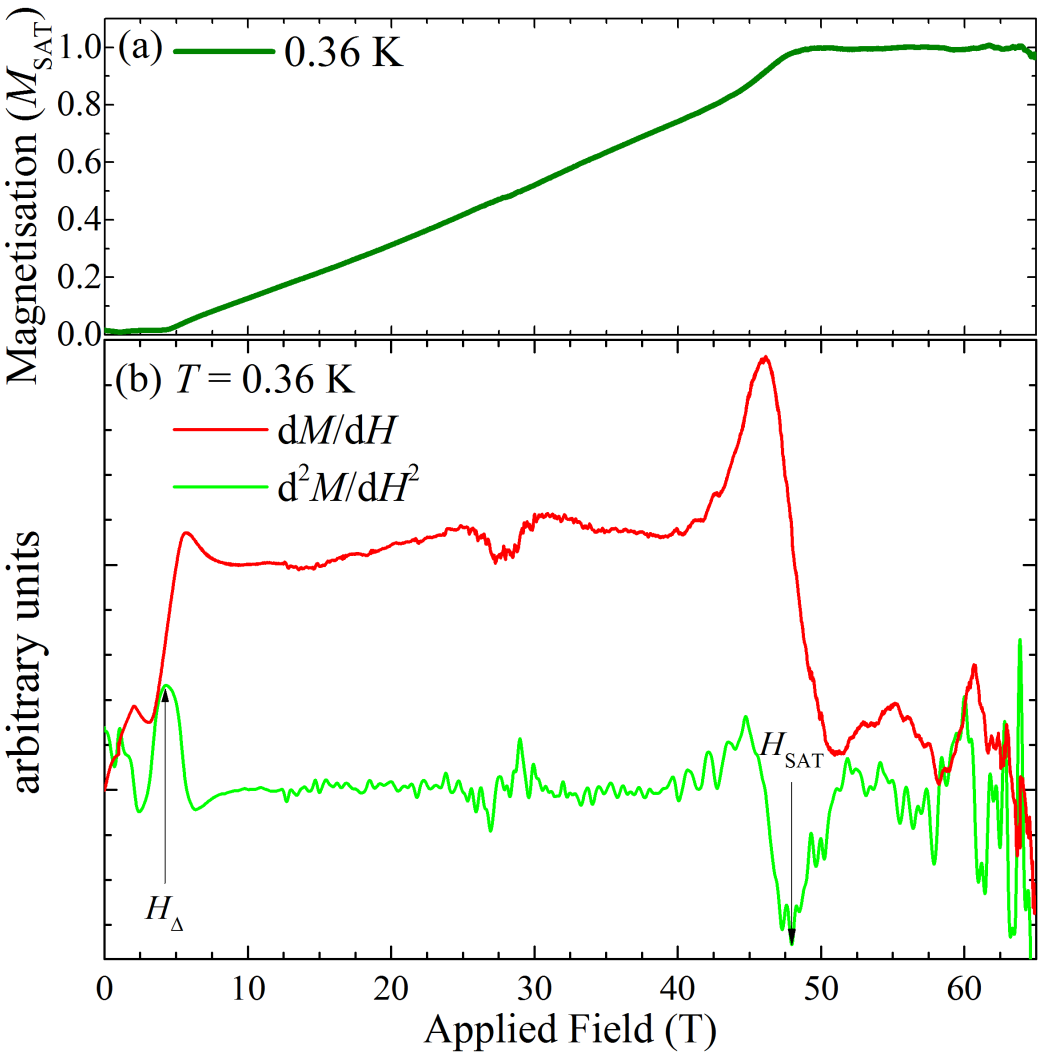

Figure 4.11: **(a)** Low-temperature magnetisation and **(b)** differential susceptibility measurements of $NiI_2(3,5\text{-lut})_4$. See text for an explanation of the critical fields.

above, this energy gap is attributed to a Haldane gap. This is located at the mid-point of rise in dM/dH, which corresponds to the peak in d^2M/dH^2 and occurs at $H_\Delta = 4.4 \pm 0.2$ T. This is taken to be the point at which the Haldane gap has been closed by the magnetic field [62, 67–70, 75]. As ESR reveals $D \approx 0$, the size of the gap will be similar for all orientations of the crystal with respect to the applied magnetic field [70]. The size of the Haldane gap is therefore $\Delta = 6.4 \pm 0.6$ K.

At the lowest temperatures, there is a concave rise to a low-field plateau, which is due to the paramagnetism of $S = 1/2$ moments at the end of chains [81]. These occur due to the Haldane spin chains being within the Valence Bond

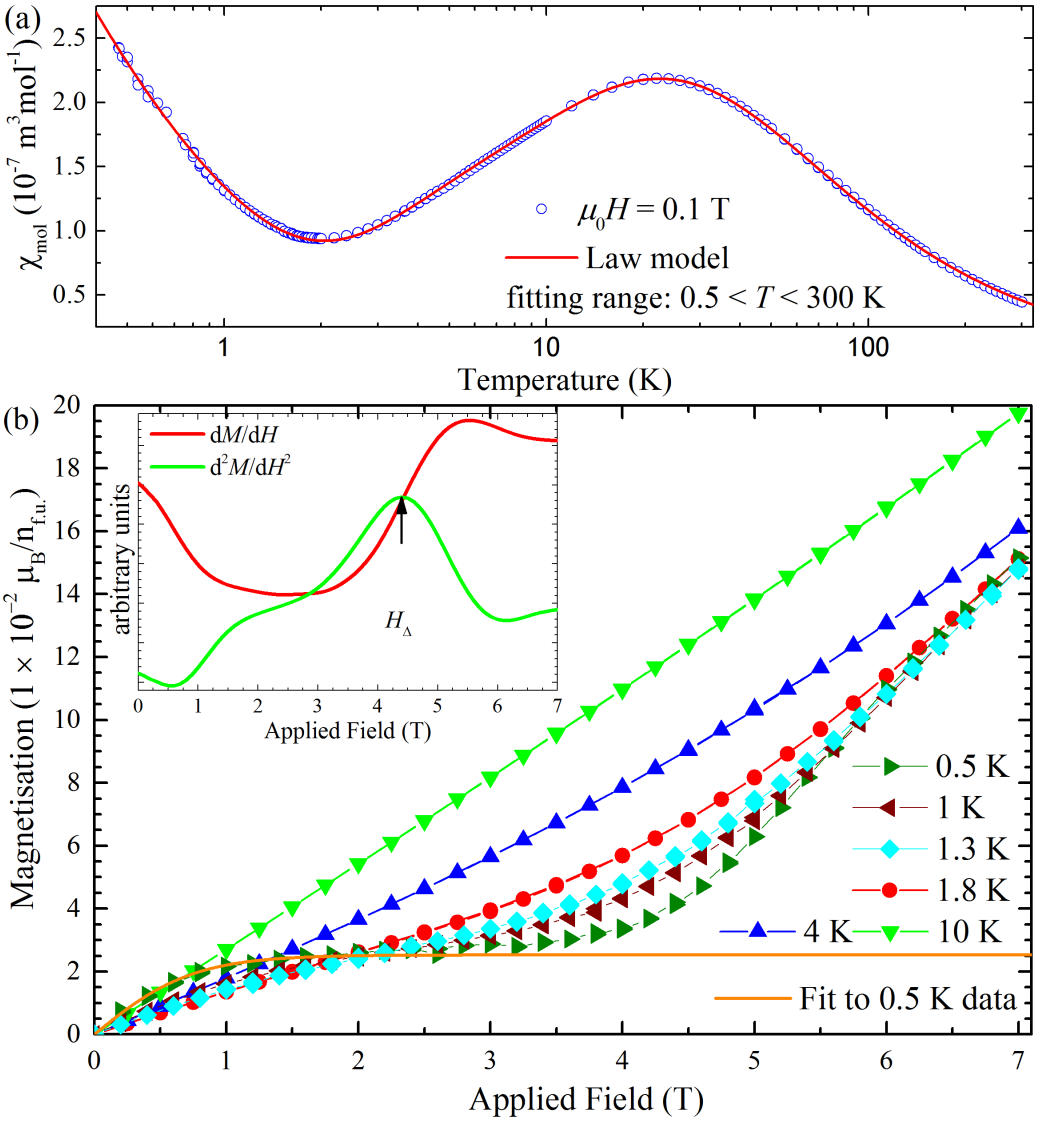

Figure 4.12: **(a)** DC susceptibility measurements of powdered NiI_2(3,5-lut)$_4$ modelled with Eq. 4.3 over the whole data range. **(b)** Quasi-static SQUID magnetisation measurements of powdered NiI_2(3,5-lut)$_4$. The lowest temperature data set has been fitted with Eq. 4.2 in the field range $0 \leq \mu_0 H \leq 2$ T. [Inset]: dM/dH and d^2M/dH^2 of the 0.5 K data showing the field at which the Haldane gap closes.

Solid state described in section 1.4.2. If the chain is very short, then the spin-1/2 moments at either end can interact with each other through the chain. However, this behaviour is not observed in the ESR measurements and therefore I assume that the chains are long enough that the end-chain spins are isolated. To verify that the concave rise is due to $S = 1/2$ end chain spins and not $S = 1$ impurities, the

region below 2 T was fitted to the following model containing an $S = 1/2$ and an $S = 1$ Brillouin function:

$$M(H) = N_{1/2} M_{1/2} B_{1/2} + N_1 M_1 B_1. \tag{4.2}$$

Here, $N_{1/2}$ and N_1 are the proportion of free $S = 1/2$ and $S = 1$ spins, $M_{1/2}$ and M_1 are the saturation fields for spin-1/2 and spin-1 paramagnets, and $B_{1/2}$ and B_1 are the Brillouin functions for spin-1/2 and spin-1 paramagnets [24], respectively. The resultant fit gives the parameters $N_{1/2} = 0.0253(2)$ and $N_1 = 0$. This confirms that the end-chain spins in NiI_2(3,5-lut)$_4$ are $S = 1/2$ moments, as expected via the valence bond solid model [78, 80].

The differential susceptibility of the pulsed-field measurements show two critical fields [Fig. 4.11(b)], the first one at $H_\Delta = 4.3(1)$ T ($\Delta = 6.3(1)$ K), which is the point at which the Haldane gap has been closed by the magnetic field. The second critical field $H_J = 48.0(1)$ T occurs when the moments are fully saturated by the applied magnetic field. As NiI_2(3,5-lut)$_4$ has negligible single-ion anisotropy, H_J is a direct measure of the magnitude of J (See H_{SAT} in Eq. 2.4). Using Eq. 2.4, a value of $J = 17.5(1)$ K is calculated. Using the value of D from the ESR measurements, the ratio $|D/J| \sim 10^{-3}$ is consistent with NiI_2(3,5-lut)$_4$ being in the Haldane phase [4].

DC Susceptibility measurements of powdered NiI_2(3,5-lut)$_4$ [Fig. 4.12(a)] exhibits a large, broad peak at 20 K, indicating the build-up of short range correlations. At temperatures below the peak the susceptibility drops towards zero until $\approx$ 2 K where there is an upturn due to end-chain spins [64, 70, 136]. This is expected due to the powdered nature of the sample. From the analysis of the ESR data, $D \ll J$ and the data can be fitted to the following model with two contributions

$$\chi = 2x\chi_{FS} + (1 - x)\,\chi_{chain}. \tag{4.3}$$

Here, χ_{chain} is the susceptibility of Heisenberg antiferromagnetic chains for various spin values from the Padé approximation derived by Law *et al.*, and includes a term to account for Δ [51]. χ_{FS} is a Curie-Weiss term that accounts for the free $S = 1/2$ spins. Eq. 4.3 models both the high and low temperature regimes of the data very well [Fig. 4.12(b)], with the parameters $J = 18.4(1)$ K, $\Delta = 7.44(1)$ K and $x = 0.0169(1)$ extracted, reasonably consistent with the parameters extracted from the $M(H)$ measurements.

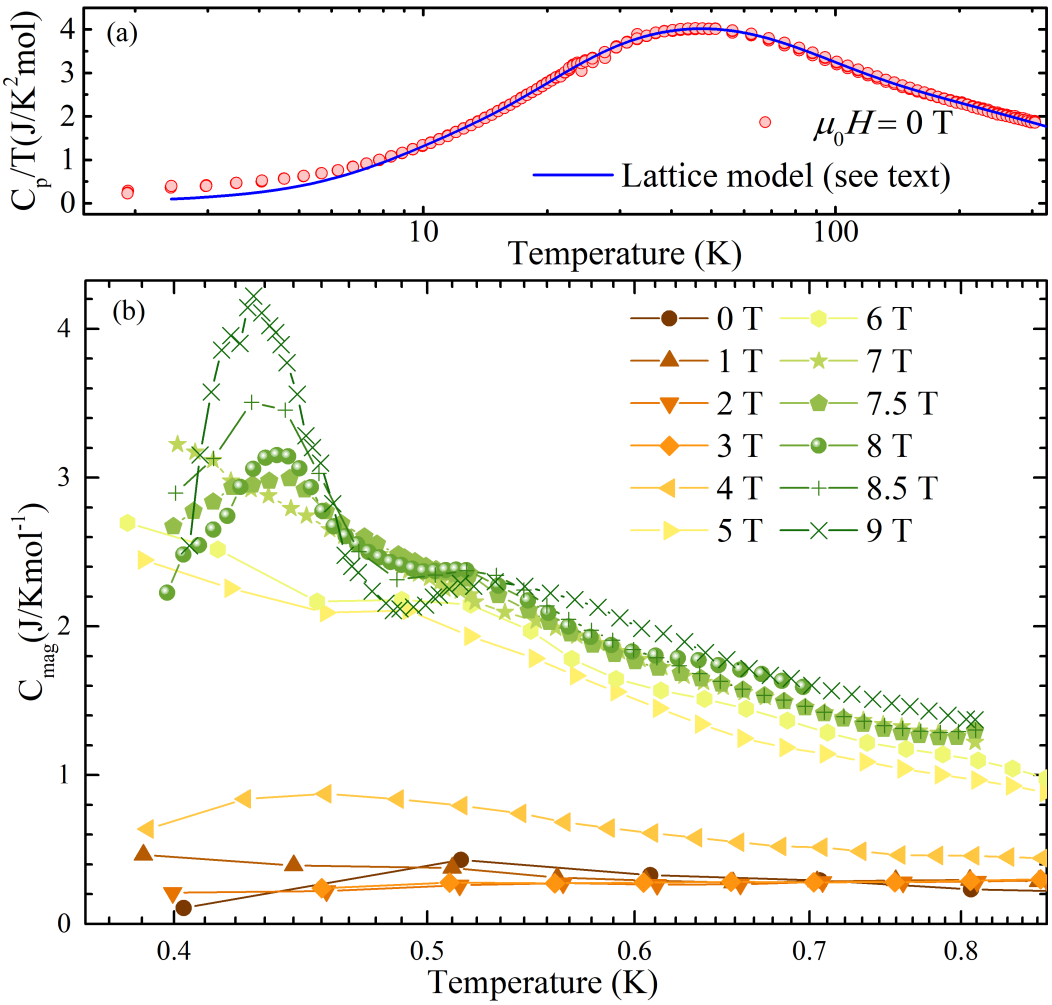

Figure 4.13: **(a)** Zero-field heat capacity measurements of powdered NiI_2(3,5-lut)$_4$ pressed into a pellet show a large and broad hump due to the lattice contribution at high temperatures. This was fitted to a model with one Debye and three Einstein modes over the range $10 \leq T \leq 300$ K. **(b)** Magnetic heat capacity of NiI_2(3,5-lut)$_4$ at a different fields in the range $0 \leq T \leq 9$ T.

4.7.4 Heat capacity

Heat capacity measurements of powdered NiI_2(3,5-lut)$_4$ pressed into a pellet exhibits a large, broad peak in the C_p/T zero-field data at ≈ 45 K [Fig. 4.13(a)]. This occurs due to phonons and is modelled using one Debye mode and three Einstein modes. The best lattice fit was over the range $10 \leq T \leq 300$ K. The parameters of the fit is shown in Table. 4.5 which was subtracted from the total heat capacity. The resultant low-temperature magnetic heat capacity of NiI_2(3,5-lut)$_4$ [Fig. 4.13(b)] show a peak appearing at $T = 0.43(1)$ K for $\mu_0 H \geq 7.5$ T (Fig. 4.13). Though it is

Table 4.5: Lattice fit parameters for NiI_2(3,5-lut)$_4$ obtained from modelling high-temperature zero-field heat capacity data.

A_{D}	63(4) K
θ_{D}	68(2) K
A_{E1}	182(4) K
θ_{E1}	118(3) K
A_{E2}	159(5) K
θ_{E2}	252(8) K
A_{E3}	304(6) K
θ_{E3}	833(17) K

quite broad, it is attributed to a transition associated with field-induced long-range order. This feature is further evidence of an energy gap and that NiI_2(3,5-lut)$_4$ lies in the Haldane phase [6, 70, 71]. The broadness of the peak is likely to be caused by the small single-ion anisotropy in NiI_2(3,5-lut)$_4$ resolving at the highest fields. The peak due to the onset of long range order is also located at approximately the same temperature for field sweeps in the range $7.5 \leq \mu_0 H \leq 9$ T. This kind of behaviour has been observed in NDMAP [6, 71, 72] which is another spin-1 AFM chain in the Haldane phase. The peak then drops out of the temperature range of the heat capacity probe (≈ 0.4 K) for $\mu_0 H \leq 7$ T. There is a sharp drop in the magnitude of C_{mag} as the field decreases below 5 T, indicating that indicating that the Haldane gap is in the range $4 < \Delta < 5$ T. This is consistent with the magnetometry measurements.

4.7.5 Discussion

NiI_2(3,5-lut)$_4$ has been shown to be an almost ideal spin-1 Heisenberg antiferromagnetic chain within the Haldane phase. The appearance of the peak in a heat capacity above 7.5 T is evidence of the closing of the Haldane gap, though the peak moves out of the temperature range of the probe for $\mu_0 H \leq 7$ T. However, the position of the kink in the magnetisation measurements gives the size of the gap as $\Delta = 6.4(6)6$ K. The strength of the intra-chain magnetic interaction extracted is $J = 17.5(2)$ K. Theoretical calculations predict that the ratio $\Delta/J = 0.41191$ for isotropic $S = 1$ chains [51], and the ratio $\Delta/J = 0.36(4)$ obtained for NiI_2(3,5-lut)$_4$ is within 15% of the predicted value. Magnetometry measurements also show features associated with free spin 1/2 moments at the end of chains. By fitting to a Brillouin function, 2.53(2) % of the saturation magnetisation is due to these end chain spins. The limit of $D < 0.1$ K obtained from high-field ESR measurements gives $|D/J| < 5.7 \times 10^{-3}$,

which is smaller than that of $CsNiCl_3$ which has the ratio $|D/J| < 8.9 \times 10^{-3}$ [137]. Though the value of $|D/J| = 2 \times 10^{-4}$ is smaller for $AgVP_2S_6$ [138], the much larger magnitudes of J and D make $AgVP_2S_6$ a poor choice for probing the Haldane phase with commercially available lab-based equipment. This suggests that NiI_2(3,5-lut)$_4$ can be considered to be one of the most isotropic $S = 1$ Heisenberg AFMs currently known. Most other Haldane spin-1 chains currently known contain sizeable single-ion anisotropy [139]. NiI_2(3,5-lut)$_4$ is therefore an excellent candidate for new areas of experimental research into the near-ideal Haldane phase. This is due to the flexibility of coordination chemistry, in which constituent parts can be swapped almost at will, and the low fields required to accurately characterise this compound. Transition metal - doped halide superexchange pathways have already been shown to induce Mott (for $H = 0$) and Bose (for $H > 0$) glass phases and a possible quantum Griffiths phase in the Br-doped quantum paramagnet DTN [140, 141]. As will be seen in the next chapter, halide substitution has been used to experimentally study magnetic exchange disorder in quasi two-dimensional $S = 1/2$ antiferromagnets. As the other members of the NiX_2(3,5-lut)$_4$ family do not lie in the Haldane phase, one can use NiI_2(3,5-lut)$_4$ to test theories on bond disorder between magnetic sites parallel and perpendicular to the spin-chain [73]. Introducing a second non-bridging ligand is likely to break the axial symmetry, introducing an E term into the Hamiltonian. This can be used to investigate the predictions of quantum phase transitions that occur due to rhombic-type single-ion anisotropy in Haldane spin chains [142].

4.8 Summary

All the members of the NiX_2(3,5-lut)$_4$ family, apart from X = I which is almost Heisenberg-like, and NiF_2(3,5-lut)$_4$·H_2O have been shown to contain easy-plane single-ion anisotropy. $NiBr_2$(3,5-lut)$_4$ and NiI_2(3,5-lut)$_4$ also contain significant magnetic interactions between adjacent Ni ions along the Ni-X-X-Ni chains (Table. 4.6). ESR suggests that Ni$(HF_2)_2$(3,5-lut)$_4$ contains easy-plane single-ion anisotropy with $D = +11.97(2)$ K and magnetometry data indicate that NiF_2(3,5-lut)$_4$·H_2O is a D-only system with a magnitude of $D = +8.4(7)$ K. Magnetometry data suggests that $NiCl_2$(3,5-lut)$_4$ contains negligible magnetic interactions with $D = +9.6(2)$ K. ESR and magnetisation measurements are consistent with $NiBr_2$(3,5-lut)$_4$ containing both $J = 0.8(1)$ K and $D = +6.4(1.2)$ K. ESR, magnetisation and susceptibility show that NiI_2(3,5-lut)$_4$ is a spin-1 AFM chain in the Haldane phase with $D = +0.6(4)$ K, $J = 17.5(1)$ K and $\Delta = 6.3(1)$ K. The

Table 4.6: Experimentally derived parameters for NiX_2(3,5-lut)$_4$.

Compound	J (K)	D (K)
NiF_2(3,5-lut)$_4$·H_2O	≈ 0	8.4(7)
Ni$(HF_2)_2$(3,5-lut)$_4$	-	11.97(2)
$NiCl_2$(3,5-lut)$_4$	≈ 0	+10.06(2)
$NiBr_2$(3,5-lut)$_4$	0.8(1)	+6.4(1.2)
NiI_2(3,5-lut)$_4$	17.5(1)	±0.06(4)

very small magnitude of D compared to J makes NiI_2(3,5-lut)$_4$ one of the most Heisenberg-like $S = 1$ AFM chains in the Haldane phase (Fig. 1.3).

There are two trends linking the structures and the magnetic properties of NiX_2(3,5-lut)$_4$. Firstly, there is an increase in J as adjacent nickel ions move closer together and the size of the bridging ion increases. However, NiF_2(3,5-lut)$_4$·H_2O doesn't follow this behaviour as nickel ions are much closer together than $NiCl_2$(3,5-lut)$_4$ but contains no significant J. This can partly be explained by the water molecule in between the fluorine ions inhibiting magnetic interactions. This is observed in the compounds in the previous chapter that all contain water ligands which appear to inhibit magnetic exchange. In NiX_2(3,5-lut)$_4$, as the ionic radii of X increases, the adjacent nickel ions within the chains get closer together. In the quasi two-dimensional NiX_2(pyz)$_2$ however, the nickel ions get further apart as the ionic radius increases. Both families show increasing strength of magnetic interactions through the Ni-X-X-Ni linkages as the size of X increases. This suggests that the size of the bridging ion has a more significant contribution to the strength of the superexchange interaction than the distance between Ni^{2+} ions.

The second trend is the decrease in the magnitude of D as the size of the halide ligand increases (Fig. 4.14). The halide ligand also moves further away from each Ni^{2+} ion as the size of the halide ion increases. A previous study investigated various Ni^{2+} compounds with the octahedra NiN_6, $NiN_4N'_2$, NiN_4O_2 and $NiN_2O_2O'_2$ (the accent represents a ligand from a different donor set) in an attempt to study how D changed with local structure. It was found that the weakening of axial ligand's crystal field and therefore an elongation of the axial bond made D more positive, whilst a compression turned D more negative [35]. An experimentally calculated quantitative dependence of D on the structure of Ni^{2+} octahedra was obtained which was roughly linear through approximately zero ($D = 0$ for symmetric octahedra). The behaviour of the the NiX_2(3,5-lut)$_4$ family does not follow this behaviour. This is due to the different ligands involved in NiX_2(3,5-lut)$_4$. The model may hold if the composition of the octahedra is kept constant and the bond

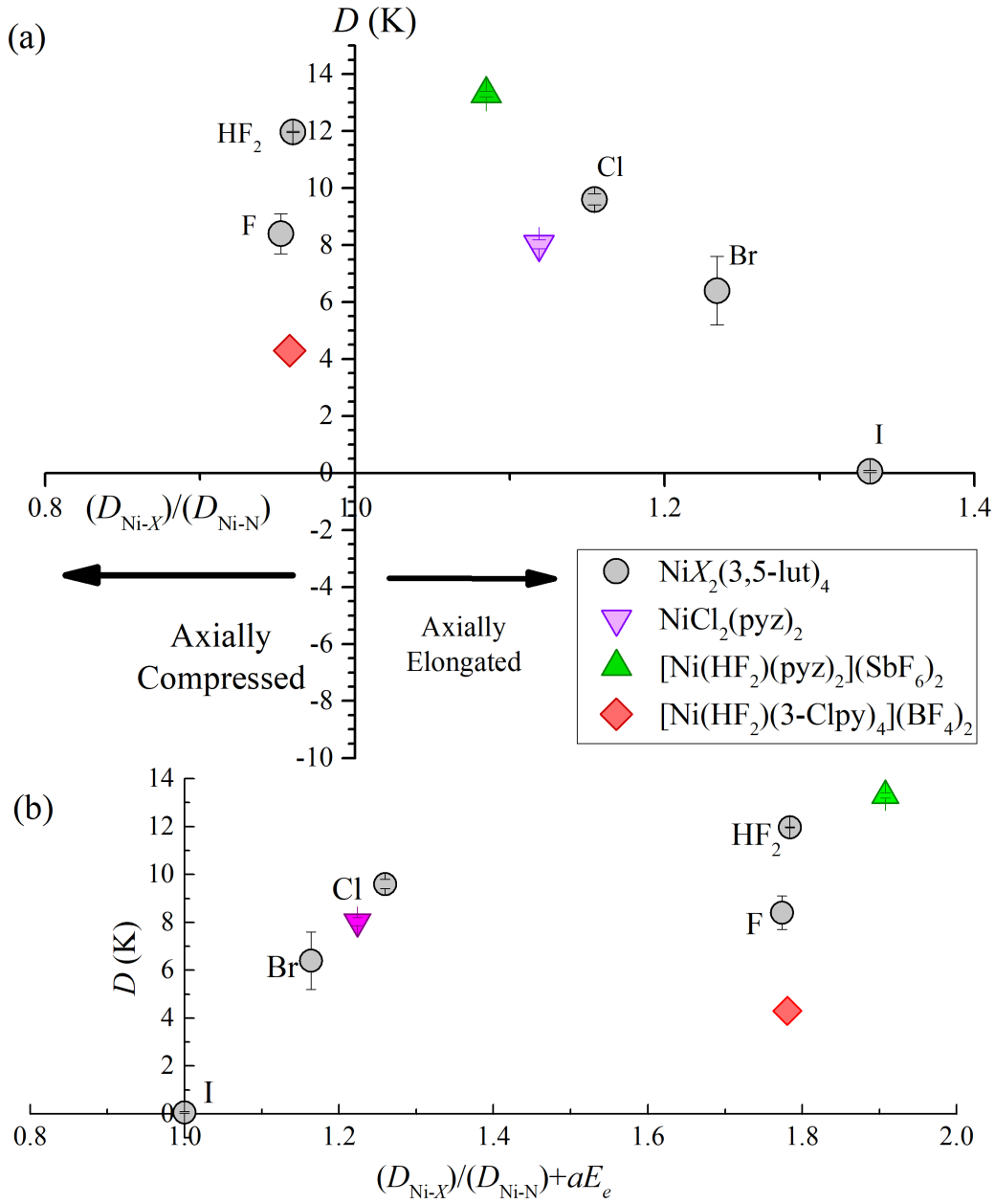

Figure 4.14: **(a)** Effect of bond lengths in the NiX_2N_4 octahedra in $NiX_2(3,5\text{-lut})_4$ on the magnitude of the single-ion anisotropy parameter D. $D_{\mathrm{Ni}-X}$ is the Ni-halide bond length and $D_{\mathrm{Ni}-\mathrm{N}}$ is the Ni-N bond length. The y axis is positioned at $D_{\mathrm{Ni}-X}/D_{\mathrm{Ni}-\mathrm{N}} = 1$ which corresponds to a symmetric local environment around the $Ni^{2=}$ ion. The previously published structural and D parameters of $NiCl_2(pyz)_2$ [1], $[Ni(HF_2)(pyz)_2](SbF_6)_2$ [13] and $[Ni(HF_2)(3\text{-Clpy})_4](BF_4)_2$ [10] have been used. **(b)** Effect of the electronegativity difference between the halide ions and the N atoms (E_e) has on D in NiX_2N_4 octahedra. $NiI_2(3,5\text{-lut})_4$ has been set at $D_{\mathrm{Ni}-X}/D_{\mathrm{Ni}-\mathrm{N}} + aE_e = 1$, where $a = 0.875$ is a calibration factor (see text).

lengths are changed. For example, $NiCl_2$(3,5-lut)$_4$ has a more elongated octahedra compared to $NiCl_2$(pyz)$_2$ and has a bigger magnitude of D (Fig. 4.14). However, the structure dependence of D for NiN_4F_2 octahedra is not consistent. Thus the prediction that an axial ligand with a strong (weak) crystalline-electric field causes a negative (positive) value of D [34] appears to be incorrect in this case.

Along with the results of the previous chapter for NiN_4O_2, NiN_2O_4 and NiN_4OF octahedra, this suggests that the moments on the nickel ions may prefer to point away from the most electronegative ligand. For NiX_2(3,5-lut)$_4$, this explains why octahedra with fluorine and chlorine ions, which are more electronegative than nitrogen [126], are easy-plane. However, bromine and iodine are less electronegative than nitrogen but $NiBr_2$(3,5-lut)$_4$ has $D > 0$ and NiI_2(3,5-lut)$_4$ is almost Heisenberg-like. Therefore, the electronegative argument doesn't fully explain the behaviour of $NiBr_2$(3,5-lut)$_4$ and NiI_2(3,5-lut)$_4$. To further investigate this, an electronegativity term aE_e was added to the x-axis in Fig. 4.14(a). $E_e = E_X - E_{\mathrm{N}}$ is the difference in the Pauling electronegativity values of the halide ions and the nitrogen atoms in the NiX_2N_4 octahedra. The constant $a = 0.875$ was calibrated by setting NiI_2(3,5-lut)$_4$ to $D_{\mathrm{Ni}-X}/D_{\mathrm{Ni}-\mathrm{N}} + aE_e = 1$. This is due to NiI_2(3,5-lut)$_4$ being almost Heisenberg-like. The resultant graph is shown in Fig. 4.14(b). The X = Cl, Br, I data shows an approximately linear relationship between $D_{\mathrm{Ni}-X}/D_{\mathrm{Ni}-\mathrm{N}} + aE_e$ and D. This indicates that there is a mixture of crystal field and electronegative effects that both contribute to the single-ion anisotropy in six-coordinate Ni^{2+} compounds.

However, the X = F data does not follow a discernible trend. This may be due to the different structures that Ni-F compounds have compared to the other Ni-halide compounds. The size of the F^- ion means that undesired molecules may enter into the crystal, such as the water molecule in NiF_2(3,5-lut)$_4$·H_2O. Also, the chemical process used to process the Ni-F compounds can introduce HF_2 molecules instead of F^- ions. The effect that HF_2 and the additional molecules has on D may be more complicated than the simplistic model based on NiF_2N_4 octahedra. More measurements on suitable compounds are required to explore this further.

Chapter 5

Effect of magnetic exchange disorder in a quasi-two dimensional Cu^{2+} antiferromagnet

5.1 Introduction

This aim of this chapter is to investigate the effect of random exchange strength in a quasi two-dimensional (Q2D) spin-1/2 antiferromagnet. Bond-disorder in insulating magnetic systems reduces the connectivity of the lattice, leading to a percolative phase transition beyond which the system is broken up into small finite clusters. Classically, the percolation transition is coupled to the magnetic transition (destruction of long-range order), but in quantum systems the progressive reduction in lattice connectivity enhances quantum fluctuations. In one-dimensional magnetic systems an infinitesimally small amount of disorder is required to destroy long-range order. However, the Hamiltonian of the two dimensional antiferromagnet is more robust to the onset of long-range order, enabling the study of these quantum effects. For interacting $S = 1/2$ moments on square lattices, there are currently two theories which predict the behaviour of the ground state as bond disorder increases. The first, which is based on numerical calculations, suggests that the ground state of the system is stable until the percolation limit is reached. Therefore, disorder has reduced relevance on quantum Heisenberg models with a dimensionality $D > 1$ [110]. The alternative theory predicts multicritical points that separate the magnetic transition from the percolation transition, introducing a quantum phase transition and

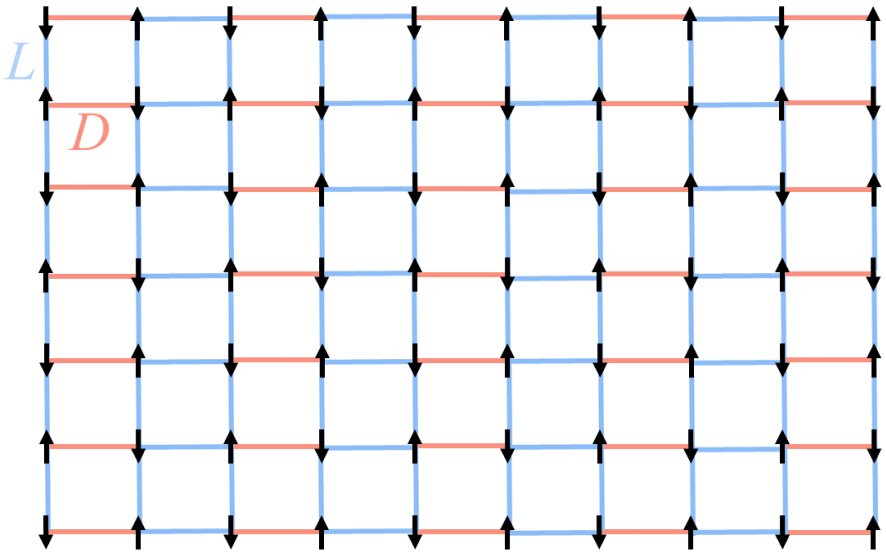

Figure 5.1: Decomposition of an antiferromagnetic square lattice into dimer (D - light red) and ladder (L - light blue) bonds.

quantum disordered phase [109]. This occurs due to inhomogeneous bond disorder. If a square lattice is decomposed into dimer and ladder (inter-dimer) bonds (Fig. 5.1), with the number of dimer bonds P_{D} and latter bonds P_{L} in the lattice, then homogeneous bond disorder occurs for $P_{\mathrm{D}} = P_{\mathrm{L}}$ whereas inhomogeneous disorder happens when $P_{\mathrm{D}} \neq P_{\mathrm{L}}$. Inhomogeneous bond disorder leads to strongly fluctuating quantum states, such as dimer singlets, which significantly enhance quantum fluctuations. This destroys long-range order before the percolation limit is reached, and may lead to a quantum Griffiths phase. The Griffiths phase leads to arbitrarily large magnetically ordered regions formed within the paramagnetic phase at $T > T_{\mathrm{N}}$ [143].

Due to the flexibility of coordination polymer chemistry, bond disorder has been realised by doping with different halide ions within the superexchange pathway. Previous measurements on Cu^{2+}-halide and Ni^{2+}-halide superexchange pathways have indicated that substituting different halide ions will change the strength of magnetic interactions between the transition metal ions (see chapter 4 and Ref. [1, 127]). Therefore, by randomising the proportion of chlorine and bromine atoms in the unit cell, there are two or more possible values of J between adjacent Cu^{2+} ions. Over a whole system of interacting Cu^{2+} ions, it is expected that this will introduce magnetic exchange disorder into the system. This procedure has been used in the studies of bond disordered compounds including the $S = 1/2$ AFM chain

Table 5.1: Relevant structural parameters for $(QuinH)_2CuBr_4{\cdot}2H_2O$ [2] and $(QuinH)_2CuCl_4{\cdot}2H_2O$ [3].

Compound	$(QuinH)_2CuBr_4{\cdot}2H_2O$	$(QuinH)_2CuCl_4{\cdot}2H_2O$
Crystal System	Monoclinic	Monoclinic
Space group	$C2/c$	$C2/c$
a (Å)	12.3323(7)	11.815(2)
b (Å)	9.7972(6)	9.837(2)
c (Å)	18.6504(11)	18.311(4)
Cu-$X1$ (Å)	2.3469(4)	2.2622(18)
Cu-$X2$ (Å)	2.4118(4)	2.2174(11)

$Cu(py)_2(Cl_{1-x}Br_x)_2$, where it was found that an increase in disorder induces a decrease in T_N and the ordered moment m_0, which is the opposite of what is prediction from mean-field chain theory [144]. A Bose glass phase was discovered in the mildly frustrated quantum magnet $(C_4H_{12}N_2)Cu_2(Cl_{1-x}Br_x)_6$ [145–147]. A Bose glass is a gapless spin liquid with a disordered phase at $T = 0$ that is expected to precede the Bose-Einstein condensate phase in an applied field. Pressure was also observed to induce a formation of a Griffiths phase in $(C_4H_{12}N_2)Cu_2(Cl_{1-x}Br_x)_6$ [148]. A Mott glass state precedes the Bose glass at zero-field, and is incompressible (has a vanishing susceptibility at $T = 0$) despite being gapless. The first experimental realisation of a Mott glass was discovered in the $S = 1$ AFM chain $NiCl_{2-2x}Br_{2x} \cdot 4SC(NH_2)_2$ (DTN) [140]. Further studies investigated the Bose glass to Bose-Einstein condensate of magnons transition in DTN [149–151], where an increase in x lowers the spin-gap driving the system closer to a quantum critical point [141].

The combination of pulsed-field magnetisation and μ-SR measurements have been shown to be highly suited at determining the ground state of Cu^{2+} complexes [87, 88, 94–97, 104, 124, 129]. As has been previously mentioned, μ-SR is a local probe adept at detecting the presence of long-range order throughout a sample. Pulsed-field magnetisation on the other hand is a bulk measurement technique that is not necessarily sensitive to long-range order. Critical fields observed in magnetisation data can arise due to significant short range correlations in low-dimensional materials [87, 104]. In the context of bond disorder in quasi-two dimensional antiferromagnets, magnetisation measurements can be used to determine the percolation limit. An absence of an abrupt saturation field would correspond to a totally disordered sample. Pulsed-field magnetisation and μ-SR measurements are therefore ideal techniques to investigate bond disorder in a quasi-two dimensional $S = 1/2$ antiferromagnet.

For this study, the magnetic properties of the quasi two-dimensional coor-

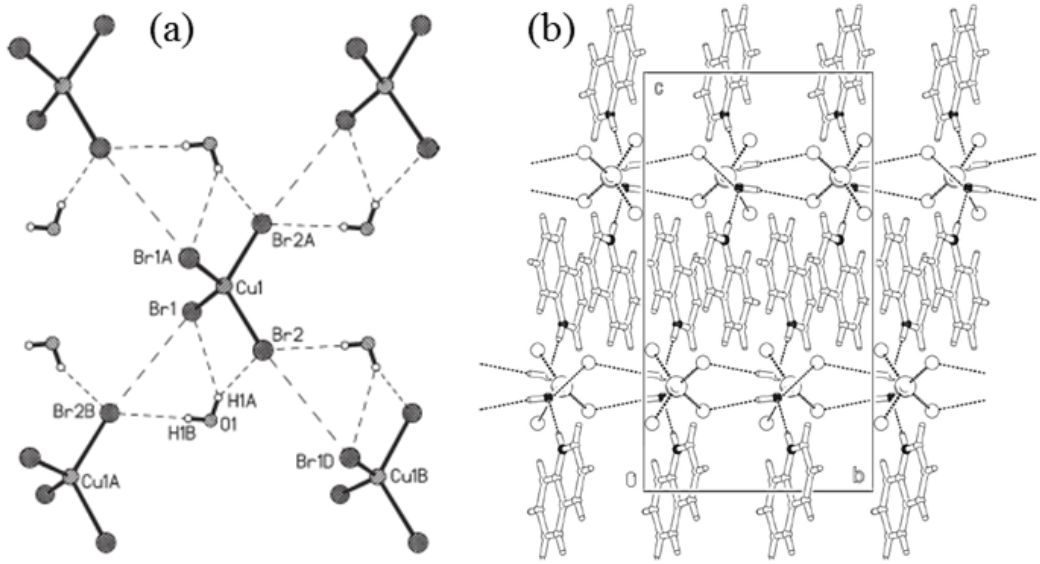

Figure 5.2: **(a)** 87(2) K x-ray structure of $(QuinH)_2CuBr_4{\cdot}2H_2O$ shows the distorted $CuBr_4^{2-}$ tetrahedra layer in the crystal ab plane. Dashed lines illustrate close Br-Br contacts and OH-Br hydrogen bonds. This figure has been taken from Ref. [2]. **(b)** 150(2) K X-ray structure of $(QuinH)_2CuCl_4{\cdot}2H_2O$ showing the view down the a-axis with quinolinium ions ($C_9H_8N^+$) keeping Cu-Cl planes well separated. This figure has been taken from Ref. [3]. The two compounds are isostructural.

dination polymer $(QuinH)_2Cu(Cl_xBr_{1-x})_4{\cdot}2H_2O$ will be characterised. The structures of the parent compounds $(QuinH)_2CuBr_4{\cdot}2H_2O$ and $(QuinH)_2CuCl_4{\cdot}2H_2O$ have been previously determined [2, 3]. The two compounds are isostructural and are made up of layers of CuX_4 (X=Br,Cl) distorted tetrahedra. The CuX_4 tetrahedra are connected via hydrogen bonds to water molecules to form two-dimensional magnetic pathways in the ab plane [Fig. 5.2(a)]. The layers are stacked along the c-axis and kept well separated by the organic (QuinH) cation [Fig. 5.2(b)]. In the crystal growth process, flat platelets of $(QuinH)_2Cu(Cl_xBr_{1-x})_4{\cdot}2H_2O$ grow on top of each other such that the ab plane is parallel to a flat edge. This makes it simple to align the ab plane with the applied field. The structural parameters of both $(QuinH)_2CuBr_4{\cdot}2H_2O$ and $(QuinH)_2CuCl_4{\cdot}2H_2O$ are shown in Table 5.2. Comparing the parameters of the two parent compounds, there are differences of 4% and 0.4% in the distance between Cu^{2+} ions in the a-axis and b-axis respectively. It has also been shown that the size of the bridging halide ion within a superexchange pathway is more important that the distance between adjacent magnetic ions (Chapter 4 and Ref. [1, 127]). Therefore, it is expected that the structural differences between the two parent compounds will have a much smaller effect on the magnetism within

the planes than the composition of the superexchange pathways. The change in the magnetic properties of $(\mathrm{QuinH})_2\mathrm{Cu}(\mathrm{Cl}_x\mathrm{Br}_{1-x})_4{\cdot}2\mathrm{H_2O}$ as the doping (x) increases will likely be due to an increase in magnetic exchange disorder within the Cu^{2+} planes alone.

The magnetic properties of $(\mathrm{QuinH})_2\mathrm{CuBr}_4{\cdot}2\mathrm{H_2O}$ has been characterised, which showed it to be a quasi-two dimensional antiferromagnetic system with $J = 6.17(3)$ K within the Cu-Br-H_2O layers and an average g-factor of $g = 2.15$ [2]. High-field magnetisation measurements also suggest a limit of $T_\mathrm{N} < 1.8$ K, indicating well isolated layers. The structures of $(\mathrm{QuinH})_2\mathrm{CuBr}_4{\cdot}2\mathrm{H_2O}$ and $(\mathrm{QuinH})_2\mathrm{CuCl}_4{\cdot}2\mathrm{H_2O}$ along with the previously mentioned published measurements suggest the Hamiltonian of $(\mathrm{QuinH})_2\mathrm{CuCl}_4{\cdot}2\mathrm{H_2O}$ and $(\mathrm{QuinH})_2\mathrm{CuBr}_4{\cdot}2\mathrm{H_2O}$ can be given by [104]

$$\hat{\mathcal{H}} = J\sum_{\langle i,j\rangle} \hat{\boldsymbol{S}}_i \cdot \hat{\boldsymbol{S}}_j + J_\perp \sum_{\langle i,j'\rangle_\perp} \hat{\boldsymbol{S}}_i \cdot \hat{\boldsymbol{S}}_{j'} + \mu_\mathrm{B}\mu_0 \sum_i \boldsymbol{H}\cdot\boldsymbol{g}\cdot\hat{\boldsymbol{S}}_i, \tag{5.1}$$

where $\langle i,j\rangle$ is the sum over unique exchange bonds and j' indicates an adjacent magnetic site on a neighbouring plane. J is the primary exchange interaction which acts in the xy plane and $J_\perp$ is the interplane interaction in the crystal c (z)-axis. The last term is the Zeeman interaction for spins in an applied magnetic field. Due to the similarity in the structural parameters, it is likely that $(\mathrm{QuinH})_2\mathrm{CuCl}_4{\cdot}2\mathrm{H_2O}$ will exhibit similar Q2D magnetic behaviour to $(\mathrm{QuinH})_2\mathrm{CuBr}_4{\cdot}2\mathrm{H_2O}$. It is also expected that the different x should not affect $J_\perp$ due to the small ($< 2\%$) difference in the distance between Cu^{2+} layers in the parent compounds.

5.2 Methods and preparatory measurements

Energy dispersive x-ray (EDX) measurements of $(\mathrm{QuinH})_2\mathrm{Cu}(\mathrm{Cl}_x\mathrm{Br}_{1-x})_4{\cdot}2\mathrm{H_2O}$ were performed by Fan Xiao using a Bruker TM-1000 scanning electron microscope (SEM) at Clark University, USA. Single crystals were mounted on a piece of carbon conductive tape which was attached to an aluminium sample holder within the spectrometer. The crystals were then exposed to a beam of electrons with energy 15kV for approximately 90 seconds. An incident electron excites an electron from an energy level close to the nucleus. An electron in the outer shell then drops down to the recently vacated level, releasing a photon. This photon has a unique wavelength for different atoms, allowing the determination of not only the composition but the relative abundance of atoms within the sample. For $(\mathrm{QuinH})_2\mathrm{Cu}(\mathrm{Cl}_x\mathrm{Br}_{1-x})_4{\cdot}2\mathrm{H_2O}$ the relative abundance of the halide ions were ex-

tracted. The result of these measurements and a full list of samples prepared are in Table. 5.2. Measurements performed on different crystals of the same batch and different spots on the same single crystal showed no evidence of phase separation, indicating that $(\mathrm{QuinH})_2\mathrm{Cu}(\mathrm{Cl}_x\mathrm{Br}_{1-x})_4{\cdot}2\mathrm{H}_2\mathrm{O}$ is homogeneous. Also included in Table. 5.2 are the measurements made on the different concentrations of $(\mathrm{QuinH})_2\mathrm{Cu}(\mathrm{Cl}_x\mathrm{Br}_{1-x})_4{\cdot}2\mathrm{H}_2\mathrm{O}$. The lowest temperatures measured in the pulsed-field magnetisation and μ-SR measurements, which are presented in this chapter, are also included.

Pulsed-field measurements using the short-pulse 65 T magnet at NHMFL, Los Alamos, USA, were made on small single-crystals with the *ab* plane parallel to the applied field. The field at which the magnetisation of exchanged-coupled spin systems is directly proportional to the strength of the magnetic interactions between ions within the sample [88]. To determine the critical field at which the samples saturate, the down sweep data were interpolated in steps of 0.01 T and smoothed using an adjacent-averaging method with a 20-40 point window. The smoothing was consecutively applied five times. This process eliminates the noise from the data without affecting the physically important features. The data was differentiated once, and then the smoothing method was repeated before a second differentiation to obtain $\mathrm{d}^2M/\mathrm{d}H^2$.

Zero-field μ-SR measurements of polycrystalline $(\mathrm{QuinH})_2\mathrm{CuCl}_4{\cdot}2\mathrm{H}_2\mathrm{O}$ were performed on the HIFI instrument at ISIS, UK. Zero-field μ-SR measurements of polycrystalline samples of $(\mathrm{QuinH})_2\mathrm{Cu}(\mathrm{Cl}_x\mathrm{Br}_{1-x})_4{\cdot}2\mathrm{H}_2\mathrm{O}$ (x = 0, 0.01, 0.09, 0.23, 0.25 and 0.41) were made and analysed at PSI, Switzerland by Fan Xiao and Tom Lancaster. In both cases, the samples were mounted onto a silver backing plate inside the cryostat using Apiezon vacuum grease.

Table 5.2: List of concentrations of $(QuinH)_2Cu(Cl_xBr_{1-x})_4{\cdot}2H_2O$ prepared, and for which measurements were performed. For the pulsed-field magnetisation and μ-SR techniques, the temperature of the data presented in section 5.3 is stated. The temperatures in red indicate measurements that were performed at PSI and analysed by Fan Xiao.

Concentration	Pulsed-Field	μ-SR
0	0.56 K	0.112 K
0.01	0.67 K	0.02 K
0.02	0.59 K	
0.04	0.60 K	
0.05	0.58 K	
0.09	0.64 K	0.02 K
0.09	0.58 K	
0.14	0.59 K	
0.17	0.47 K	
0.23	0.59 K	0.02 K
0.25	0.60 K	0.02 K
0.41	0.57 K	0.02 K
0.57	0.52 K	
0.605	0.59 K	
0.74	0.46 K	
0.835	0.65 K	
0.84	0.65 K	
0.95	0.59 K	
0.96	0.69 K	
1	0.69 K	0.1 K

5.3 Results and discussion

5.3.1 Parent compounds

Magnetisation

Pulsed-field magnetisation measurements of single crystals of $(QuinH)_2CuBr_4{\cdot}2H_2O$ [Fig. 5.3(a)] show a concave rise to saturation, indicative of low-dimensional behaviour [123]. The saturation field reflects the size of the magnetic interactions in the sample. As discussed in Section 2.1, the critical field H_C is found from the position of the trough in d^2M/dH^2. For $(QuinH)_2CuBr_4{\cdot}2H_2O$ this occurs at $\mu_0 H_c =$ 16.8(5) T [Fig. 5.3(b)]. This is directly proportional to the strength of the Q2D magnetic interactions in the sample via the formula

$$nJ = g\mu_B\mu_0 H_C, \tag{5.2}$$

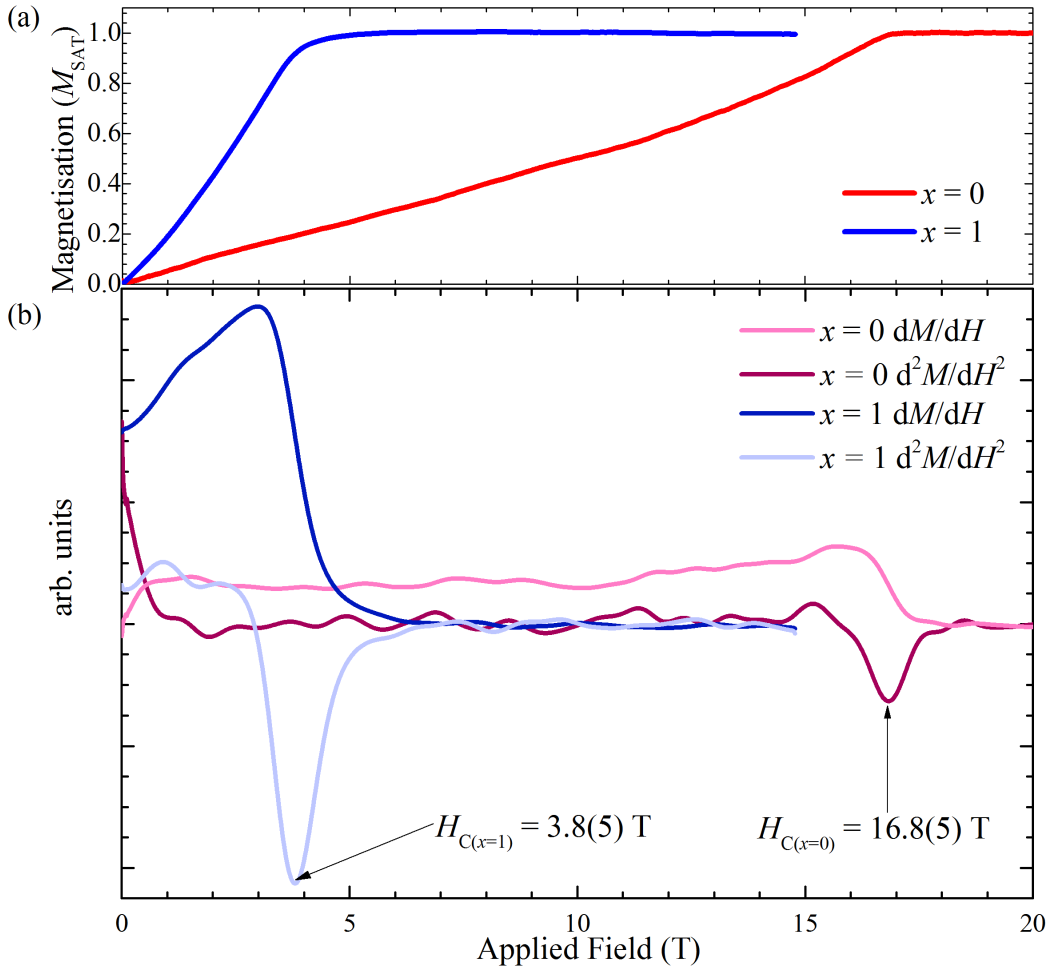

Figure 5.3: **(a)** Pulsed-field magnetisation measurements of $(QuinH)_2CuBr_4{\cdot}2H_2O$ (red) and $(QuinH)_2CuCl_4{\cdot}2H_2O$ (blue). The data presented here is from the down sweep of the magnetic field. **(b)** Differential susceptibility and gradient of differential susceptibility of $(QuinH)_2CuBr_4{\cdot}2H_2O$ (pink and maroon) and $(QuinH)_2CuCl_4{\cdot}2H_2O$ (dark blue and light blue). See table. 5.2 for the temperature.

where $n = 4$ is the number of exchange pathways with magnitude J and $J \gg J_\perp$ [88]. The previously published g-factor of $g = 2.15$ is used. Using Eq. 5.2, it was found that $J = 6.1(2)$ K for $(QuinH)_2CuBr_4{\cdot}2H_2O$, consistent with the previously reported measurements [2]. Pulsed-field measurements of $(QuinH)_2CuCl_4{\cdot}2H_2O$ show a much more rounded rise to saturation [Fig. 5.3(a)]. The critical field was found to be $\mu_0 H_C = 3.8(5)$ T [Fig. 5.3(b)]. Using Eq. 5.2, this yields $J = 1.4(2)$ K. As the g-factor for $(QuinH)_2CuCl_4{\cdot}2H_2O$ is unknown, the powder averaged value of $g = 2.15$ was used in this calculation due to the structural sim-

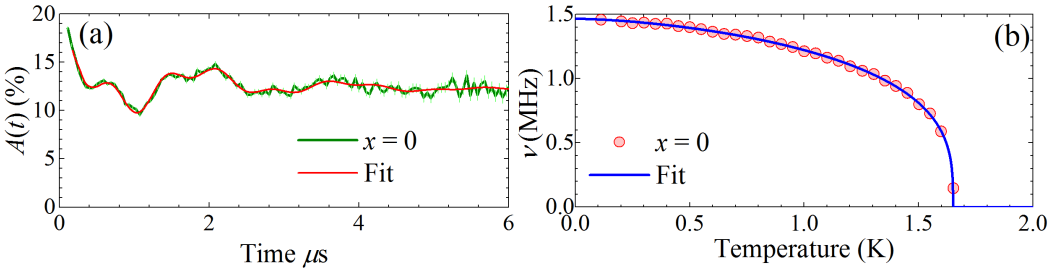

Figure 5.4: **(a)** The 0.112 K μ-SR asymmetry spectra of $(QuinH)_2CuBr_4{\cdot}2H_2O$ and **(b)** temperature dependence of the highest frequency oscillation from **(a)**.

ilarity with $(QuinH)_2CuBr_4{\cdot}2H_2O$ and other quasi-two dimensional Cu^{2+} materials. The magnitude of J found for $(QuinH)_2CuCl_4{\cdot}2H_2O$ is lower than that of $(QuinH)_2CuBr_4{\cdot}2H_2O$, which is expected due to the halide substitution [1]. Also, $J_{Br} = 4J_{Cl}$ within errors, which is in excellent agreement with previous measurements [127]. As there is no published g-factor for $(QuinH)_2CuCl_4{\cdot}2H_2O$, a magnitude of $g = 2.15$ will be used for all values of x.

μ-SR

Zero-field μ-SR spectra of polycrystalline $(QuinH)_2CuBr_4{\cdot}2H_2O$ were measured at PSI, Switzerland, and analysed by Fan Xiao. The 0.112 K asymmetry $[A(t)]$ displayed oscillations, which shows the presence of long-range order in $(QuinH)_2CuBr_4{\cdot}2H_2O$. The data was found to be well modelled with three oscillating frequencies [Fig. 5.4(a)] and fitted to:

$$A(t) = \sum_{i=1}^{3} A_i e^{-\lambda_i t} \cos\left(2\pi\nu_i t + \phi_i\right) + A_{bg} e^{-\lambda_{bg} t}, \tag{5.3}$$

where there are $i = 3$ oscillatory components with frequency ν_i and phase ϕ_i, and a relaxing background with amplitude A_{bg}. The temperature dependence of the oscillatory component with the highest frequency was used to find T_N [Fig. 5.4(b)] using

$$\nu_i\left(T\right) = \nu_i\left(0\right)\left[1 - \left(\frac{T}{T_N}\right)^{\beta}\right]^{\alpha}. \tag{5.4}$$

The transition to long-range order was found to be at $T_N = 1.65(1)$ K, consistent with the previously published limits.

Zero-field polycrystalline measurements of $(QuinH)_2CuCl_4{\cdot}2H_2O$ collected at 1.8 K continuously relaxes and shows no sign of oscillatory behaviour [Fig. 5.5(a) - green line]. Therefore, the data was fitted to the Kubo-Toyabe model [119];

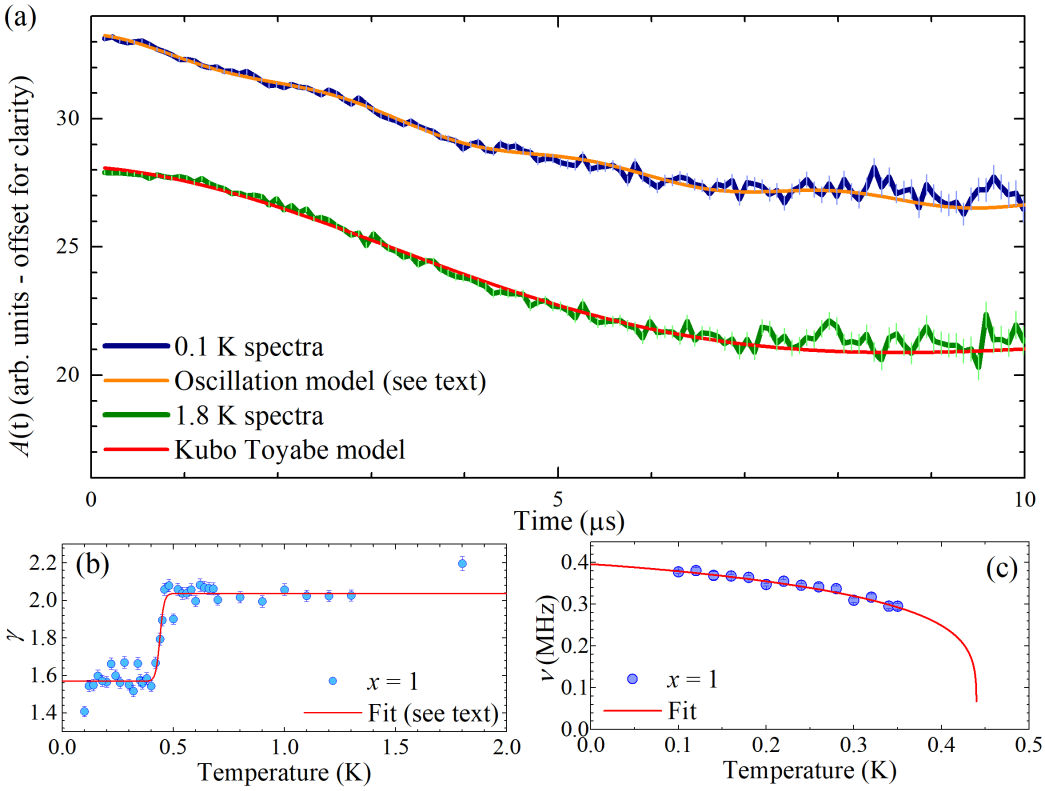

Figure 5.5: **(a)** Time evolution of the asymmetry at 0.1 K (blue line) and 1.8 K (green line). The light blue and light green lines indicate the errors in the data. The orange line is a fit of the 0.1 K data to Eq. 5.8 and the red line is a fit of the 1.8 K data to Eq. 5.5. **(b)** Temperature dependence of γ. The red line is a fit to Eq. 5.6. **(c)** Temperature dependence of ν. The red line is a fit to Eq. 5.9

$$A(t) = A_0 + A(0)\left(\frac{1}{3} + \frac{2}{3}e^{-\Delta^2 t^2/2}\left(1 - \Delta^2 t^2\right)\right)e^{-\lambda t}, \tag{5.5}$$

where A_0 is the background asymmetry and $A(0)$ is the relaxing asymmetry. An exponential decay term is included to account for fluctuations that are too fast for the muons to interact with, which squashes the dip in the Kubo-Toyabe model. Δ and λ were left free to vary and the best fit was achieved with $A_0 = 20.69(5)$ %, $A(0) = 7.44(5)$ %, $\Delta = 0.201(3)$ and $\lambda = 0.036(4)$. This model gives a reasonable description of the data.

As the temperature is lowered, the Kubo-Toyabe model becomes increasingly less representative of the data. Therefore, measurements at all temperatures were fitted to the following stretched exponential model

$$A(t) = A_0 + A(0)e^{-(\lambda t)^{\gamma}}, \tag{5.6}$$

with all parameters free to vary. Though a stretched exponential has little physical meaning, it was found to be the only model to be in agreement with the data throughout the whole temperature range. The reason for this is unknown. A plot of the parameter γ varying with temperature is shown in Fig. 5.5(b) and shows a clear change in behaviour at $T \approx 0.45$ K. This is a result of the muons being insensitive to fluctuations that occur in electronic times scales for $T > T_{\rm N}$, but are relaxed by these on cooling below $T_{\rm N}$ [87]. This indicates a transition to a magnetically ordered state, and was modelled using a Fermi function type transition between two amplitudes γ_1 and γ_2

$$\gamma = \gamma_2 + \frac{\gamma_1 - \gamma_2}{\mathrm{e}^{(T-T_{\rm N})/\omega} + 1}, \tag{5.7}$$

where $\gamma_1 < \gamma_2$ and ω is the width of the transition. The critical temperature $T_{\rm N} = 0.44(1)$ is extracted. The width of the transition is taken to be the error in $T_{\rm N}$. A comparison of the asymmetry between measurements taken at 0.44 and 0.45 K shows a change in the shape of the relaxation, consistent with a transition to a state of long-range order.

In the ordered regime, the data shows one damped, weakly oscillating frequency in $A(t)$ [Fig. 5.5(a)]. The damping of the oscillations in Fig. 5.5(a) are caused by muons settling into sites in the sample that have slightly different values for the internal magnetic field. The precession of muons therefore dephase from each other, damping the oscillations in $A(t)$. Therefore, each run was therefore found to be best modelled using

$$A(t) = A_0 + A(0)\left[p_1 e^{-(\lambda_1 t)} cos\left(2\pi\nu t\right) + p_2 e^{-(\lambda_2 t)^{\gamma_2}}\right], \tag{5.8}$$

where ν_1 is the frequency of the oscillation, p_1 is the proportion of muons that sit at sites where they will oscillate and p_2 is the proportion of muons that sit at sites with no oscillations. When fitting the 0.1 K data, all parameters were left to vary freely. For all subsequent runs, A_0 and $A(0)$ were left fixed. The amplitude of oscillations was found to be very small with $p_1 \approx 2\%$, similar to $[\mathrm{Cu(4\text{-}phpyO)_2(pyz)_2}](\mathrm{ClO_4})_2$ [104] and the $[\mathrm{Cu(pyz)_2(pyO)_2}]Y_2$ ($Y = \mathrm{BF_4}$, $\mathrm{PF_6}$) family [104, 118]. λ_1 was found to vary between orders of 0.01 and 0.1, which suggests that the damping is light and the distribution in the local magnetic field is small at this muon site [95]. The other parameters remain relatively constant around $\lambda_2 \approx 0.2$ and $\gamma_2 \approx 1.6$. The resultant temperature dependence of the frequency is plotted in Fig. 5.5(c) and

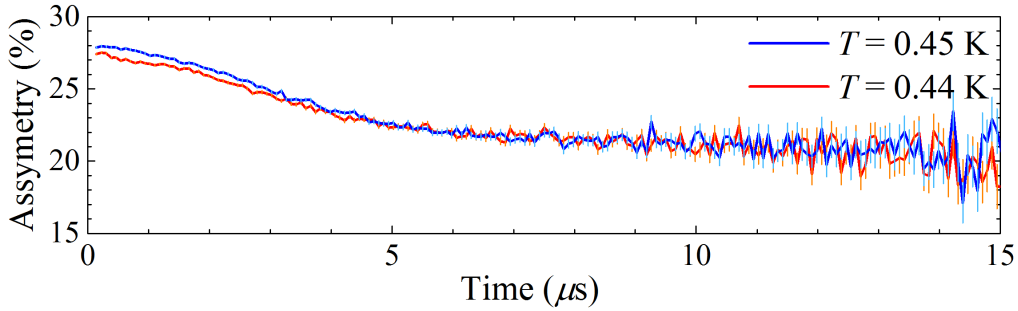

Figure 5.6: Comparison of the time evolution of the asymmetry at 0.44 K (red line) and 0.45 K (blue line). The light blue and orange lines indicates the errors in the 0.44 K and 0.45 K data respectively.

shows a shallow downward curve from low temperature towards T_c. This was fitted to the phenomenological function

$$\nu = \nu(0)\left[1 - \left(\frac{T}{T_{\mathrm{N}}}\right)^{\alpha}\right]^{\beta}. \tag{5.9}$$

For $T > 0.36$ K, the amplitude of the oscillations become too small too be observable. There aren't enough points close to the critical region to achieve an accurate T_{N} in Fig. 5.5(c). Therefore value of T_{N} was set to the previously obtained value of 0.44 K. The other parameters extracted from Eq. 5.9 were $\nu(0) = 0.4(2)$ MHz, which indicates the magnitude of the magnetic field at at the oscillating muon site, $\alpha = 1.1(6)$ and $\beta = 0.20(5)$. For $(\mathrm{QuinH})_2\mathrm{CuCl}_4{\cdot}2\mathrm{H}_2\mathrm{O}$, $\nu(0)$ is a similar order of magnitude to frequencies observed in many similar copper systems. These systems usually have more than one oscillation frequency however. For $(\mathrm{QuinH})_2\mathrm{CuCl}_4{\cdot}2\mathrm{H}_2\mathrm{O}$, it may be the case that muons do not stop at the sites that have the higher frequencies or that these frequencies have negligible amplitudes [118, 125]. β describes the behaviour around T_{N} and is used to make inferences about the magnetic dimensionality. For $(\mathrm{QuinH})_2\mathrm{CuCl}_4{\cdot}2\mathrm{H}_2\mathrm{O}$ this value is typical of low-dimensionality [118]. However, due to the lack of data points in this region, this parameter has a low dependency in the fitting of the model.

The Yasuda relationship relates J and $J_\perp$ to the ordering temperature T_{N} of $S = 1/2$ Q2D systems [102]:

$$\frac{T_{\mathrm{N}}}{J} = \frac{2.30}{2.43 - \ln\left|\frac{J_\perp}{J}\right|}, \tag{5.10}$$

and is precise to one order of magnitude. Using the values of J and T_{N} ex-

tracted from pulsed-field and μ-SR measurements, the strength of interplane magnetic interactions are found to be $J_\perp = 0.014(5)$ K for $(\mathrm{QuinH})_2\mathrm{CuBr}_4{\cdot}2\mathrm{H}_2\mathrm{O}$ and $J_\perp = 0.011(8)$ K for $(\mathrm{QuinH})_2\mathrm{CuCl}_4{\cdot}2\mathrm{H}_2\mathrm{O}$. These values of $J_\perp$ are the same within the errors. Therefore, substitution of the halide atoms has a vanishingly small effect on the strength of $J_\perp$ and any deviation from Eq. 5.10 on changing x is due to exchange disorder in the Cu^{2+} planes.

5.3.2 Disordered compounds

Magnetisation

The low-temperature ($T \approx 0.6$ K) pulsed-field magnetisation measurements of single-crystals of $(\mathrm{QuinH})_2\mathrm{Cu}(\mathrm{Cl}_x\mathrm{Br}_{1-x})_4{\cdot}2\mathrm{H}_2\mathrm{O}$ for all concentrations are shown in Fig. 5.7. For x close to zero there is the concave rise to saturation indicative of low-dimensional antiferromagnetism [Fig. 5.7(a)]. As the concentration (x) increases above $x = 0.05$, the magnetisation becomes less concave. The saturation point decreases slightly in field and becomes much more rounded. A small hump also develops at low fields. Whilst this could be due to the saturation of Cu^{2+} ions within Cl-rich regions in the samples, EDX measurements suggest that this is not the case. The cause of this hump is therefore unknown. As the concentration approaches 0.6, the magnetisation becomes very rounded, such that the saturation field becomes very broad [Fig. 5.7(a),(b)]. For $x = 0.74$ and $x = 0.835$, there is no unambiguous saturation feature in the expected region $0 \leq \mu_0 H \leq 5$ T in the $\mathrm{d}^2M/\mathrm{d}H^2$ data based on the $x = 0.605$ and $x = 0.84$ measurements (Fig. 5.8). There is an observable saturation field for $x = 0.84$ and above [Fig. 5.7(c)]. As the concentration approaches $x = 1$ the data becomes more concave, consistent with the return to low-dimensional antiferromagnetism in $(\mathrm{QuinH})_2\mathrm{CuCl}_4{\cdot}2\mathrm{H}_2\mathrm{O}$.

The critical fields obtained from pulsed-field magnetisation measurements of the disordered samples are summarised in Fig. 5.9. They show a slow decrease in the critical field from $H_\mathrm{C} = 16.8(5)$ T at $x = 0$, until $x = 0.41$ at which there appears to be a sharper drop towards zero around $x = 0.61$. The $x \leq 0.605$ data was fitted to the following phenomenological model

$$H_\mathrm{C}(x) = H_\mathrm{C}(0)\left[1 - \left(\frac{x}{x_\mathrm{C}}\right)^n\right]^m. \tag{5.11}$$

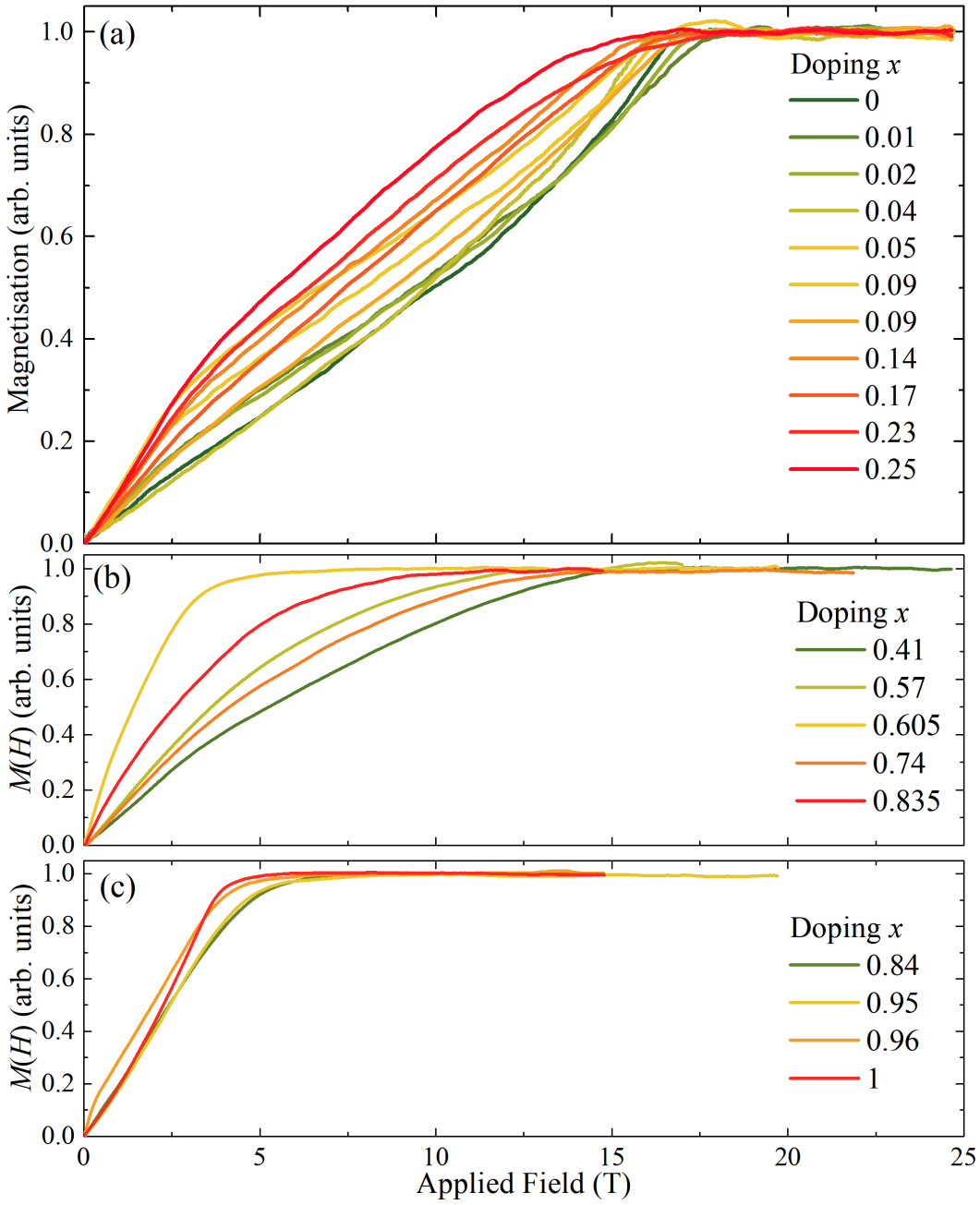

Figure 5.7: Low-temperature pulsed-field magnetisation data of $(\mathrm{QuinH})_2\mathrm{Cu}(\mathrm{Cl}_x\mathrm{Br}_{1-x})_4{\cdot}2\mathrm{H}_2\mathrm{O}$ taken in decreasing fields for **(a)** $x \leq 0.25$, **(b)** $0.41 \leq x \leq 0.835$ and **(c)** $0.84 \leq x$. See table. 5.2 for the temperature that each measurement was taken at.

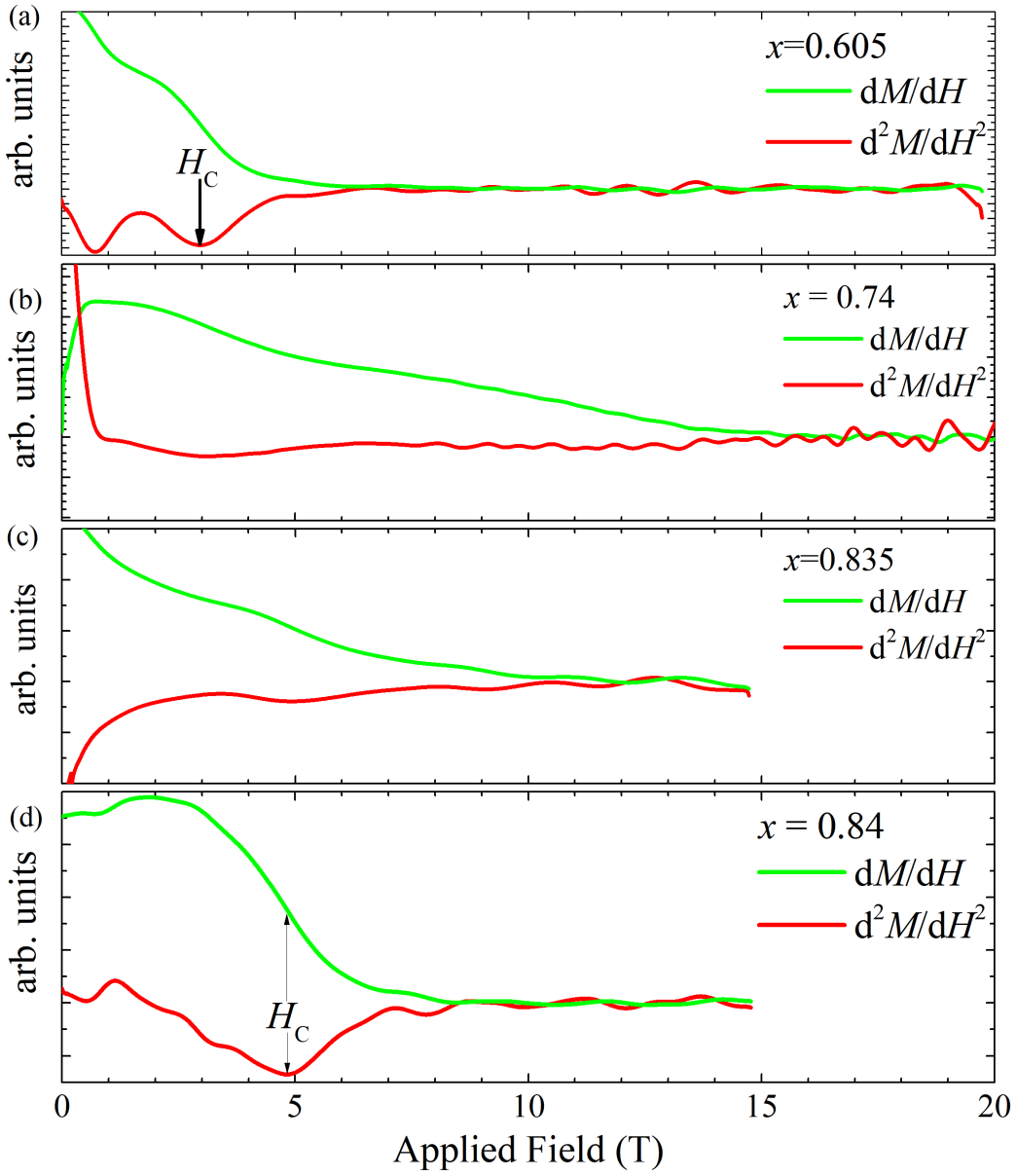

Figure 5.8: Down sweep $\mathrm{d}M/\mathrm{d}H$ and $\mathrm{d}^2\mathrm{M}/\mathrm{d}H^2$ data for $(\mathrm{QuinH})_2\mathrm{Cu}(\mathrm{Cl}_x\mathrm{Br}_{1-x})_4{\cdot}2\mathrm{H}_2\mathrm{O}$ with **(a)** $x = 0.605$, **(b)** $x = 0.74$, **(c)** $x = 0.835$ and **(d)** $x = 0.84$. The lack of a critical field H_C in the $x = 0.74$ and $x = 0.835$ data is indicative of a disordered phase in these samples.

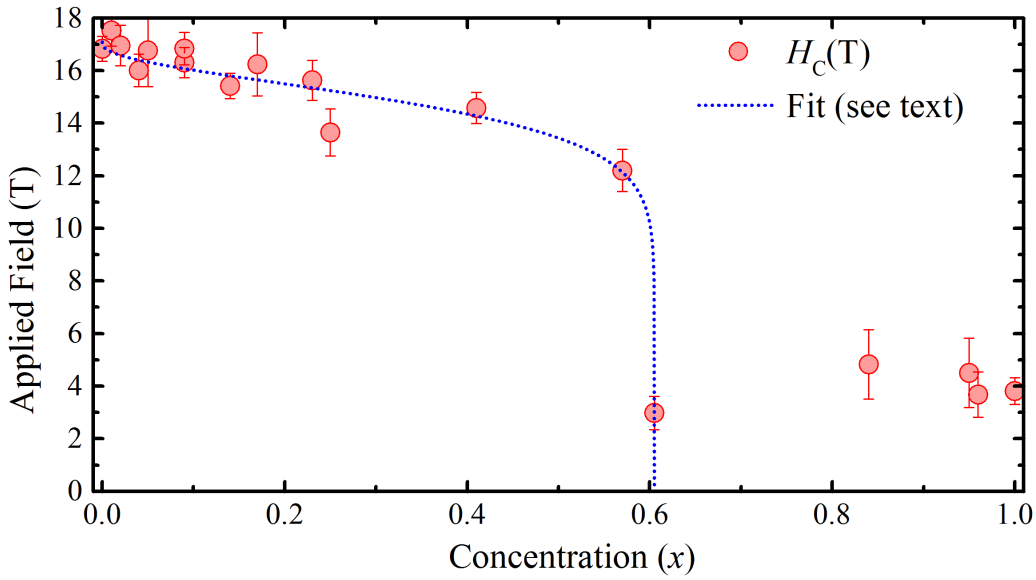

Figure 5.9: Phase diagram showing the critical fields in pulsed-field magnetisation measurements for different concentrations x.

The fit (blue line in Fig. 5.9) yields $x_C = 0.605(1)$ with exponents $n = 0.43(26)$ and $m = 0.095(24)$. As mentioned previously, there is no apparent saturation point in the region $0.605 < x < 0.84$. At $x = 0.84$, a sharp feature in the data at the saturation point reappears. As magnetisation measurements indicated the presence of short range correlations, this suggests that there is a disordered region is in the region $0.605 < x < 0.84$.

It appears that there are two separate regimes either side of this region of disorder. The left hand side is dominated by interactions via Cu-Br-Cu pathways, whereas the right-hand side is dominated by Cu-Cl-Cu routes. Within each regime it is assumed that an increase in the broadness of the saturation point is due to an increase in the disorder of the Q2D system. The error bars are determined from the full width at half-maximum of the trough in $\mathrm{d}^2M/\mathrm{d}H^2$ and is an indication of how sharp the saturation point is. Bigger errors correspond to a broader saturation point. It seems that as $(\mathrm{QuinH})_2\mathrm{Cu}(\mathrm{Cl}_x\mathrm{Br}_{1-x})_4{\cdot}2\mathrm{H}_2\mathrm{O}$ becomes more disordered, the broadness of the saturation point increases.

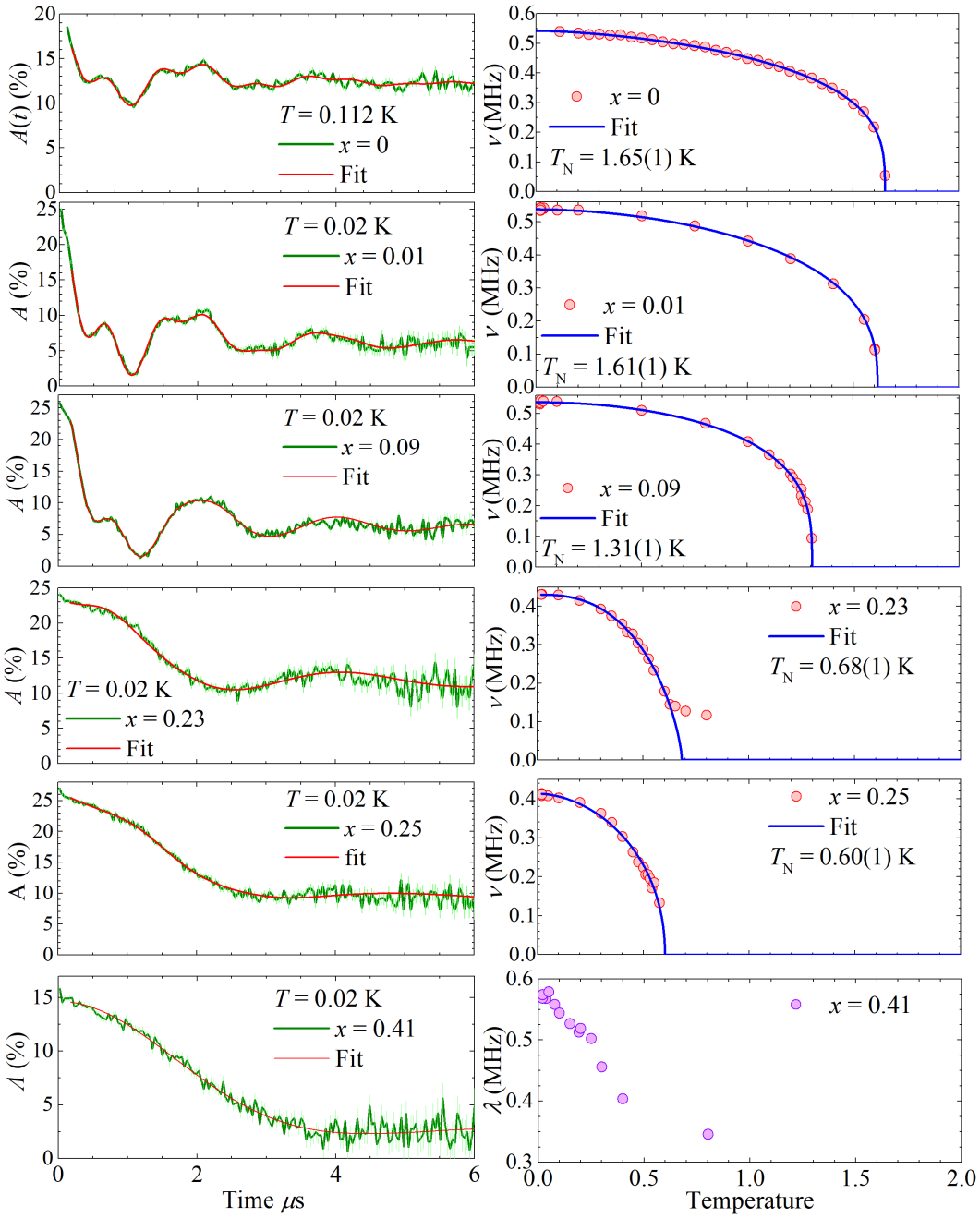

Figure 5.10: Left column: the lowest temperature μ-SR asymmetry spectra of $(QuinH)_2Cu(Cl_xBr_{1-x})_4{\cdot}2H_2O$. From top to bottom is $(QuinH)_2CuBr_4{\cdot}2H_2O$ (added for comparison) and then $x = 0.01$, 0.09. 0.23, 0.25, 0.41. Right column: temperature dependence of the highest frequency oscillation from the left column.

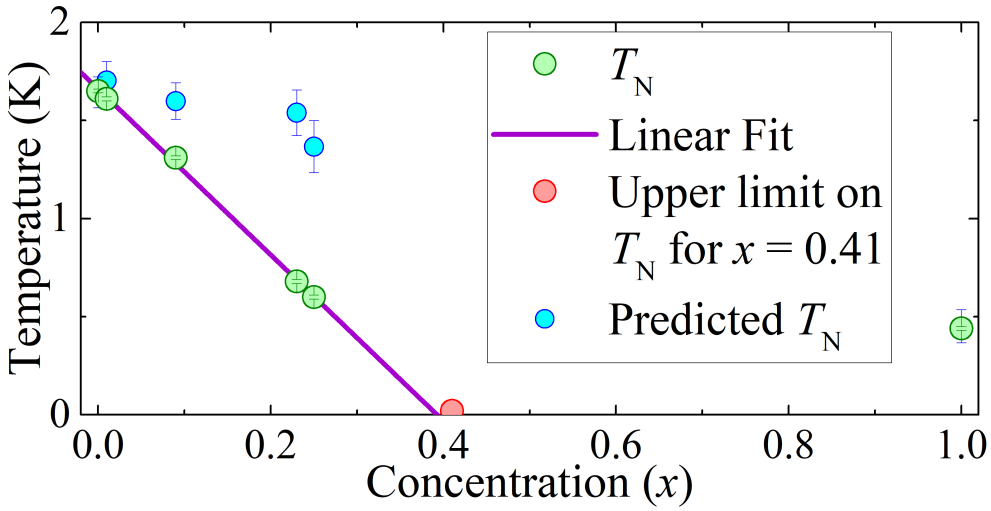

Figure 5.11: Ordering temperature of $(QuinH)_2Cu(Cl_xBr_{1-x})_4{\cdot}2H_2O$ as a function of x (green dots). The $x \leq 0.25$ data points have been fitted to a linear model with $x_{C1} = 0.39$ (green line). Also included are the predicted ordering temperatures for $(QuinH)_2Cu(Cl_xBr_{1-x})_4{\cdot}2H_2O$ using the values of J obtained from magnetisation measurements, and assuming that $J_\perp$ is constant and Eq. 5.10 holds for all x

μ-SR

Low-temperature μ-SR spectra of polycrystalline $(QuinH)_2Cu(Cl_xBr_{1-x})_4{\cdot}2H_2O$ (x=0.01, 0.09, 0.23, 0.25 and 0.41) were measured at PSI and analysed by Fan Xiao (University of Bern) and are shown in the left column of Fig. 5.10. The data displays oscillations with two ($x = 0.23, 0.25$) or three ($x = 0.01, 0.09$) different frequencies. The asymmetry data was fitted to Fig. 5.3. The temperature dependence (right column of Fig. 5.10) of the oscillation with the highest frequency for each sample was fitted to Eq. 5.4. This yields ordering temperatures of 1.61(1), 1.31(1), 0.68(1) and 0.60(1) K for x=0.01, 0.09, 0.23 and 0.25 respectively. There is no discernible evidence of oscillations indicating the presence of long-range order for $x = 0.41$. The $x = 0.41$ data at all temperatures was fitted to Eq. 5.6 and no sudden change in the behaviour of λ_1 (Fig. 5.10) was observed, suggesting that there is no long-range order for $x = 0.41$ at $T > 0.02$ K.

The concentration dependence of T_N is plotted in Fig. 5.11 and shows a linear drop with no LRO predicted for $x \geq 0.39$, consistent with the upper bound on T_N for $x = 0.41$. This is at odds with the results from the magnetisation measurements which gives $x_C = 0.605$. One interpretation of this disparity is that disorder destroys the LRO in the region $0.39 < x < 0.61$, but there are still short range correlations present. Also included in Fig. 5.11 are the ordering temperatures assuming that

$J_\perp$ is constant and Eq. 5.10 holds for all x. It is clear that the actual ordering temperature is less than the predicted data. This suggests that long-range ordering is being suppressed for $x \neq 0, 1$. This will be discussed further in the next section.

5.4 Summary

The effect of magnetic exchange disorder in Q2D antiferromagnets has been investigated using pulsed-field magnetisation and μ-SR measurements. A proposed phase diagram is shown in Fig. 5.12. For small amounts of disorder, there is little change in the effective exchange strength. As x approaches 0.6 from below, there is a much sharper drop and J appears to go to zero in the region $0.605 \leq x \leq 0.74$. However, there is a much faster decrease in the ordering temperature for low x values with no apparent long-range order for $x = 0.41$. For high x, short correlations persist as low as $x = 0.84$, and there is long-range order below $T_\mathrm{N} = 0.44(1)$ K for $x = 1$. Further measurements are required to accurately map out this side of the phase diagram. The parameters of samples with known ordering temperatures are summarised in Table. 5.3. If Eq. 5.10 holds for all values of x, there is a substantial decrease in $J_\perp$ for $x < 0.41$. It has been shown that there is practically no change in $J_\perp$ between $(\mathrm{QuinH})_2\mathrm{CuBr}_4{\cdot}2\mathrm{H}_2\mathrm{O}$ and $(\mathrm{QuinH})_2\mathrm{CuCl}_4{\cdot}2\mathrm{H}_2\mathrm{O}$. This suggests that the decrease in T_N is not solely driven by a difference in dimensionality but by the enhancement of quantum fluctuations as x increases.

The concentration at which long range order seems to disappear for any observable temperature is at $x_{\mathrm{C}1} = 0.39\,(1)$. However, a critical field continues to be observed in magnetometry measurements up to $x_{\mathrm{C}2} = 0.61\,(1)$. Bulk magnetometry is not a good indicator of LRO and critical fields can arise from short-range correlations in low-dimensional materials. The region $0.605 < x < 0.84$ appears to be totally disordered due to the absence of any critical field in the $x = 0.74$, 0.835 magnetisation data and the absence of long-range order for $0.41 < x < 1$. If $J \to 0$, this suggests a decoupling of the magnetic transition ($x_{\mathrm{C}1}$) and the percolation transition ($x_{\mathrm{C}2}$). In this case, the model published by R. Yu *et al.* is consistent with the data. The presence of two competing magnetic pathways with different strengths between Cu^{2+} ions is likely to lead to inhomogeneity within the sample. This could give rise to segments of ladders at the Br-rich end of the spectrum which are linked via Cu-Cl-Cu pathways and the local formation of Cu-Br-Cu dimers at the Cl-rich end of the spectrum. These locally fluctuating states enhance quantum fluctuations, which would destroy long-range order within the sample. The region $0.61 < x < 0.84$ could be a quantum disordered phase and $0.39 < x < 0.61$ may be

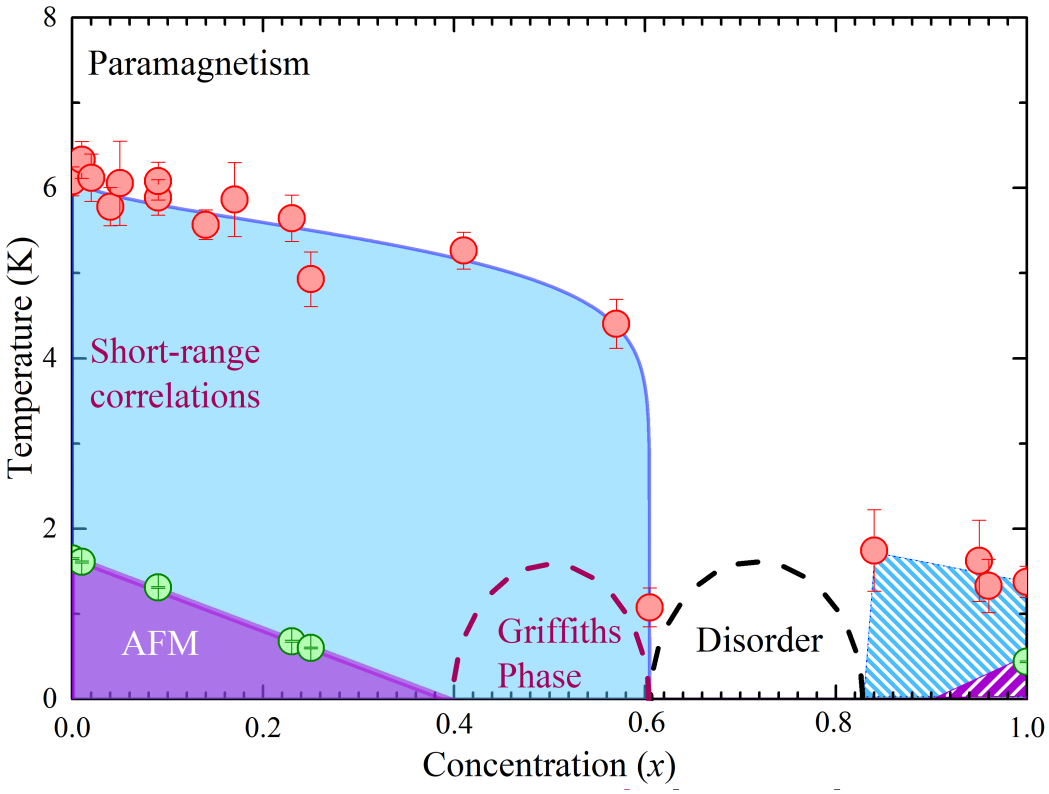

Figure 5.12: Proposed phase diagram of $(\mathrm{QuinH})_2\mathrm{Cu}(\mathrm{Cl}_x\mathrm{Br}_{1-x})_4{\cdot}2\mathrm{H}_2\mathrm{O}$. The phase boundaries are estimates suggested by the experimental data (see text). As x increases from zero, $(\mathrm{QuinH})_2\mathrm{Cu}(\mathrm{Cl}_x\mathrm{Br}_{1-x})_4{\cdot}2\mathrm{H}_2\mathrm{O}$ remains in an antiferromagnetically ordered state at $T = 0$ until quantum fluctuations destroy long-range order at $x_{\mathrm{C1}} = 0.39$. $(\mathrm{QuinH})_2\mathrm{Cu}(\mathrm{Cl}_x\mathrm{Br}_{1-x})_4{\cdot}2\mathrm{H}_2\mathrm{O}$ then enters a quantum Griffiths phase with large magnetically ordered regions. At $x_{\mathrm{C2}} = 0.61$, $(\mathrm{QuinH})_2\mathrm{Cu}(\mathrm{Cl}_x\mathrm{Br}_{1-x})_4{\cdot}2\mathrm{H}_2\mathrm{O}$ becomes fully disordered with no evidence of short range correlations. A sharp saturation point re-emerges at $x = 0.84$ and there is long range order at $T = 0$ for $(\mathrm{QuinH})_2\mathrm{CuCl}_4{\cdot}2\mathrm{H}_2\mathrm{O}$. For $x > 0.8$, patterned regions correspond to estimated regions mirroring the low-x end of the spectrum, with more experiments required to map out the phase boundaries at high-x.

an experimental realisation of a quantum Griffiths phase [109]. The absence of long-range order but the presence of a critical field indicating short-range correlations does suggest the formation of large magnetically ordered regions within the global paramagnetic phase ($T > T_{\mathrm{N}}$). This phase has been reported in antiferromagnets previously in the site diluted $\mathrm{Fe}_{1-x}\mathrm{Zn}_x\mathrm{F}_2$ [152], the geometrically frustrated $\mathrm{DyBaCo}_4\mathrm{O}_{7+\delta}$ [143] and is reported to be induced by pressure in $(\mathrm{C}_4\mathrm{H}_{12}\mathrm{N}_2)\mathrm{Cu}_2(\mathrm{Cl}_{1-x}\mathrm{Br}_x)_6$[148]. Therefore, $(\mathrm{QuinH})_2\mathrm{Cu}(\mathrm{Cl}_x\mathrm{Br}_{1-x})_4{\cdot}2\mathrm{H}_2\mathrm{O}$ presents an excellent opportunity to further study this novel phase in a bond disor-

Table 5.3: Table showing parameters extracted from pulsed-field (J) and μ-SR (T_{N}) measurements.

x	0	0.01	0.09	0.23	0.25	1
J (K)	6.1(2)	6.3(2)	5.9(2)	5.6(3)	5.0(3)	1.4(2)
T_{N} (K)	1.65(1)	1.61(1)	1.31(1)	0.68(1)	0.60(1)	0.44(1)

dered antiferromagnet.

However, it is possible that there is a smooth, continuous transition between the J_{Br} and J_{Cl} dominant regimes within the "disordered" region. More measurements are required to accurately determine whether this region is truly disordered. Also required are further μ-SR measurements to explore the behaviour of T_{N} in the region $0.84 \leq x < 1$. Future investigations can also make further use of the varied magnetic behaviour of the halide ions in superexchange pathways studied in Chapter 2. For example, $(\mathrm{QuinH})_2\mathrm{Cu}(\mathrm{F}_x\mathrm{I}_{1-x})_4{\cdot}2\mathrm{H_2O}$ could be a more effective realisation of bond dilution due to the predicted large difference in the two exchange strengths ($J_I \gg J_F$).

Chapter 6

Conclusion

Low-dimensional antiferromagnets have long been studied by condensed matter physicists, predominantly with the aim of verifying various theoretical predictions. There are significant challenges in trying to apply these systems to real world situations. Magnetism on a microscopic level is still not fully understood, and attempts to produce bespoke magnetic system do not succeed regularly. This is partly due to complex ground states for $S \geq 1$ antiferromagnets, which make them more difficult to characterise, and the lack of single crystals sufficiently large enough to make measurements on. In this thesis, I have presented a methodology for characterising the magnetic properties of low-dimensional anisotropic Ni^{2+} complexes in powdered form. This uses readily available magnetometry and heat capacity techniques and was largely successful and could be applied more widely to related systems enabling swift characterisation of new materials and improved feedback on structure/property relationships to chemists growing new examples of low-dimensional magnets. A decision on whether further studies making use of more difficult and costly measurements and/or single-crystal growth can then be made. During these measurements a trend has emerged linking the arrangement of the local Ni^{2+} octahedral environment and the sign and size of D, while further measurements would be desirable to confirm this tendency, it could be used by sample growers to engineer materials with specific single-ion properties. The NiI_2(3,5-lut)$_4$ system is ideal for in-depth measurements of the excitations and critical properties of ideal Haldane chains, which have not been possible previously due to high critical fields and/or large anisotropy. The work on (QuinH)$_2$Cu(Cl$_x$Br$_{1-x}$)$_4$·2H$_2$O is the first such study of bond-disordered two-dimensional quasi-Heisenberg antiferromagnets and is suggestive of an exotic disordered phase.

Magnetisation measurements are highly effective at determining whether

single-ion anisotropy and/or magnetic exchange is the dominant term in the Hamiltonian of a low-dimensional spin-1 quantum magnet. The shape of the differential susceptibility is different for $|D| \gg J$, $D \sim J$ and $|D| \ll J$. The former case exhibits a smooth drop, with a weak hump if $|D| > 0$ at $g\mu_{\mathrm{B}}\mu_0 H_{\mathrm{C}} = \sqrt{D^2 - E^2}$. For $|D| \sim J$ there is at least one sharp feature indicating a critical field and a less rounded saturation point than for $|D| \gg J$. For $|D| \ll J$, there is only one sharp feature which occurs at saturation.

In a system of ions where the single-ion anisotropy term is dominant, modelling susceptibility measurements gives an accurate value of the magnitude and sign of D and E can be obtained. Heat capacity measurements are also able to accurately measure the size and sign of D and E in isolated systems using Eq. 3.5 and Eq. 2.1. For the case $D \sim J$ the analysis is more complicated. Low-temperature magnetisation measurements may indicate a sample is easy-axis by the presence of a spin-flop or spin-flip. Accurate values of D and J can be calculated from the positions of critical fields described in section. 2.3. Heat capacity measurements are highly suited to observing the transition to long-range order. This can be used to help map out the phase diagram of these compounds. However, the lambda peak can also mask the Schottky anomaly, and therefore cannot not be relied on to model single-ion anisotropy in anisotropic exchange coupled systems. It has also been shown that susceptibility measurements can indicate T_{N} via the Fisher relation.

This methodology has been used to further understand the interplay between structure and composition, and the magnetic properties of Ni^{2+} chains. NiF_2(3,5-lut)$_4$·H_2O and the NiX_2(3,5-lut)$_4$ (X = HF_2, Cl, Br, I) family are made up of Ni-X-X-Ni chains. Whilst the substitution of different halides changes the structure significantly along the chains, there is little change perpendicular to the chains, where non-bridging lutidine molecules inhibit magnetic interactions. The NiX_2N_4 octahedra also have very similar Ni—N bond lengths for all NiF_2(3,5-lut)$_4$·H_2O and NiX_2(3,5-lut)$_4$. These structural similarities between NiF_2(3,5-lut)$_4$·H_2O and NiX_2(3,5-lut)$_4$ give an excellent baseline with which to understand how the different halide ions effect the single-ion anisotropy and the magnetic exchange between Ni^{2+} ions along the chains. It was found that NiF_2(3,5-lut)$_4$·H_2O, Ni$(HF_2)_2$(3,5-lut)$_4$ and $NiCl_2$(3,5-lut)$_4$ contain negligible interactions and easy-plane anisotropy with D = +8.4(7), +11.97(2) and +9.6(2) K respectively. NiI_2(3,5-lut)$_4$ is a near ideal Heisenberg spin-chain in the Haldane phase with J = 17.5(1) K. NiI_2(3,5-lut)$_4$ is one of the most isotropic Haldane spin chains currently known, and has low critical fields within the range of commercially available magnets and magnets at neutron, muon and x-ray facilities. NiI_2(3,5-lut)$_4$ therefore has superb potential

for exploring the Haldane phase further. $NiBr_2$(3,5-lut)$_4$ appears to be made up of weakly interacting anisotropic spins with $J = 0.8(1)$ K and $D = +6.4(1.2)$ K. Susceptibility measurements do not agree with the magnitude of D and further measurements are required to confirm this.

As the size of the axial halide ligand in NiX_2(3,5-lut)$_4$ increases it moves further away from the Ni^{2+} ion. This increased elongation of the axial Ni—X bond corresponds to a decrease in the magnitude of D for NiX_2(3,5-lut)$_4$, which does not agree with the previously published theory [34]. However, this is based purely on bond lengths within Ni^{2+} octahedra. There are different ligands in NiX_2(3,5-lut)$_4$ that need to be taken into account. Even if the composition of the octahedra is kept constant and the bond lengths are changed, the structural dependence of D for NiN_4F_2 octahedra is not consistent with this theory (Fig. 4.14). Along with the results Chapter 3 for NiN_4O_2, NiN_2O_4 and NiN_4OF octahedra, this suggests that the moments on the nickel ions may prefer to point away from the most electronegative ligand. For NiX_2(3,5-lut)$_4$, this explains why octahedra with fluorine and chlorine ions, which are more electronegative than nitrogen, have easy-plane anisotropy. However, bromine and iodine are less electronegative than nitrogen but $NiBr_2$(3,5-lut)$_4$ has $D > 0$ and NiI_2(3,5-lut)$_4$ is almost Heisenberg-like. Therefore, it appears that single-ion anisotropy is affected by a mixture of crystal field and electronegative effects which compete against each other.

There is also a trend linking structure and composition to the magnetic exchange along Ni-X-X-Ni pathways in NiX_2(3,5-lut)$_4$. As the size of the bridging ion increases, adjacent nickel ions move closer together and J increases. Whilst NiF_2(3,5-lut)$_4$·H_2O doesn't follow this behaviour, the water molecule within the superexchange pathway appears to help inhibit magnetic interactions. Comparing the trends for NiX_2(3,5-lut)$_4$ with NiX_2(pyz)$_2$, both families show increasing strength of magnetic interactions as the size of the halide ions in the superexchange pathways increases [1]. However, the Ni—Ni distance increases in NiX_2(pyz)$_2$ as the size of X increases. This suggests that the size of the bridging halide ion has a more significant contribution to the strength of the superexchange interaction than the distance between Ni^{2+} ions.

Larger halide ions within superexchange pathways being better mediators of exchange is consistent with the magnetic properties of the quasi-two dimensional (QuinH)$_2CuBr_4$·$2H_2O$ and (QuinH)$_2CuCl_4$·$2H_2O$, where $J_{Br} \approx 4J_{Cl}$. From these parent samples, single-crystals of (QuinH)$_2$Cu(Cl_xBr_{1-x})$_4$·$2H_2O$ were grown, which exhibit bond disorder within the Cu-X planes due to he presence of these two competing magnetic pathways with different strengths. For low x, it was found that long

range order seemed to disappear for any observable temperature at $x_{C1} = 0.39\,(1)$. However, evidence of short-range correlations were observed up to $x_{C2} = 0.605$. The region $0.605 < x < 0.84$ appears to be totally disordered due to the absence of any sharp feature in the $x = 0.74$ and 0.835 magnetisation data and the absence of long-range order for $x \geq 0.41$. A sharp feature at saturation reappears in the $x = 0.84$ magnetisation data and there is long-range order below 0.44(1) K in $(\mathrm{QuinH})_2\mathrm{CuCl}_4{\cdot}2\mathrm{H}_2\mathrm{O}$. The data suggests a decoupling of the magnetic transition (x_{C1}) and the percolation transition (x_{C2}). This is consistent with the model published by R. Yu *et al.* [109]. Bond disorder seems to enhance quantum fluctuations, which destroys the classically predicted long-range order in the region $x_{C1} \leq x \leq x_{C2}$. There is a strong suggestion that a quantum Griffiths phase resides in this region.

The work presented in this thesis has furthered the understanding in how to characterise powdered, low-dimensional, anisotropic $S = 1$ Ni^{2+} antiferromagnets; how the magnetism is affected by changes in structure and composition; and an indication of how bond disorder effects magnetic interactions in a spin-1/2 quasi-two dimensional magnet antiferromagnet. However, further work remains. As this thesis has shown that electronic properties has a significant influence on single-ion and magnetic exchange properties, confirmation of the characterisation methodology is required to determine if it can be used universally for all $S = 1$ compounds. Further attempts to chemically engineer easy-axis Ni^{2+}-halide chains are required to verify the prediction that moments prefer to point away from strongly electronegative atoms made in Chapter 4. Finally, further measurements on $(\mathrm{QuinH})_2\mathrm{Cu}(\mathrm{Cl}_x\mathrm{Br}_{1-x})_4{\cdot}2\mathrm{H}_2\mathrm{O}$ in the region $0.61 < x < 1$ are required to finish mapping out the phase diagram and to accurately determine the nature of the two disordered phases.

Bibliography

[1] J. Liu, *et al.*, *Inorg. Chem.* **55**, 3515 (2016).

[2] R. T. Butcher, *et al.*, *Inorg. Chem.* **49**, 427 (2010).

[3] D. E. Lynch, I. McClenaghan, *Acta Crystallogr. Sect. E Struct. Reports Online* **58**, 551 (2002).

[4] K. Wierschem, P. Sengupta, *Mod. Phys. Lett. B* **28**, 1430017 (2014).

[5] I. A. Zaliznyak, D. C. Dender, C. Broholm, D. H. Reich, *Phys. Rev. B* **57**, 5200 (1998).

[6] Z. Honda, K. Katsumata, Y. Nishiyama, I. Harada, *Phys. Rev. B* **63**, 064420 (2001).

[7] M. Takigawa, T. Asano, Y. Ajiro, M. Mekata, Y. Uemura, *Phys. Rev. Lett.* **76**, 2173 (1996).

[8] A. Zheludev, *et al.*, *Phys. Rev. B* **62**, 8921 (2000).

[9] G. Xu, *et al.*, *Phys. Rev. B* **54**, R6827 (1996).

[10] J. L. Manson, *et al.*, *Inorg. Chem.* **51**, 7520 (2012).

[11] M. McElfresh, *Fundamentals of Magnetism and Magnetic Measurements* (1994).

[12] N. M, Atherton, *Principles of Electron Spin Resonance* (Ellis Horwood Limited, 1993), first edn.

[13] J. Brambleby, *et al.*, *Phys. Rev. B* **95**, 134435 (2017).

[14] D. C. Mattis, *The Theory of Magnetism I*, vol. 17 of *Springer Series in Solid-State Sciences* (Springer Berlin Heidelberg, Berlin, Heidelberg, 1981), first edn.

[15] P. de Maricourt (1269).

[16] P. G. Schmidl, *J. Arab. Islam. Stud.* **1**, 81 (1997).

[17] W. Gilbert, *De Magnete, Magneticisque Corporibus, et de Magno Magnete Tellure (On the Magnet and Magnetic Bodies, and on That Great Magnet the Earth)* (1600).

[18] S. J. Blundell, *Contemp. Phys.* **40**, 175 (1999).

[19] R. Martins, *Volta Hist. Electr.* pp. 245–265 (2003).

[20] K. Katsumata, *J. Phys. Condens. Matter* **12**, R589 (2000).

[21] C. P. Poole, *Electron spin resonance: a comprehensive treatise on experimental techniques* (John Wiley & Sons, Inc., 1996), second edn.

[22] K. Yosida, *Theory of Magnetism* (Springer-Verlag Berlin Heidelberg, 1996), first edn.

[23] G. A. Bain, J. F. Berry, *J. Chem. Educ.* **85**, 532 (2008).

[24] S. Blundell, *Magnetism in Condensed Matter* (Oxford University Press, 2001).

[25] S. Blundell, K. Blundell, *Concepts in Thermal Physics* (Oxford University Press, 2009), second edn.

[26] D. C. Mattis, *The Theory of Magnetism II*, vol. 55 of *Springer Series in Solid-State Sciences* (Springer Berlin Heidelberg, Berlin, Heidelberg, 1985), first edn.

[27] G. E. Pake, T. L. Estle, *The physical principles of electron paramagnetic resonance.* (W. A. Benjamin, Inc, 1973), second edn.

[28] S. J. Blundell, *Contemp. Phys.* **48**, 275 (2007).

[29] H. A. Jahn, E. Teller, *Proc. R. Soc. A Math. Phys. Eng. Sci.* **161**, 220 (1937).

[30] J. Krzystek, A. Ozarowski, J. Telser, *Coord. Chem. Rev.* **250**, 2308 (2006).

[31] R. C. Stevenson, *J. Magn. Reson.* **57**, 24 (1984).

[32] O. Kahn, *Molecular magnetism.* (Wiley-Blackwell, 1994), first edn.

[33] E. Wasserman, L. C. Snyder, W. A. Yager, *J. Chem. Phys.* **41**, 1763 (1964).

[34] R. Boča, *Coord. Chem. Rev.* **248**, 757 (2004).

[35] J. Titiš, R. Boča, *Inorg. Chem.* **49**, 3971 (2010).

[36] P. Baran, *et al.*, *Polyhedron* **24**, 1510 (2005).

[37] R. Ivaniková, *et al.*, *Polyhedron* **25**, 3261 (2006).

[38] A. Mašlejová, *et al.*, *Polyhedron* **25**, 1823 (2006).

[39] J. Titiš, *et al.*, *Polyhedron* **26**, 1523 (2007).

[40] T. Nagamiya, K. Yosida, R. Kubo, *Adv. Phys.* **4**, 1 (1955).

[41] P. W. Anderson, *Phys. Rev.* **79**, 350 (1950).

[42] A. Gingsberg, *Inorganica Chim. Acta Rev.* **5**, 45 (1971).

[43] M. E. Fisher, *Philos. Mag.* **7**, 1731 (1962).

[44] C. P. Landee, M. M. Turnbull, *J. Coord. Chem.* **67**, 375 (2014).

[45] J. H. Van Vleck, *Physica* **69**, 177 (1973).

[46] J. C. Bonner, M. E. Fisher, *Phys. Rev.* **135** (1964).

[47] M. E. Lines, *J. Phys. Chem. Solids* **31**, 101 (1970).

[48] D. C. Johnston, *et al.*, *Phys. Rev. B* **61**, 9558 (2000).

[49] F. M. Woodward, A. S. Albrecht, C. M. Wynn, C. P. Landee, M. M. Turnbull, *Phys. Rev. B* **65**, 144412 (2002).

[50] F. M. Woodward, *et al.*, *Inorg. Chem.* **46**, 4256 (2007).

[51] J. M. Law, H. Benner, R. K. Kremer, *J. Phys. Condens. Matter* **25**, 065601 (2013).

[52] J. J. Borras-Almenar, E. Coronado, J. Curely, R. Georges, *Inorg. Chem.* **34**, 2699 (1995).

[53] H. Bethe, *Zeitschrift fuer Phys.* **71**, 205 (1931).

[54] L. Onsager, *Phys. Rev.* **65**, 117 (1944).

[55] R. Georges, J. J. Borrás-Almenar, E. Coronado, J. Curély, M. Drillon, *Magn. Mol. to Mater.*, J. S. Miller, M. Drillon, eds. (Wiley-VCH Verlag GmbH & Co. KGaA, Weinheim, Germany, 2003), vol. 1-5, pp. 1–47.

[56] N. Tsyrulin, *et al.*, *Phys. Rev. B* **81**, 134409 (2010).

[57] N. D. Mermin, H. Wagner, *Phys. Rev. Lett.* **17**, 1133 (1966).

[58] M. E. Lines, *J. Appl. Phys.* **40**, 1352 (1969).

[59] M. A. Kastner, R. J. Birgeneau, G. Shirane, Y. Endoh, *Rev. Mod. Phys.* **70**, 897 (1998).

[60] K. Harada, N. Kawashima, *J. Phys. Soc. Japan* **67**, 2768 (1998).

[61] Z. Zhang, *et al.*, *Phys. Rev. B* **87**, 174405 (2013).

[62] J.-P. Renard, L.-P. Regnault, M. Verdaguer, *Magn. Mol. to Mater.* (Wiley-VCH Verlag GmbH & Co. KGaA, Weinheim, Germany, 2003), vol. 3, pp. 49–93.

[63] J. P. Renard, *et al.*, *Europhys. Lett.* **3**, 945 (1987).

[64] O. Avenel, *et al.*, *Phys. Rev. B* **46**, 8655 (1992).

[65] H. Manaka, I. Yamada, Z. Honda, H. Aruga Katori, K. Katsumata, *J. Phys. Soc. Japan* **67**, 3913 (1998).

[66] J. P. Renard, *et al.*, *J. Appl. Phys.* **63**, 3538 (1988).

[67] K. Katsumata, *et al.*, *Phys. Rev. Lett.* **63**, 86 (1989).

[68] V. Gadet, *et al.*, *Phys. Rev. B* **44**, 705 (1991).

[69] T. Takeuchi, *et al.*, *J. Phys. Soc. Japan* **61**, 3255 (1992).

[70] A. K. Bera, *et al.*, *Phys. Rev. B* **87**, 224423 (2013).

[71] Z. Honda, H. Asakawa, K. Katsumata, *Phys. Rev. Lett.* **81**, 2566 (1998).

[72] Z. Honda, K. Katsumata, M. Hagiwara, M. Tokunaga, *Phys. Rev. B* **60**, 9272 (1999).

[73] E. S. Sorensen, I. Affleck, *Phys. Rev. B* **51**, 16115 (1995).

[74] T. Kawae, M. Ito, M. Mito, K. Takeda, *J. Phys. Soc. Japan* **68**, 740 (1999).

[75] Y. Uchiyama, *et al.*, *Phys. Rev. Lett.* **83**, 632 (1999).

[76] M. Hagiwara, K. Katsumata, I. Affleck, B. I. Halperin, J. P. Renard, *Phys. Rev. Lett.* **65**, 3181 (1990).

[77] J. Lou, S. Qin, Z. Su, L. Yu, *Phys. Rev. B* **58**, 12672 (1998).

[78] A. P. Ramirez, S.-W. Cheong, M. L. Kaplan, *Phys. Rev. Lett.* **72**, 3108 (1994).

[79] K. Hallberg, C. D. Batista, a. a. Aligia, *Phys. Rev. B* **58**, 9248 (1997).

[80] M. W. Meisel, *arXiv:9809077v1* (1998).

[81] G. E. Granroth, *et al.*, *Phys. Rev. B* **58**, 9312 (1998).

[82] M. Fujita, *Met. Fram.*, L. R. MacGillivray, ed. (John Wiley & Sons, Inc., Hoboken, NJ, USA, 2010), pp. 1–35.

[83] S. R. Batten, *et al.*, *CrystEngComm* **14**, 3001 (2012).

[84] P. Ball, *Bright Earth: Art and the Invention of Color*, no. March (Farrar, Straus and Giroux, New York, 2001).

[85] H. J. Buser, D. Schwarzenbach, W. Petter, A. Ludi, *Inorg. Chem.* **16**, 2704 (1977).

[86] F. Herren, P. Fischer, A. Ludi, W. Haelg, *Inorg. Chem.* **19**, 956 (1980).

[87] T. Lancaster, *et al.*, *Phys. Rev. Lett.* **112**, 1 (2014).

[88] P. A. Goddard, *et al.*, *Phys. Rev. Lett.* **108**, 1 (2012).

[89] M. Cortijo, S. Herrero, R. Jiménez-Aparicio, E. Matesanz, *Inorg. Chem.* **52**, 7087 (2013).

[90] M. Gruden-Pavlović, M. Perić, M. Zlatar, P. García-Fernández, *Chem. Sci.* **5**, 1453 (2014).

[91] K. E. Marriott, *et al.*, *Chem. Sci.* **6**, 6823 (2015).

[92] L. H. R. Dos Santos, *et al.*, *J. Am. Chem. Soc.* **138**, 2280 (2016).

[93] P. R. Hammar, D. H. Reich, C. Broholm, F. Trouw, *Phys. Rev. B* **57**, 7846 (1998).

[94] P. R. Hammar, *et al.*, *Phys. Rev. B - Condens. Matter Mater. Phys.* **59**, 1008 (1998).

[95] J. L. Manson, *et al.*, *Chem. Mater.* **20**, 7408 (2008).

[96] P. A. Goddard, *et al.*, *New J. Phys.* **10**, 083025 (2008).

[97] F. Xiao, *et al.*, *Phys. Rev. B* **79**, 134412 (2009).

[98] K. Wierschem, Y. Kato, Y. Nishida, C. D. Batista, P. Sengupta, *Phys. Rev. B* **86**, 201108 (2012).

[99] R. Nath, *et al.*, *Phys. Rev. B* **91**, 054409 (2015).

[100] A. B. Christian, *et al.*, *Phys. Rev. B* **90**, 224423 (2014).

[101] J. L. Manson, *et al.*, *Sci. Rep.* **8**, 1 (2018).

[102] C. Yasuda, *et al.*, *Phys. Rev. Lett.* **94**, 217201 (2005).

[103] C. P. Landee, M. M. Turnbull, *Eur. J. Inorg. Chem.* **2013**, 2266 (2013).

[104] P. A. Goddard, *et al.*, *Phys. Rev. B* **93**, 094430 (2016).

[105] A. Zheludev, T. Roscilde, *Comptes Rendus Phys.* **14**, 740 (2013).

[106] V. Zapf, M. Jaime, C. D. Batista, *Rev. Mod. Phys.* **86**, 563 (2014).

[107] J. Brambleby, *et al.*, *Phys. Rev. B* **95**, 024404 (2017).

[108] L. Savary, L. Balents, *Reports Prog. Phys.* **80**, 016502 (2017).

[109] R. Yu, T. Roscilde, S. Haas, *Phys. Rev. B* **73**, 064406 (2006).

[110] N. Laflorencie, S. Wessel, A. Läuchli, H. Rieger, *Phys. Rev. B* **73**, 060403 (2006).

[111] J. Lashley, *et al.*, *Cryogenics (Guildf).* **43**, 369 (2003).

[112] J. S. Hwang, K. J. Lin, C. Tien, *Rev. Sci. Instrum.* **68**, 94 (1997).

[113] J. Brambleby, Quantum Magnetism in Coordination Polymers, Ph.D. thesis, The University of Warwick (2018).

[114] F. L. A. Machado, *et al.*, *Phys. Rev. B* **95**, 104418 (2017).

[115] G. R. Eaton, S. S. Eaton, D. P. Barr, R. T. Weber, *Quantitative EPR* (Springer Vienna, Vienna, 2010).

[116] N. M. Atherton, *Electron spin resonance : theory and applications* (Ellis Horwood Limited, 1973), first edn.

[117] T. Lancaster, *et al.*, *J. Phys. Condens. Matter* **16**, S4563 (2004).

[118] A. J. Steele, *et al.*, *Phys. Rev. B* **84**, 064412 (2011).

[119] R. S. Hayano, *et al.*, *Phys. Rev. B* **20**, 850 (1979).

[120] A. Le Bail, *Powder Diffr.* **20**, 316 (2005).

[121] H. Alloul, J. Bobroff, M. Gabay, P. J. Hirschfeld, *Rev. Mod. Phys.* **81** (2009).

[122] J. L. Manson, *et al.*, *Inorg. Chem.* **50**, 5990 (2011).

[123] K. Wierschem, P. Sengupta, *J. Phys. Conf. Ser.* **400**, 032112 (2012).

[124] T. Lancaster, *et al.*, *Phys. Rev. B* **73**, 020410 (2006).

[125] T. Lancaster, *et al.*, *Phys. Rev. Lett.* **99**, 267601 (2007).

[126] A. Allred, *J. Inorg. Nucl. Chem.* **17**, 215 (1961).

[127] J. A. Schlueter, *et al.*, *Inorg. Chem.* **51**, 2121 (2012).

[128] S. H. Lapidus, *et al.*, *Chem. Commun.* **49**, 499 (2013).

[129] J. L. Manson, *et al.*, *J. Am. Chem. Soc.* **131**, 6733 (2009).

[130] S. Yamamoto, S. Miyashita, *Phys. Rev. B* **50**, 6277 (1994).

[131] H. Nakano, M. Hagiwara, T. Chihara, M. Takahashi, *J. Phys. Soc. Japan* **66**, 2997 (1997).

[132] P. Mukherjee, M. G. B. Drew, C. J. Gomez-Garcia, A. Ghosh, *Inorg. Chem.* **48**, 5848 (2009).

[133] Y. Doi, R. Suzuki, Y. Hinatsu, K. Kodama, N. Igawa, *Inorg. Chem.* **54**, 10725 (2015).

[134] M. Sieling, W. Palme, B. Lüthi, *Zeitschrift für Phys. B Condens. Matter* **96**, 297 (1995).

[135] E. Čižmár, *et al.*, *New J. Phys.* **10**, 033008 (2008).

[136] A. Meyer, A. Gleizes, J. J. Girerd, M. Verdaguer, O. Kahn, *Inorg. Chem.* **21**, 1729 (1982).

[137] H. Kadowaki, K. Ubukoshi, K. Hirakawa, *J. Phys. Soc. Japan* **56**, 751 (1987).

[138] H. Mutka, *et al.*, *Phys. Rev. Lett.* **67**, 497 (1991).

[139] Y. Rahnavard, W. Brenig, *Phys. Rev. B* **91**, 054405 (2015).

[140] R. Yu, *et al.*, *Nature* **489**, 379 (2012).

[141] M. Dupont, S. Capponi, M. Horvatić, N. Laflorencie, *Phys. Rev. B* **96**, 024442 (2017).

[142] Y. C. Tzeng, H. Onishi, T. Okubo, Y. J. Kao, *Phys. Rev. B* **96**, 1 (2017).

[143] J. Kumar, S. N. Panja, S. Dengre, S. Nair, *Phys. Rev. B* **95**, 054401 (2017).

[144] M. Thede, *et al.*, *Phys. Rev. B* **86**, 180407 (2012).

[145] D. Hüvonen, *et al.*, *Phys. Rev. B* **86**, 214408 (2012).

[146] D. Hüvonen, *et al.*, *Phys. Rev. B* **85**, 100410 (2012).

[147] D. Hüvonen, G. Ballon, A. Zheludev, *Phys. Rev. B* **88**, 094402 (2013).

[148] A. Mannig, *et al.*, *Phys. Rev. B* **94**, 144418 (2016).

[149] K. Y. Povarov, *et al.*, *Phys. Rev. B* **92**, 024429 (2015).

[150] E. Wulf, *et al.*, *Phys. Rev. B* **88**, 174418 (2013).

[151] E. Wulf, *et al.*, *Phys. Rev. B* **91**, 014406 (2015).

[152] C. Binek, W. Kleemann, *Phys. Rev. B* **51**, 12888 (1995).